Doctoral Dissertation

Fabrication and microscopic characterization of nanosheets exfoliated from artificially-synthesis mica

Mohammad Razzakul Islam

Supervisor: Professor Masahiko Tomitori

Graduate School of Advanced Science and Technology
Japan Advanced Institute of Science and Technology
[Materials Science]
September 2020

Abstract

Fabrication and microscopic characterization of nanosheets exfoliated from artificially-synthesis mica

Mohammad Razzakul Islam

s1720401

Two-dimensional (2D) materials with atomic or molecular thickness have attracted extensive interest in material research communities because of their exotic properties for novel functional materials and devices. As represented by graphene, the method of mechanical exfoliation of cleavable 2D materials has opened a new era in 2D nanomaterials. Innovation using such 2D nanomaterials crucially depends on the scalability of their thickness and width, as well as the degree of purity and interaction with the substrate, which should be thoroughly investigated.

In this study, we successfully fabricated wide (several hundredths of micrometers) single layer (1 nm) to 20-layer nanosheets of pure artificially synthesized phlogopite on Si substrates. We then characterized their thickness and width by atomic force microscopy (AFM) and scanning Auger electron spectroscopy/microscopy (SAM), including SAM analysis of their chemical composition. In addition, by measuring the current–voltage (*I*–*V*) curves of metal–nanosheet–metal contacts by conductive AFM, we show the potential of phlogopite as a thin insulating 2D material with discrete thickness for electron tunneling devices. The nanoscale characterizations of mica nanosheets with focused electron beam has been investigated.

Phlogopite is a member of the mica family of silicate (phyllosilicate) minerals. It is a single crystalline oxide with a band gap energy of ~7 eV, perfectly cleavable along the (001) plane, and fascinating because of its high resistance to heat, water, and chemical agents. The phlogopite used in this study was purely artificially synthesized, and its quality was sufficiently high to be used for electronics applications. Thus, a method to control its discrete thickness by units of 1 nm and placing it on a substrate is of great importance to exploit phlogopite as an insulating 2D nanomaterial.

First, we propose a conventional approach using a polyurethane hand roller to exfoliate one- or few-layer 2D nanosheets with wide area from 2D cleavable crystals. In comparison with other exfoliation methods for 2D materials, including transfer processes to a substrate, our method easily and reliably provides clean and much wider 2D nanosheets with one- and few-layer thickness on the substrate.

Second, we propose a method to determine the thickness of mica nanosheets in the range from one to five layers on a Si substrate using SAM by taking the intensity ratios of the Auger electron spectroscopy (AES)

peaks of Mg and O as the compositional elements of the mica with respect to the peaks of the elements of the substrate, such as Si and the metal (Au and Ir in the present study). We derived thickness calibration curves based on the AES peak intensity ratios experimentally obtained for mica nanosheets with different thicknesses. The curves showed the AES intensity attenuation through the mica nanosheets with the inelastic mean free path, which is often used in photoelectron spectroscopy. Although SAM analysis of insulating materials tends to be avoided owing to terrible charging effects, we clearly demonstrate that SAM analysis is a powerful method for investigating insulating 2D nanomaterials.

Third, the electronic properties of the mica nanosheets were examined by conductive atomic force microscopy to measure their current–voltage (*I*–*V*) curves, exhibiting the characteristics of metal-insulator-metal contact having a tunneling barrier which is decreased with decreasing thickness. This would allow us to conduct the SAM analysis by avoiding the terrible charging effect on the insulating mica.

Finally, focused electron-beam induced etching of mica layers has been investigated as a selective nanoscale etching technique. In order to gain an understanding of the process, the effects of beam current, beam energy, and scan time on the process were examined as of controlling parameters. Experimental results indicated that the etching process is governed by the electron-stimulated desorption of mica elements from the mica compound.

This study demonstrated that the elemental and structural analysis of even insulating thin 2D layered materials can be plainly conducted by the SAM, the information of which is fundamental and critical to realize nanoscale electronic devices, composed of conducting and insulating 2D layered materials.

Keywords: Mica nanosheets, atomic force microscopy, scanning Auger electron microscopy/spectroscopy, current-voltage characterizations, focused electron beam

Acknowledgments

Firstly, I wish to express my sincere gratitude to my supervisor Prof. Masahiko Tomitori, Graduate School of Advanced Science and Technology, Japan Advanced Institute of Science and Technology, for providing me the opportunity to be his student. His kind guidance, valuable suggestions and constructive criticism contributed the necessary impetus in the completion of this work. His utmost faith in me was the prime source of motivation for me to stay focused during the entire time of research and preparation of this thesis.

I would like to express my deep thanks to the internal committee members Professor Yoshifumi Oshima, Professor Tokumitsu Eisuke and Professor Goro Mizutani, School of Materials Science at JAIST and my special thanks to Professor Masamichi Yoshimura from Toyota Technological Institute as an external committee.

I would like to express my deep thanks to my laboratory members and research group under Professor Yoshifumi Oshima.

Finally, I express my heartfelt gratitude to my parents and brothers, for their positivity, relentless support and encouragement in difficult times. I would like to dedicate this work to my parents, who have always believed in me and my dreams. Their faith makes me stronger every time and fuels my passion to dream big.

Mohammad Razzakul Islam

Tomitori's lab., JAIST, Ishikawa, Japan.

Table of Content

Chapter 1

Introduction

1.1 Research Background

The field of two-dimensional (2D) materials with atomic or molecular thickness represent a broad spectrum of materials with exceptional physical and electronic properties that has witnessed several significant advancements in a short period of time [1-6]. Compared to traditional three-dimensional (3D) bulk semiconductors, the electronic and optical properties of 2D materials often results in fascinating phenomena. This can be attributed to the unique properties possessed by 2D materials, such as ultralow weight, high Young's modulus, high strength, outstanding carrier mobility and strong in-plane anisotropy [7-11]. Since the successful exfoliation of graphene from graphite, a single atomic layer of carbon has paved the way to study the interesting family of 2D materials. In addition, apart from graphene, significant research effort has been directed toward 2D semiconducting materials such as boron nitride (h-BN), transitions metal dichalcogenides (TMDs) and layered transition metal oxides [12-17]. By exploiting the unique mechanical and electric properties, 2D materials can be used in wide-ranging applications, including flexible electronics, strain sensors, nano-generators, and innovative nano-electromechanical systems. A layered materials 'mica', one of the groups of sheet silicate (phyllosilicate) minerals, is an oxide with a band gap of ~7 eV, has prominent characteristic application in the electronic and electrical industries because of its optical transparency, uniform high dielectric constant and mechanical strength as well as its high resistance to heat, water, and chemical agents [18-21]. Mica is an insulator with an ultra-flat surface and a highly stable structure that can also be used to tune the carrier mobility of other two-dimensional materials, such as graphene, MoS_2, and others [22,23].

The unique properties of 2D materials greatly depends on the preparations process. In that case, mechanical exfoliation process is one of the reliable methods to prepare high quality single crystal

2D materials that can exhibit near ideal electronic behaviors. Mechanical exfoliation and transfer techniques lead to understanding of new physical phenomena, however, exfoliation techniques fall short in terms of scalability. Also the unique electrical, optical, and mechanical properties of 2D materials considerably depend on the thickness of the nanosheets as well as the interaction with the underlying substrates. With regard to the development of devices using 2D mica nanosheets, a conventional and reliable method to prepare high quality scalable 2D nanosheets and a process that can conveniently evaluate their thickness is of great importance.

Despite the advantageous and unique material properties of mica, fundamental issues still exist with the manipulation of these materials. Deeper understanding of the underlying mechanisms and chemical manipulation of the 2D materials at the nanoscale is an increasing requirement for novel nanofabrication. One method is called focused electron beam induced processing, a nanofabrication technique which has drawn considerable appeal in terms of the novel capabilities offered [24,25]. Therefore, it is very important to investigate and characterize mica nanosheets under focus electron beam and mechanism involving with electron beam manipulation.

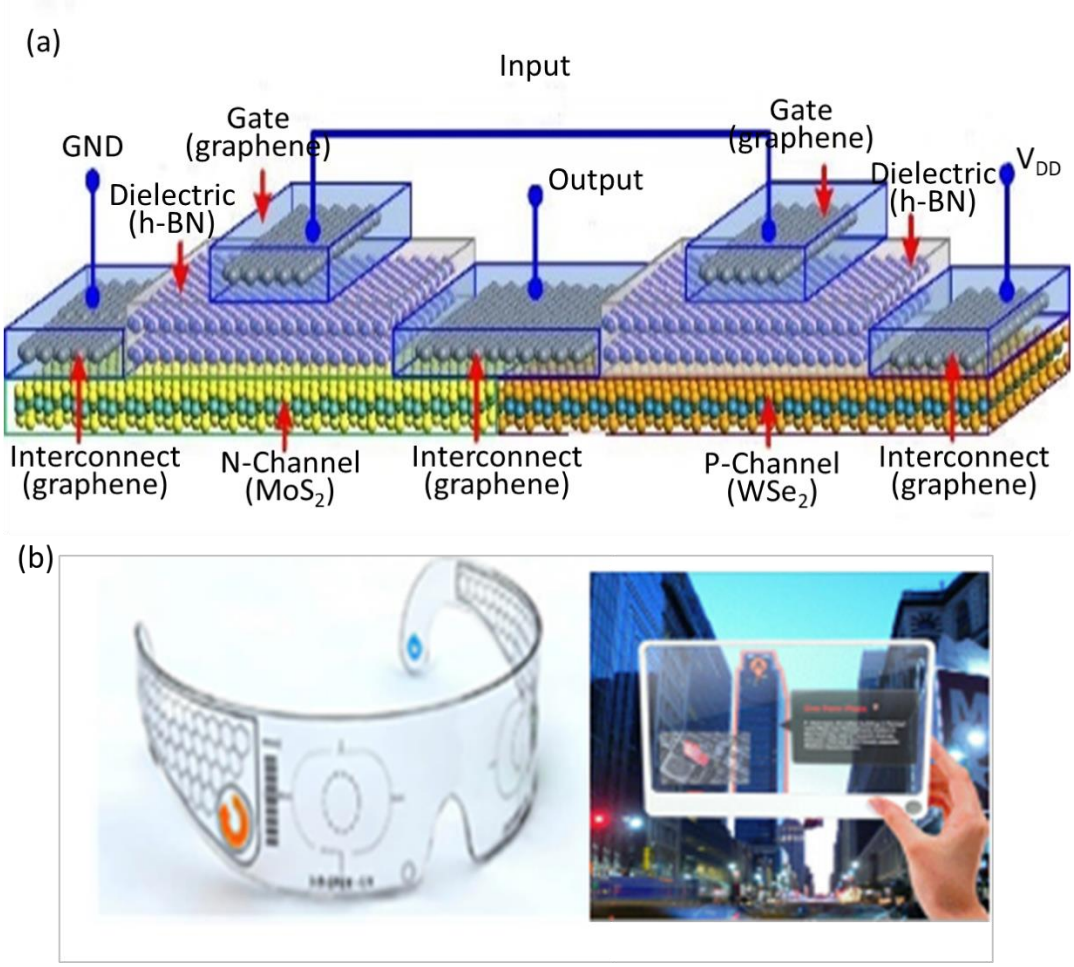

Figure 1.1: (a) An example of 2D hybrids materials-based circuit [3]. (b) Applications of 2D materials to the flexible and transparent devices. [3]

1.2 Purpose of the Study

The purpose of this study is to develop a method to prepare large area and high quality atomically thin 2D mica nanosheets as thin as just one layer (1 nm) and measuring their properties as well as the thickness on different substrates such as SiO_2/Si wafers and gold and Iridium-coated Si wafers. To mechanically exfoliate large and high-quality mica 2D sheets from bulk mica and affix them on the substrates, we modify the approach by using a polyurethane hand roller for the exfoliation. To analyze artificially synthesis pure mica (phlogopite) nanosheets, we use scanning Auger electron

microscopy/spectroscopy (SAM) as well as atomic force microscopy (AFM), in regard to their 2D shapes and thicknesses with less than 10 layers, and their atomic species. Auger electron spectroscopy (AES) possesses high chemical sensitivity as a surface analytical technique, based on the kinetic energy spectrum of electrons backscattered from the sample irradiated with an accelerated electron beam, which is used to determine the ultra-thin film thickness. Although scanning electron microscopy (SEM), which function is also conducted in the SAM, is not usually applied to insulating materials because of terrible charging effects induced by irradiation of the electron beam, we challenge to analysis mica nanosheets using the SAM. The tunneling current and barrier height of few-layer mica are characterized with conductive AFM. The nanoscale characterization of mica nanosheets with focused electron beam is presented and discussed with the mechanism involving beam interactions with mica as an oxide.

1.3 The Structure and Property of Mica

Mica is a type of phyllosilicates that exhibiting two-dimensional sheet or layered structure. Mica is formed by a complex aluminosilicate mineral with the ideal unit cell formula can be represented by a chemical formula of $X_2Y_{4-6}Z_8O_{20}(OH,F)_4$, in which X represents interlayer cations (K^+, Na^+, Ca^{2+}), Y represents the octahedral coordinated elements (Al^{3+}, Mg^{2+}, Fe^{2+}, Li^+ ,..), and Z represents the tetrahedral coordinated elements (Si^{4+}, Al^{3+},..). Two tetrahedral (T) sheets on both sides of an octahedral (O) sheet forming the layered mica structural unit (1 nm). Silicate tetrahedron (SiO_4) and aluminum octahedron (AlO_6) are the basic building blocks of mica layers and these layers with a ratio of 2:1 are repeatedly bound together interlayer potassium ions. Mica layered structure is consist of alternating aluminosilicate and potassium ion layers. In the aluminosilicate layer Si ions are partially substituted by Al ions (1/3), which gives a net negative charge to the layer and interlayer cations (K^+) maintaining the charge neutrality of the unit. For the phlogopite mica the center of each octahedron is occupied by Mg and for muscovite mica Al. The electrostatic force between the K^+ and

the aluminosilicate layer is shared among 12 oxygen atoms, due to the weak attraction force between the K^+ and the aluminosilicate layers and perfect cleavage parallel to the (001) plane occurs easily along this interface. Upon cleavage along (001) plane mica surface exhibits a hexagonal arrangement of Si and O atoms partly covered by potassium ions produces two large, atomically flat surfaces on both sides of the cleaved mica, with each expose surface is occupied with equal but randomly distributed K^+ atoms to preserve the charge neutrality of the mica sheets.

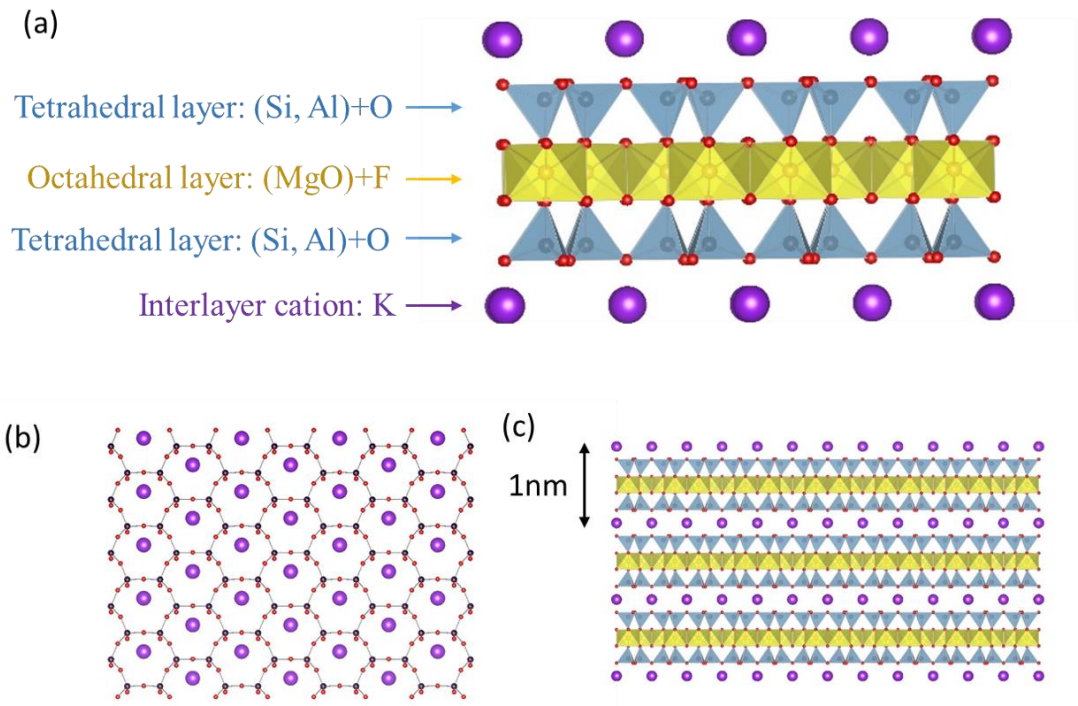

Figure 1.2: Crystal structure. (a) Structural unit of mica. Surface structure of phlogopite mica: (b) [001] projection and (c) [100] projection.

The following are the most noticeable features that makes mica an ideal material for flexible device applications.

i. 2D structure: Mica shows strong intra-layer but weak inter-layer van der Waals (vdW) and electrostatic interactions that's possible to peel off over layer from bulk mica creating two-dimensional thin film.

ii. Transparent: Several-layer mica sheet exhibits clear transmittance in the ultraviolet–visible-infrared range of the electromagnetic spectrum and gain more attraction to optoelectronic applications.

iii. Elastic: The high elasticity of atomically thin mica nanosheets as a mechanical property of mica crystals validate their applicability as dielectric substrates in highly demanding mechanical applications.

iv. Flexible: Mica has very high yield strain and the bending radius down to 0.03 cm is reported for 100 nm thick mica sheet [29].

v. Chemically inert: The absence of dangling bonds on surface makes mica highly tolerable against chemical bonding.

vi. Electrically insulating: Insulating properties of mica is much higher than other 2D insulating materials and mica is a perfect candidate for the use as a gate dielectric in flexible electronic devices [29].

vii. High thermal resistance: artificially synthesized pure phlogopite mica ($KMg_3AlSi_3O_{10}F_2$), which is suitable for electronic device processes and applications because it is thermally stable up to a maximum operating temperature of ~1100 °C and is much purer than natural mica in minerals, e.g., muscovite ($KAl_2(AlSi_3)O_{10}(OH)_2$) with the temperature of ~550 °C [30]. Coefficient of thermal expansion (CTE) of mica matched with Si.

viii. Atomically flat surface: This is the key reason for using mica in TEM and AFM observations. Moreover, mica is the ideal substrate because of its ultra-high surface flatness for investigating other 2D materials.

ix. Inexpensive and abundant: Phyllosilicates are one of the most abundant minerals found in in all the three major rock verities-igneous, sedimentary and metamorphic.

1.4 Remaining Chapter Summary

This thesis will focus on developing exfoliation method and characterizing layered materials phlogopite mica with AFM, SAM, and the focus electron beam induced etching. The results will be split into the following main chapters:

Chapter 2. Background- This chapter will give a background of all experimental technique used in this project.

Chapter 3. Mechanical exfoliations- Introducing new approach of mechanical exfoliations process with the poly-urethane hand roller. This chapter will discuss the mechanism and advantages of the newly invented approach to exfoliate wider and high quality nanosheets and compare the result with other conventional methods.

Chapter 4. Thickness measurement- The main objective of this chapter is to evaluate thickness of few layer mica nanosheets with Auger electron spectroscopy, SEM image observations and current-voltage characterizations of insulating few layer mica nanosheets are discussed.

Chapter 5. Electron beam irradiations- In this chapter we will investigate the effect and involving mechanism of focus electron beam irradiations on mica surface and finding the beam controlling parameters to selectively etching mica layers with the incident electron beam.

Chapter 6. Conclusions- This chapter will summarize the results found in this thesis and give insight into the future directions of these results.

References

1. Xia, Fengnian, et al. "Two-dimensional material nanophotonics." Nature Photonics 8.12 (2014): 899-907.

2. Novoselov, Kostya S., et al. "Two-dimensional gas of massless Dirac fermions in graphene." Nature 438.7065 (2005): 197-200.
3. Kang, Jiahao, et al. "Graphene and beyond-graphene 2D crystals for next-generation green electronics." Micro-and Nanotechnology Sensors, Systems, and Applications VI. International Society for Optics and Photonics 9083. (2014): 908305-908312.
4. Castellanos-Gomez, Andres. "Why all the fuss about 2D semiconductors?" Nature Photonics 10.4 (2016): 202-204.
5. Bhimanapati, Ganesh R., et al. "Recent advances in two-dimensional materials beyond graphene." ACS nano 9.12 (2015): 11509-11539.
6. Song, Li, et al. "Large scale growth and characterization of atomic hexagonal boron nitride layers." Nano letters 10.8 (2010): 3209-3215.
7. Liu, Han, et al. "Phosphorene: an unexplored 2D semiconductor with a high hole mobility." ACS nano 8.4 (2014): 4033-4041.
8. Kumar, Anshuman, et al. "Tunable light–matter interaction and the role of hyperbolicity in graphene–hBN system." Nano letters 15.5 (2015): 3172-3180.
9. Fei, Ruixiang, and Li Yang. "Strain-engineering the anisotropic electrical conductance of few-layer black phosphorus." Nano letters 14.5 (2014): 2884-2889.
10. Li, Peining, et al. "Hyperbolic phonon-polaritons in boron nitride for near-field optical imaging and focusing." Nature communications 6.1 (2015): 1-9.
11. Dai, S., et al. "Tunable phonon polaritons in atomically thin van der Waals crystals of boron nitride." Science 343.6175 (2014): 1125-1129.
12. Novoselov, Kostya S., et al. "Electric field effect in atomically thin carbon films." science 306.5696 (2004): 666-669.
13. Dean, Cory R., et al. "Boron nitride substrates for high-quality graphene electronics." Nature nanotechnology 5.10 (2010): 722-726.

14. Jeong, S., et al. "Raman scattering studies of the lattice dynamics in layered MoS_2." Journal of the Korean Physical Society 66.10 (2015): 1575-1580.
15. Wilson, Jl A., and A. D. Yoffe. "The transition metal dichalcogenides discussion and interpretation of the observed optical, electrical and structural properties." Advances in Physics 18.73 (1969): 193-335.
16. Zhao, Yang, et al. "Recent developments and understanding of novel mixed transition-metal oxides as anodes in lithium ion batteries." Advanced Energy Materials 6.8 (2016): 1502175-1502194.
17. Kalantar-zadeh, Kourosh, et al. "Two dimensional and layered transition metal oxides." Applied Materials Today 5 (2016): 73-89.
18. Maslova, M. V., L. G. Gerasimova, and Willis Forsling. "Surface properties of cleaved mica." Colloid Journal 66.3 (2004): 322-328.
19. Castellanos-Gomez, Andres, et al. "Atomically thin mica flakes and their application as ultrathin insulating substrates for graphene." Small 7.17 (2011): 2491-2497.
20. Low, Chong Guan, et al. "Graphene field effect transistors with mica as gate dielectric layers." Small 10.20 (2014): 4213-4218.
21. Bitla, Yugandhar, and Ying-Hao Chu. "MICAtronics: A new platform for flexible X-tronics." FlatChem 3 (2017): 26-42.
22. Rudenko, A. N., et al. "Graphene adhesion on mica: Role of surface morphology." Physical Review B 83.4 (2011): 045409.
23. Low, Chong Guan, and Qing Zhang. "Ultra-thin and Flat Mica as Gate Dielectric Layers." Small 8.14 (2012): 2178-2183.
24. Barth, Johannes V., Giovanni Costantini, and Klaus Kern. "Engineering atomic and molecular nanostructures at surfaces." Nanoscience and technology: a collection of reviews from Nature journals. 2010. 67-75.

25. Utke, Ivo, Stanislav Moshkalev, and Phillip Russell, eds. Nanofabrication using focused ion and electron beams: principles and applications. Oxford University Press (2012).
26. Pauling, Linus. "The structure of the chlorites." Proceedings of the National Academy of Sciences of the United States of America 16.9 (1930): 578-582.
27. Fleet, Michael E., et al., eds. "Rock-forming minerals: Micas." Geological Society of London (2003).
28. Castellanos-Gomez, Andres, et al. "Mechanical properties of freely suspended atomically thin dielectric layers of mica." Nano Research 5.8 (2012): 550-557.
29. He, Yudong, et al. "Mica, a Potential Two-Dimensional-Crystal Gate Insulator for Organic Field-Effect Transistors." Advanced Materials 23.46 (2011): 5502-5507.
30. Barlow, S. G., and D. A. C. Manning. "Influence of time and temperature on reactions and transformations of muscovite mica." British ceramic transactions 98.3 (1999): 122-126.

Chapter 2

Background

2.1 Atomic Force Microscopy

Atomic force microscopy (AFM) is an atomic resolution type of scanning probe microscopy (SPM), the illustrated resolution on the order of fractions of a nanometer, more than thousand times better than the optical diffraction limit [1]. The surface information of the sample is gathered by "feeling" or "touching" the sample surface with a mechanical probe and building up a map of the height or topography of the surface as it goes along. Piezoelectric elements that facilitate tiny but accurate and precise movements on electronic command enable perfect scanning of the sample. Through this research work we have used Molecular Imaging's PicoPlus controller, the PicoScan 2500 with the environmental chamber for the control environmental experiment.

Figure 2.1: AFM setup. [https://images.app.goo.gl/4zWEVPADUmmcTEv1A]

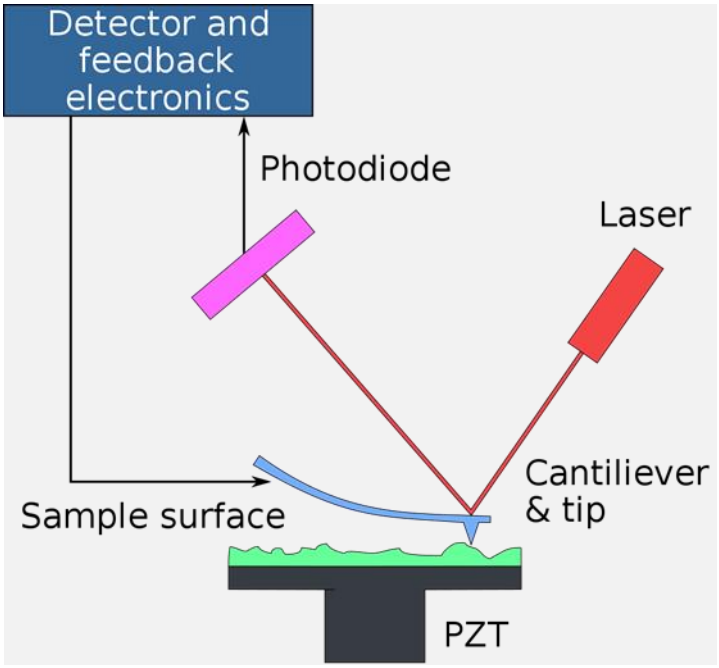

Figure 2.2: An AFM instrument generates topographic images by moving a small cantilever over the surface of a sample. A sharp tip is attached on the end of the cantilever that contact with the sample surface, the reflected laser beam from the backside of the cantilever is detected by a photodetector and send to the detector and feedback electronic.

The atomic force microscopy consists of cantilever with a tip, a laser source, photodiode with detector and feedback circuit. Typically, silicon or silicon nitride cantilever with a sharp tip (probe) attached at its end which is used to scan the specimen surface by contacting the sample surface or vibrating on top of the surface depending on the scan mode. When the tip is brought into proximity of a sample surface, forces between the tip and the sample lead to a deflection of the cantilever according to Hooke's law [2]. Depending on the scan mode, forces that are measured in AFM include mechanical contact force, van der Waals forces, capillary forces, chemical bonding, electrostatic forces etc. The AFM can be operated in a number of modes, depending on the application such as static (also called contact) modes and a variety of dynamic (non-contact or "tapping") modes where the cantilever is vibrated or oscillated at a given frequency [3]. In this research work we have used contact mode operations with the silicon nitride tip for the image topography and for the conductive AFM mode, we used 10 nm Iridium coated silicon nitride tips.

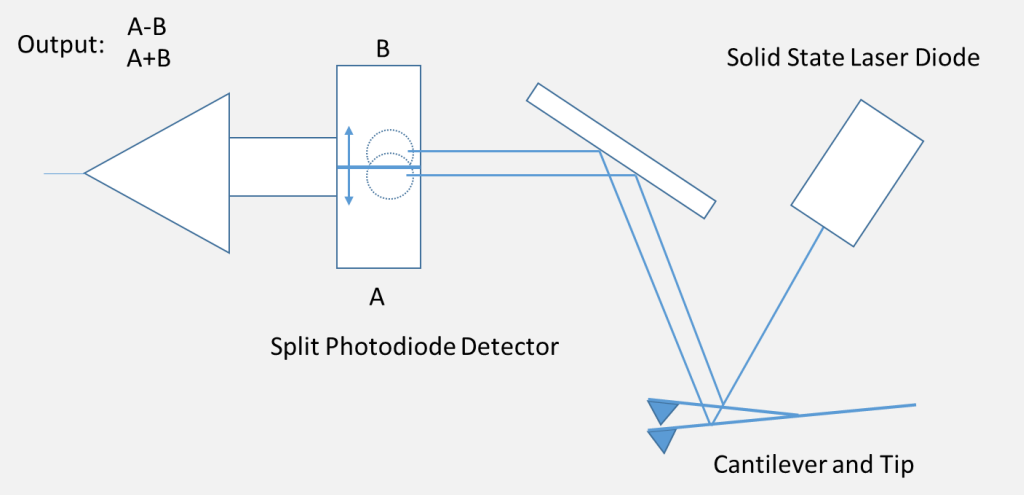

Figure 2.3: AFM beam-deflection detection

2.1.1 Conductive Atomic Force Microscopy

Atomic force microscopy has divers of functions to characterized surface morphology of different type of sample. With modifications of the setup, AFM can be used to measure the surface conductivity and tunneling current of two-dimensional materials. The conductive atomic force microscopy (cAFM) can simultaneously measure the topography of the sample surface and electric current flow at the contact point of the tip and sample. Laser deflection from the backside of the cantilever measured the topographic image of the sample, while current is detected using a current-to-voltage preamplifier [4]. The application of topographic imaging and current detection make C-AFM advanced scanning probe microscopy compared to scanning tunneling microscopy (STM). Generally, in STM the current flowing between the tip and the sample (the distance can be calculated depending on the current) constricting the topography picture of the sample. Therefore, when STM is performed a sample portion scanning, it is not possible to discern the current fluctuations that are related to a change in the topography (due to surface roughness) or to a change in the sample conductivity (due to intrinsic inhomogeneities). On the other hand, the C-AFM is generally operated in contact mode; the tip can

be kept at one location while the voltage and current signals are applied/read, or it can be moved to scan a specific region of the sample under a constant voltage (and the current is collected).

The conductive atomic force microscopy is operated under the following conditions: i) the tip (probe) must be conductive; ii) a voltage source is needed to apply a potential difference between the tip and the sample holder; iii) a pre-amplifier is used to convert the current signal into a voltage signal that can be read by the computer via an analog–digital converter [4]. In C-AFM experiments, the sample holder must needed to use conductive wire or tape to connect the sample with holder to make complete circuit to apply bias voltage [5]. The currents collected by the CAFM obey the relationship:

$$I = \underline{J} \times A_{eff}$$

where I is the total current flowing through the tip/sample nanojunction, J is the current density and A_{eff} is the effective emission area through which electrons can flow [4]. The most common mistake in C-AFM research is to assume that the effective emission area A_{eff} equals the physical contact area A_{c}. Usually this assumption is incorrect because in different tip/sample systems the electrical field applied may propagate laterally. For example, the lateral conductivity of the sample is very high when the C-AFM tip is placed on a metal, making the whole sample surface area electrically connected (A_{eff} equals the area covered by the metallic film/electrode) [6,7]. On the contrary, if the C-AFM tip is placed directly on an insulator, it acts as a nano-sized electrode and provides a very high lateral resolution. A_{eff} has been defined as: "the sum of all those infinitesimal spatial locations on the surface of the sample that are electrically connected to the C-AFM tip (potential difference is negligible).

2.2 Scanning Auger Microscopy

Scanning Auger microscopy (SAM)/Auger electron spectroscopy (AES) is an Auger electron effect-based electron beam techniques. An incident electron beam with energy typically 3–25 keV impinges

on sample surface and causes an Auger electrons emission. This is a chain of radiation-less transitions process following the ionization of atoms by the incident electrons and finally ends up by the ejection of an electron which is known as an Auger electron. Very short inelastic mean free paths of the Auger electron make AES extremely surface sensitive (sampling depth of 3–5 nm) thus allow the analysis of the elemental composition of materials.

The elemental maps of the sample surface are produced by scanning Auger microscopy by scanning the electron beam over the sample and selecting specific Auger peaks. Depth profiling can also be run by AES using an Ar^+ sputter gun and in-depth elemental distributions are obtained through measurements of concentration profiles. The Auger depth profiling reveals ultra-thin layers and quantifying their elemental composition also in-depth information can also be obtained by analyzing a cross-sectional sample. In the SAM observations, sample preparations are quite convenient compared to transmission electron microscopy, complex sample preparation are not required in SAM. Ultra-high surface sensitivity makes SAM complementary to electron microscopy techniques (EDX and EELS) and higher spatial resolution offers an alternative to photoelectron spectromicroscopy (XPEEM).

In the process of Auger effect, an atom is excited by a beam of electrons with energies in the range of several eV to 50 keV, a core state electron can be removed leaving behind a hole. Leaving one electron from the core level transfer the atom into unstable state, the core hole can be filled by an outer shell electron, whereas the electron moving to the lower energy level loses an amount of energy equivalent to the difference in orbital energies. The transition energy can be coupled to a second outer shell electron, which will be ejected from the atom if the transferred energy is larger than the orbital binding energy [8-13].

The emitted electron will have a kinetic energy of:

$$E_{\text{kin}} = E_{\text{Core State}} - E_{\text{B}} - E`_{\text{C}},$$

where $E_{\text{Core State}}$ is the core level, E_B is first outer shell and $E`_C$ is second outer shell electron positive binding energies. Since a specific atom has unique orbital energies, analysis of the emitted electrons can provide information about the chemical composition of a surface. **Figure 2.4** illustrates two schematic views of the Auger process.

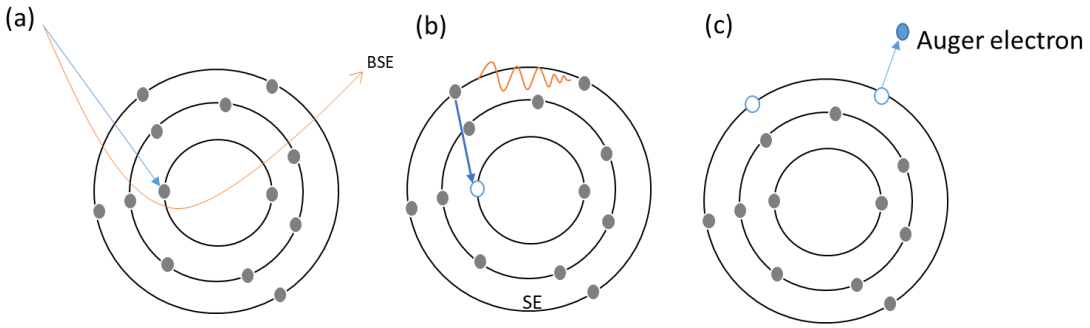

Figure 2.4: (a) The incident electron makes the ionization of the core level electron in the atom. (b) Upper level electron falls to a lower level by releasing a quantum of energy and (c) the energy released from the second electron excites the Auger electron which leaves the atom.

The surface sensitivity in AES involved with emitted electrons which usually have energies ranging from 50 eV to 3 keV and at these values, in the solid electrons have a short mean free path. The electrons escape depth is therefore localized within a range few nanometers depth of the target surface (**Fig. 2.5)**, this give AES an extreme sensitivity to surface species [13]. Ultra-high vacuum (UHV) conditions is required in the AES setup because of the low energy of the Auger electrons. Measurement in high vacuum conditions prevent electron scattering [12–14]. Typical AES setup schematically shown in **Fig. 2.6**. In this configuration, incident focused electrons strike on a sample and emitted electrons (Auger electrons) are deflected into a cylindrical mirror analyzer (CMA). The collected Auger electrons in the electron energy analyzer are plotted as a function of energy against the broad secondary electron background spectrum [15].

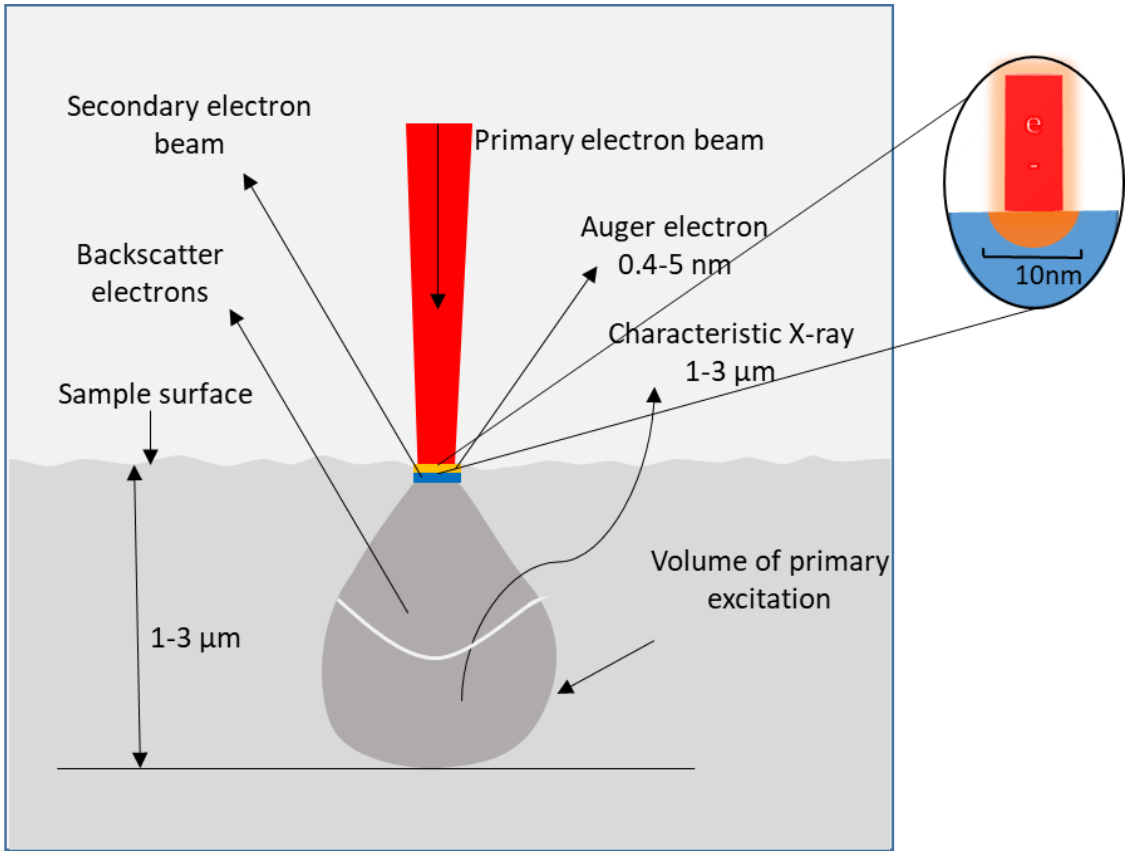

Figure 2.5: Auger electron fail to emerge with their characteristic energies if they start from deeper than about 0.5 to 5 nm into the surface.

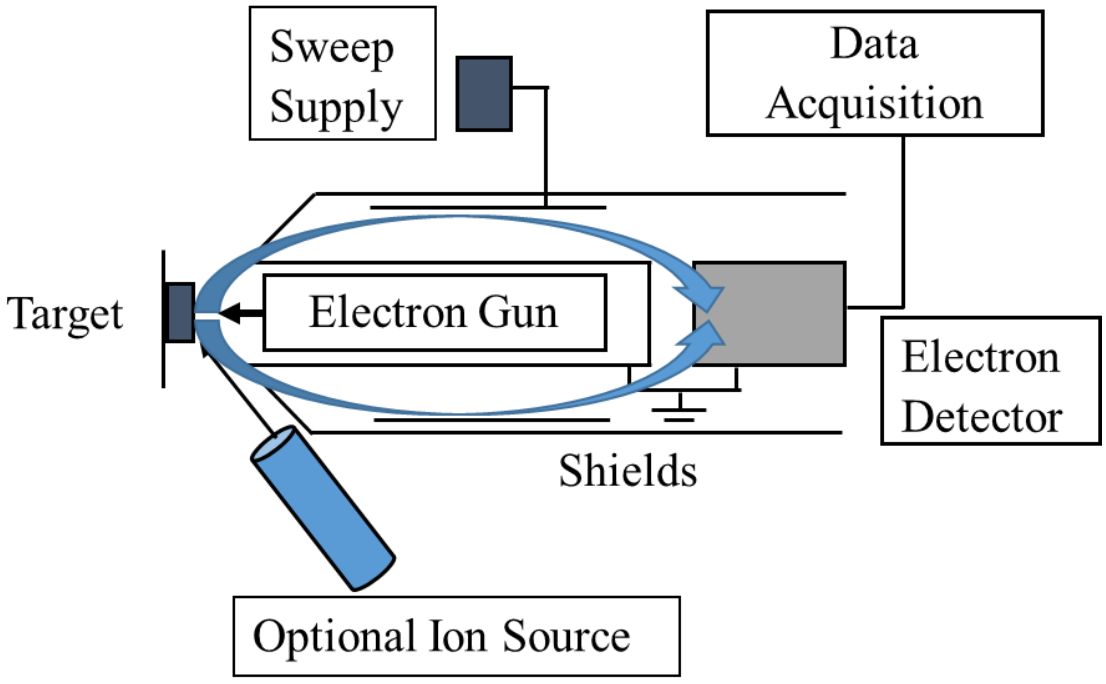

Figure 2.6: AES experimental setup using a cylindrical mirror analyzer (CMA).

In the collecting AES spectra, the Auger peaks intensity is small compared to the background noise level, to highlight the actual peak intensities of specific elements AES is often run in a derivative mode by modulating the electron collection current via a small applied AC voltage. Derivative mode of AES spectra emphasizes Auger fine structure with small secondary peaks surrounding the primary Auger peak. **Figure 2.7** illustrates a derivative spectrum from a mica sample clearly showing the Auger peaks.

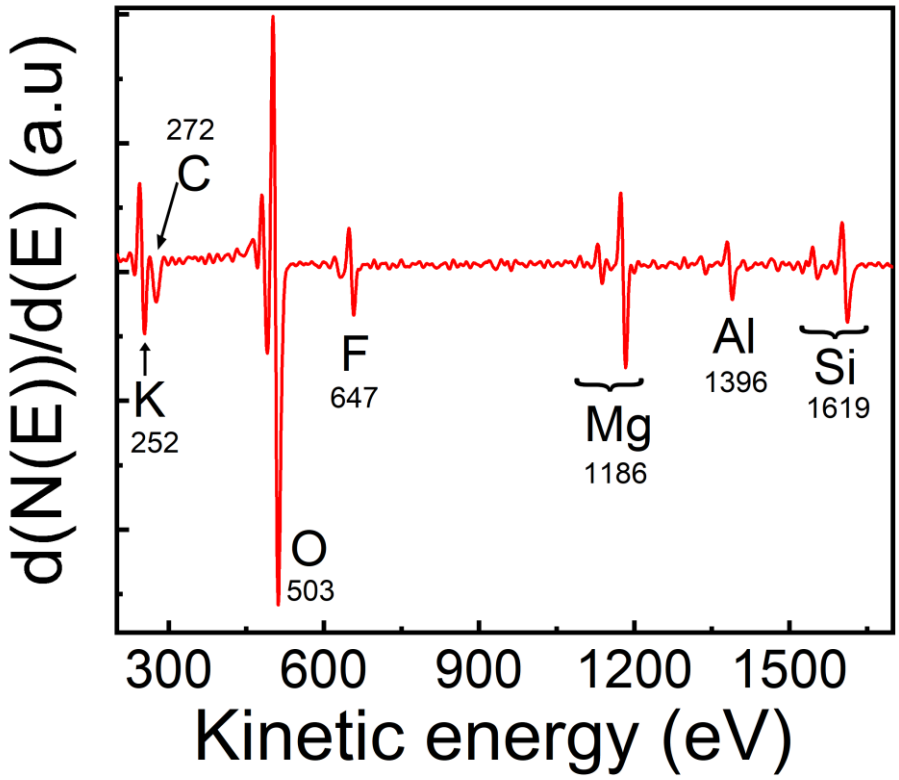

Figure 2.7: Auger spectrum of mica in derivative mode plotted as a function of Auger electron energy.

2.3 Inelastic Mean Free Path

The term inelastic mean free path (IMFP) are frequently used to specify the surface sensitivity of Auger-electron spectroscopy. The IMFP is define as how far an electron on average travels through a solid before losing its energy. When a monochromatic primary electrons beam is incident on a

sample surface, Auger electrons from atoms near-surface region of the solid are ejected. Through plasmon excitation, electron-hole pair formation, and vibrational excitation majority of incident electron loss their primary energy when passing through the solid sample surface [16].

The intensity of the primary electron beam I_0 damps as a function of distance d into the solid. The intensity decay can be expressed as follows:

$$I(d) = I_0 e^{-d/\lambda(E)}$$

Where $I(d)$ is the intensity after the primary electron beam has traveled through the solid to a distance d. The parameter $\lambda(E)$, termed the inelastic mean free path (IMFP), is defined as the distance an electron beam can travel before its intensity decays to $1/e$ of its initial value. The inelastic mean free path of electrons can roughly be described by a universal curve that is the same for all materials [17,18].

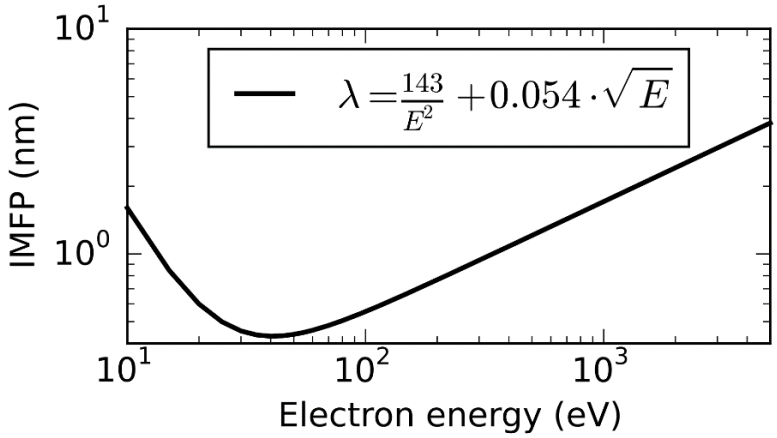

Figure 2.8: Universal curve for the electron inelastic mean free path in elements in [17].

2.4 Tunneling

2.4.1 Metal-Insulator-Metal Tunnel Diode

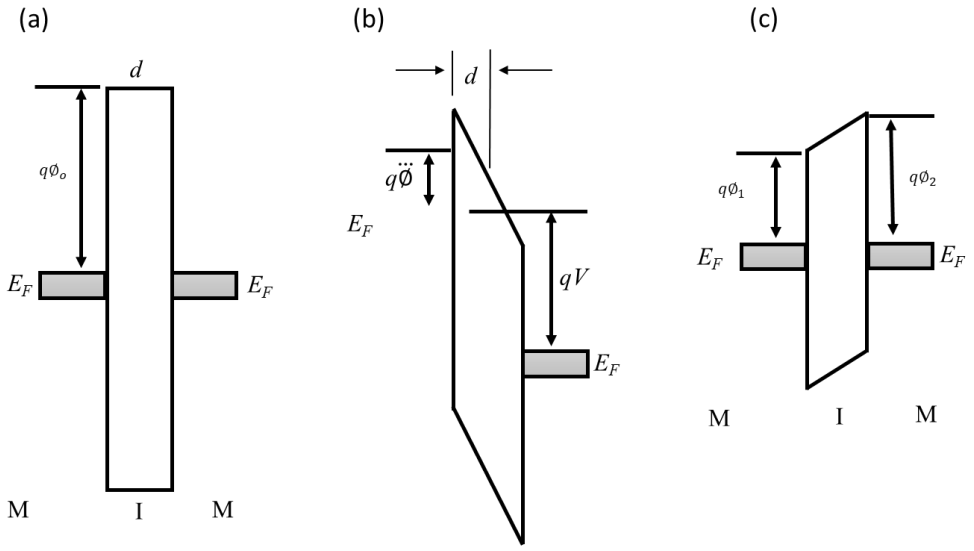

Figure 2.9: Energy-band diagrams of MIM structures. (a) Symmetrical MIM under equilibrium. (b) Under bias, $V > \emptyset_0$. (c) Asymmetrical MIM.

A metal-insulator-metal (MIM) tunnel diode is a thin-film structure consisting of well-defined single crystal material sandwiched between two metal electrodes is the ideal model for study of tunneling current of insulating materials. In the MIM structure the electrons from the first metal can tunnel through the insulator film and be collected by the second metal. It displays nonlinear *I-V* characteristics but negative resistance is not present. The nonlinear *I-V* nature is sometimes used for microwave detection as a mixer. **Figures 2.9 (**a) and (b) show the basic energy-band diagrams of a MIM diode with similar metal electrodes. Since all of the voltage applied is dropped across the insulator, the tunneling current through the insulator is,

$$J = \frac{4\pi q m^*}{h^3} \iint T_t[F(E) - F(E + qV)]dE_\perp dE$$

At 0 K,

$$J = J_0 \left[\widehat{\emptyset} \exp\left(-C\sqrt{\widehat{\emptyset}}\right) - \left(\widehat{\emptyset} + V\right) \exp\left(-C\sqrt{\widehat{\emptyset} + V}\right) \right],$$

where

$$J_0 \equiv \frac{q^2}{2\pi h d^{*2}} \text{ and } C \equiv \frac{4\pi d^* \sqrt{2m^* q}}{h}$$

For the ideal symmetrical MIM structure the current density is given by

$$J = J_0 \left[\left(\emptyset_0 - \frac{V}{2}\right) exp\left(-C\sqrt{\emptyset_0 - \frac{V}{2}}\right) - \left(\emptyset_0 + \frac{V}{2}\right) exp\left(-C\sqrt{\emptyset_0 + \frac{V}{2}}\right) \right].$$

The present investigation we fabricating iridium-mica-iridium structure and measuring the tunneling properties of few-layer mica nanosheets using above equations with conductive atomic force microscopy.

References

1. Cappella, Brunero, and Giovanni Dietler. "Force-distance curves by atomic force microscopy." Surface science reports 34.1-3 (1999): 1-104.
2. Cappella, Brunero. "Physical Principles of Force–Distance Curves by Atomic Force Microscopy." Mechanical Properties of Polymers Measured through AFM Force-Distance Curves. Springer, Cham, (2016).
3. Binnig, Gerd, Calvin F. Quate, and Ch Gerber. "Atomic force microscope." Physical review letters 56.9 (1986): 930-933.
4. Lanza, Mario Conductive Atomic Force Microscopy. Berlin, Germany: Wiley-VCH (2017).
5. Murrell, M. P., et al. "Spatially resolved electrical measurements of SiO_2 gate oxides using atomic force microscopy." Applied physics letters 62.7 (1993): 786-788.

6. Rommel, Mathias, et al. "Influence of parasitic capacitances on conductive AFM IV measurements and approaches for its reduction." Journal of Vacuum Science & Technology B, Nanotechnology and Microelectronics: Materials, Processing, Measurement, and Phenomena 31.1 (2013): 01A108.
7. Yanev, V., et al. "Comparative study between conventional macroscopic IV techniques and advanced AFM based methods for electrical characterization of dielectrics at the nanoscale." Microelectronic engineering 86.7-9 (2009): 1911-1914.
8. Carlson, Thomas. Photoelectron and Auger spectroscopy. Springer Science & Business Media, 2013.
9. Briggs, David. "Practical surface analysis." Auger and X-Ray Photoelecton Spectroscopy 1 (1990): 151-152.
10. Bialkowski, Stephen E. Photothermal spectroscopy methods for chemical analysis. Vol. 177. John Wiley & Sons (1996).
11. Hofmann, S. "Characterization of nitride coatings by Auger electron spectroscopy and x-ray photoelectron spectroscopy." Journal of Vacuum Science & Technology A: Vacuum, Surfaces, and Films 4.6 (1986): 2789-2796.
12. Feldman, Leonard C., and James W. Mayer. "Fundamentals of surface and thin film analysis." North Holland, Elsevier Science Publishers, Amsterdam, The Netherlands (1986).
13. Oura, K., et al. "M. Katayama M." Surface Science: An Introduction" Springer, Berlin (2003).
14. Kittel, Charles, Paul McEuen, and Paul McEuen. Introduction to solid state physics. Vol. 8. New York: Wiley (1996).
15. Palmberg, Paul William. Handbook of Auger electron spectroscopy: a reference book of standard data for identification and interpretation of Auger electron spectroscopy data. Physical Electronics Industries (1972).

16. Seah, M. Pl, and W. A. Dench. "Quantitative electron spectroscopy of surfaces: A standard data base for electron inelastic mean free paths in solids." Surface and interface analysis 1.1 (1979): 2-11.
17. Egerton, Ray F. Electron energy-loss spectroscopy in the electron microscope. Springer Science & Business Media (2011).
18. Werner, Wolfgang SM. "Electron transport in solids for quantitative surface analysis." Surface and Interface Analysis: An International Journal devoted to the development and application of techniques for the analysis of surfaces, interfaces and thin films 31.3 (2001): 141-176.

Chapter 3

Exfoliation of large-area high-quality two-dimensional mica nanosheets on substrate

Mechanical exfoliations and transfer techniques led to understanding of novel physical phenomena of two-dimensional (2D) materials. The original exfoliation method, which remained largely unchanged during the past decade, provides relatively small flakes with moderate yield. Here, we present a conventional approach to exfoliate single-layer or few-layer nanosheets from cleavable layered crystals using a polyurethane hand roller. The sample was a single-crystal oxide of pure artificially-synthesized phlogopite ($KMg_3AlSi_3O_{10}F_2$), one of mica family. The mica nanosheets with high-quality were extended to more than 100-μm width on Si substrates. The nanosheets down to a single layer (1 nm) were characterized by atomic force microscopy (AFM), and elemental analysis was performed by scanning Auger electron spectroscopy/microscopy (SAM). The preparation of atomically thin insulating crystalline mica sheets will enable the fabrication of ultrathin, defect-free insulating substrates, dielectric barriers, or planar electron-tunneling junction.

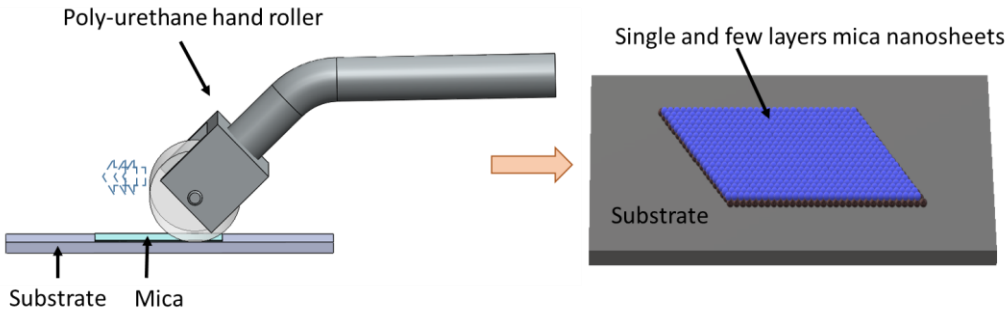

Figure 3: Transferring process of mica nanosheets

3.1 Introduction

The perfection and physical properties of atomically thin two-dimensional (2D) materials are extremely sensitive to their synthesis and growth process. Achieving desired characteristics such as structural uniformity, high carrier mobility, tunable bandgap, and flexibility is the main challenge for

the synthesis and growth of next generation 2D materials. A reliable and optimized growth and manufacturing process is essential for the synthesis of 2D materials with uniform properties for the application in flexible and transparent optoelectronics. Scalable growth techniques such as chemical vapor deposition (CVD) and atomic layer deposition techniques have been used to grow large-area 2D materials such as graphene, [1–5] MoS_2, [6,7] WS_2 [8], and others [9–11] on different substrates. But the development of CVD optimized growth approaches has proven to be a time-consuming process, since phenomena such as the formation of defects [4,12] and grain boundaries [13] happened during the growth process.

To prepare high-quality 2D materials, mechanical exfoliation processes are often performed, leading to understanding of their remarkable physical phenomena [14–21]. Mechanical exfoliation of monolayer or few-layer nanosheets from layered bulk crystals has played a central role to the rapidly accessing of high-quality flakes for exploring novel materials systems. For example, nearly all of the novel properties of graphene were first discovered and measured on mechanically exfoliated flakes [22–24] and other 2D materials such as h-BN, MoS_2 and SnS_2 have gained large attention due to their distinctive properties [25–27]. Also, it can be expected that the exfoliation process will continue to play a prominent role in the development of 2D materials.

The single-crystalline layered structure of pure artificially synthesized phlogopite mica, a phyllosilicate mineral with oxides of aluminum (Al) and magnesium (Mg), and potassium (K) and fluorine (F) in the chemical formula of $KMg_3AlSi_3O_{10}F_2$ makes this material a promising candidate to produce atomically thin insulating crystals by mechanical exfoliation. Moreover, due to its mechanical properties, high dielectric constant, and high resistance to heat, water, and chemical agents, bulk mica has already been extensively used in the electronic industry in many applications as a substrate, heat and electrical insulator, or dielectric barrier. Recently, bulk mica has been also employed as a substrate to fabricate ultra-flat graphene samples [28–33]. The 2D nature of these atomically thin crystalline insulator sheets makes them very interesting candidates in applications

such as insulating barriers in planar tunnel junctions or as flexible substrates for graphene or molecular electronic devices [34–38]. For development of high-quality nanoscale devices, conventional and reliable methods to extend the areal size of 2D mica nanosheets are required, as well as methods to precisely characterize their thickness and chemical components. In this work, we report a mechanical exfoliation process to prepare wider atomically thin mica nanosheets down to one layer (1 nm) on SiO_2/Si, Au/Si, and Ir/Si substrate. A combined characterization of these nanosheets by quantitative optical microscopy and atomic force microscopy (AFM) are presented. We also performed Auger electron spectroscopic (AES) analysis to compare the carbon contaminations on the mica nanosheets prepared in our modified exfoliation process to those prepared with other commonly used mechanical exfoliation technique.

3.2 Experimental Methods

In order to mechanically exfoliate nanosheets from the bulk phlogopite and affix them to the substrates, we first adopted a tool in the exfoliation process, where Scotch tape have been widely used to exfoliate flakes from graphene and other 2D materials. Instead of Scotch tape, we used the tool of a clean polyurethane hand roller with a diameter of 20 mm; this is originally a commercial tool to remove dust from flat surfaces in semiconductor processes without residues (Semiconductive gel roller, EX215-AS, EXSEAL Co., Ltd., Mino, Japan). The viscosity of polyurethane is similar to that of poly-dimethylsiloxane (PDMS) and Scotch tape, but the polyurethane gives lower levels of residues. The outline of the mechanical exfoliation and affixing processes is shown in **Fig. 3.1**. First, the roller was rolled once over the top surface of the bulk mica to thinly exfoliate the surface, and the exfoliated mica sheets were attached to the surface of the roller. Subsequently, the roller was rolled over a substrate so that the sheets on the roller were transferred to the target area on the substrate. The curved surface of the roller was suitable for separating thin mica sheets from the bulk mica and transferring them onto the substrate. To compare the performance of the roller, we also used a PDMS

stamp with a thickness of 0.5 mm to exfoliate the mica nanosheets. For the substrates, we used native oxidized Si wafers (SiO_2/Si) and Si wafers coated with gold (Au/Si) or iridium (Ir/Si) at a thickness of about 10 nm. Before transferring the mica sheets onto the substrate, the SiO_2/Si substrate is ultrasonically cleaned in acetone, and mill-Q water, and then subjected to ozone cleaning to remove ambient hydrocarbon adsorbates from its surface. We heated the substrate for few minutes at 250 °C in air on a conventional laboratory hotplate to evaporate water molecules from the surface of the substrate. Using the poly-urethane hand roller technique, mica nanosheets with thicknesses ranging from hundreds of nanometers down to just one nanometer, corresponding to one layer of the mica, were produced. When mica is mechanically exfoliated, cleavage occurs along the (001) basal plane of a K atom layer (**Fig. 3.2**). As a result, approximately half of the K atoms randomly remain on the surface of the exfoliated mica sheet, while the other half remain on the counter surface of the mica crystal. Inspection by optical microscopy and AFM shows the successful transfer of single and few-layer wide area mica nanosheets on different substrates.

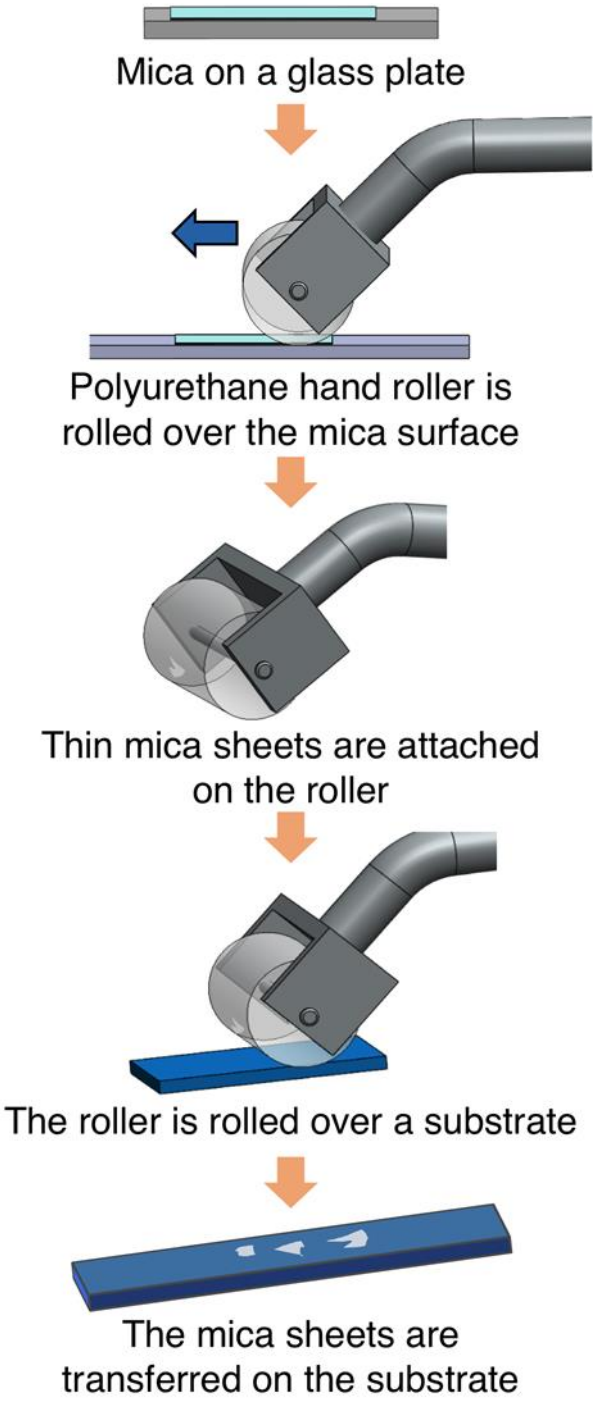

Figure 3.1: Outline of the mechanical exfoliation and affixing process to prepare the 2D mica nanosheets onto the substrate. First, a polyurethane hand roller is rolled over the mica. Subsequently, the exfoliated mica nanosheets on the surface of the roller are transferred and affixed to the substrate by rolling the roller over the substrate. [39]

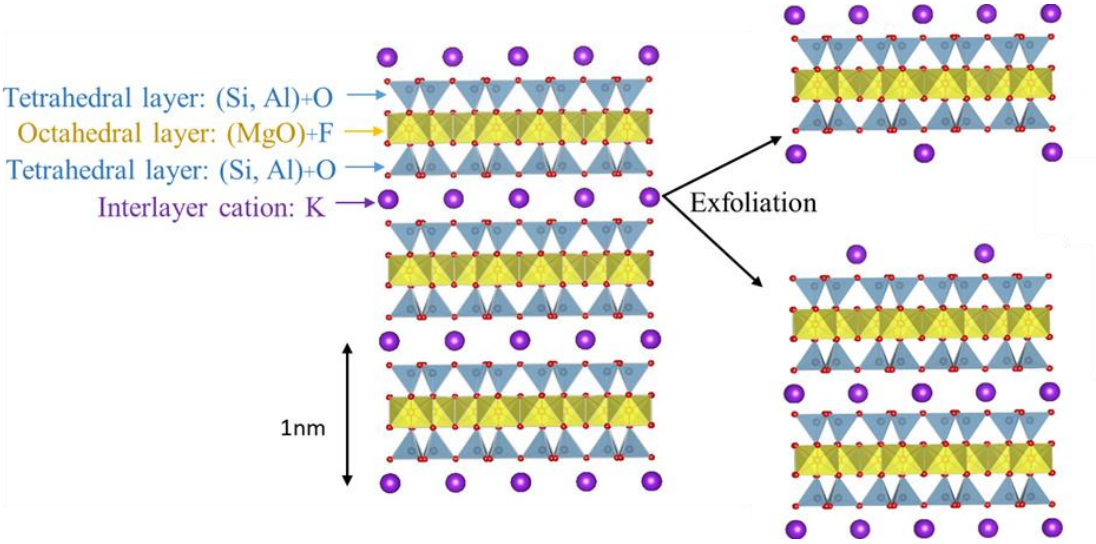

Figure 3.2: Atomistic model of phlogopite ($KMg_3AlSi_3O_{10}F_2$) viewed along the basal plane. The grayish blue polygons are the tetrahedrons composed of Al, Si, and O, where Al and Si atoms exist at a ratio of 1:3. The yellow polygons are the octahedrons composed of Mg, O, and F. The small red spheres denote O atoms at the sites that are connected to the tetrahedrons, and partly F atoms at the sites that are not connected to the tetrahedrons. The large purple spheres denote K atoms. The separation between the K layers is approximately 1.0 nm, which is the unit of thickness of mechanically cleaved phlogopite. [39]

For the gold (Au/Si) or iridium (Ir/Si) substrates, we used native oxidized Si wafers (SiO_2/Si) coated with gold (Au) or iridium (Ir) at a thickness of about 10 nm deposited by DC magnetron sputtering. **Figure 3.3** shows the schematic of the sputtering coating. DC magnetron sputtering coat was conducted in a vacuum chamber with an argon (Ar) gas (99.999%) pressure of 6 Pa at a discharge current of 15 mA with a DC power supply.

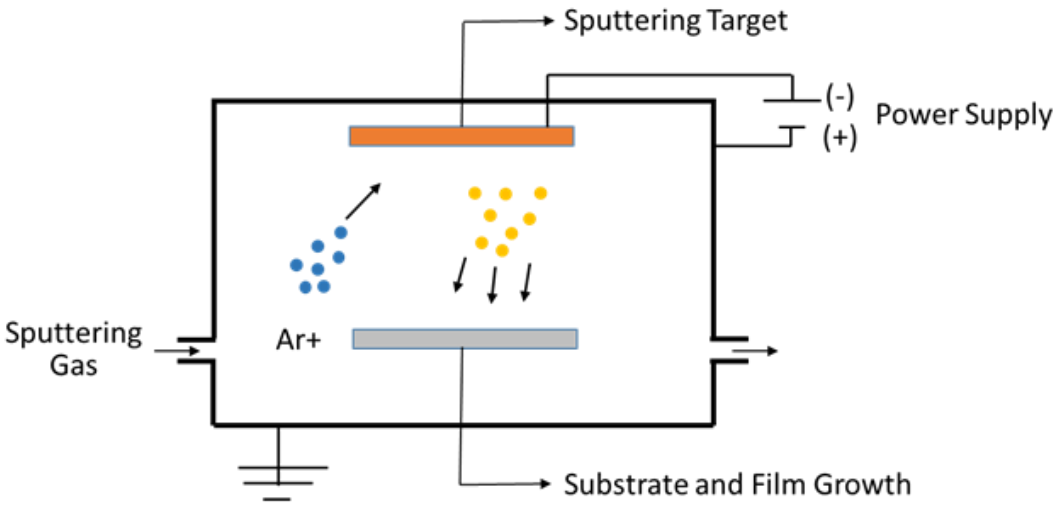

Figure 3.3: Schematic of the DC magnetron stuttering.

3.3 Results and Discussion

Figure 3.4 shows some optical microscopy images of mica nanosheets transferred onto two Si substrates with a 300 nm and a 10 nm SiO_2 thickness. The mica nanosheets on the Si substrate with the 300 nm SiO_2 thickness were more enhanced in contrast, as shown in **Fig. 3.4**(a,b), compared with those on the Si substrate with the thinner oxide. We were able to clearly observe down to one-layer mica nanosheets on the Si substrate, whereas on the 10 nm SiO_2/Si substrate, down to five-layer mica nanosheets were recognized, as shown in **Fig. 3.4**(c,d) . The sizes of nanosheets in **Figs. 3.4**(b) and (d) were about 850 μm × 350 μm with 6 layers and about 1200 μm × 800 μm with 10 layers, respectively. Our modified approach can make it easier to obtain large-area mica nanosheets.

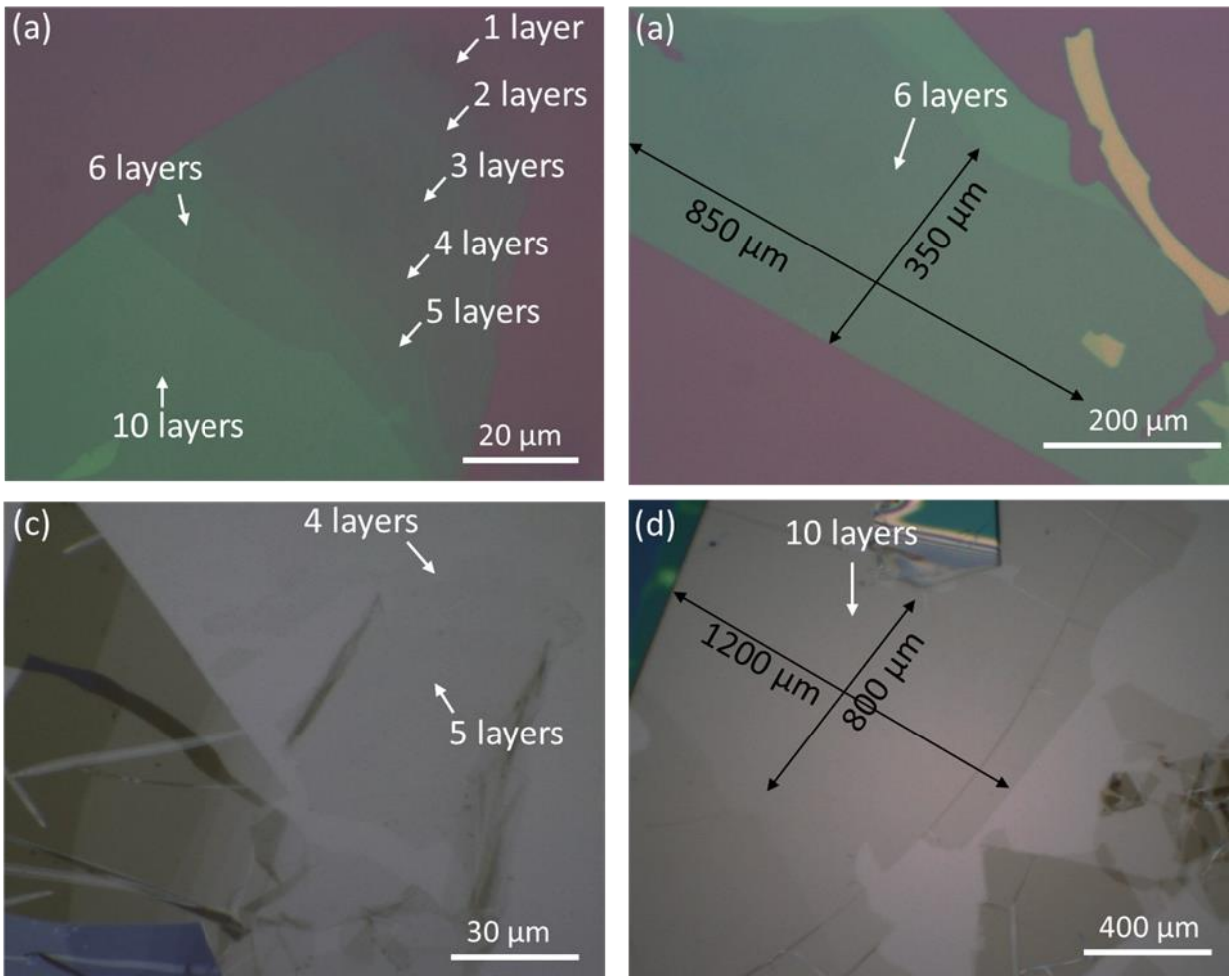

Figure 3.4: Optical microscopy images of mica nanosheets deposited on SiO_2/Si substrates. The color and contrast difference over the nanosheets correspond to different thicknesses of the mica nanosheets. (a) Mica nanosheets with thicknesses ranging from 1 to 20 nm on the 300 nm SiO_2 /Si substrate. (b) Larger area 6 layers (6 nm) mica nanosheets on the 300 nm SiO_2/Si substrate. (c) Four to several layers and (d) 10 layers extended area of mica nanosheets on a 10 nm SiO_2/Si substrate.

AFM imaging would provide an independent measurement of the thickness and morphology of 2D materials. The typical contact-mode topographic AFM images of mica nanosheets on the SiO_2/Si substrates are shown in **Figs. 3.5** (a) and (b), and those on the Au-coated Si (Au/Si) and the Ir-coated Si (Ir/Si) substrates are shown in **Figs. 3.5** (c) and (d), respectively. To evaluate their thicknesses, we examined the cross-sectional profiles through the boundary between the SiO_2 surface and the mica nanosheets in the respective images, as shown below the AFM images. The minimum height

differences between the substrate and the mica nanosheets in **Figs. 3.5 (**a) and (b) were 1 and 5 nm, corresponding to one- and five-layer mica, respectively. Although the dimensions of single layer mica nanosheets fabricated by mechanical exfoliation processes, such as with Scotch tape, are usually not much larger than 1 μm × 1 μm, we were able to prepare single layer mica nanosheets with dimensions of ~10 μm ×10 μm using the polyurethane hand roller (**Fig. 3.5** (a)). The dimensions of the five-layer thick mica nanosheets reached to several hundredth μm in width (**Fig. 3.5** (b)). We also observed few layers mica nanosheets with larger area on the Au/Si and Ir/Si substrate (**Figs. 3.5** (c) and (d).

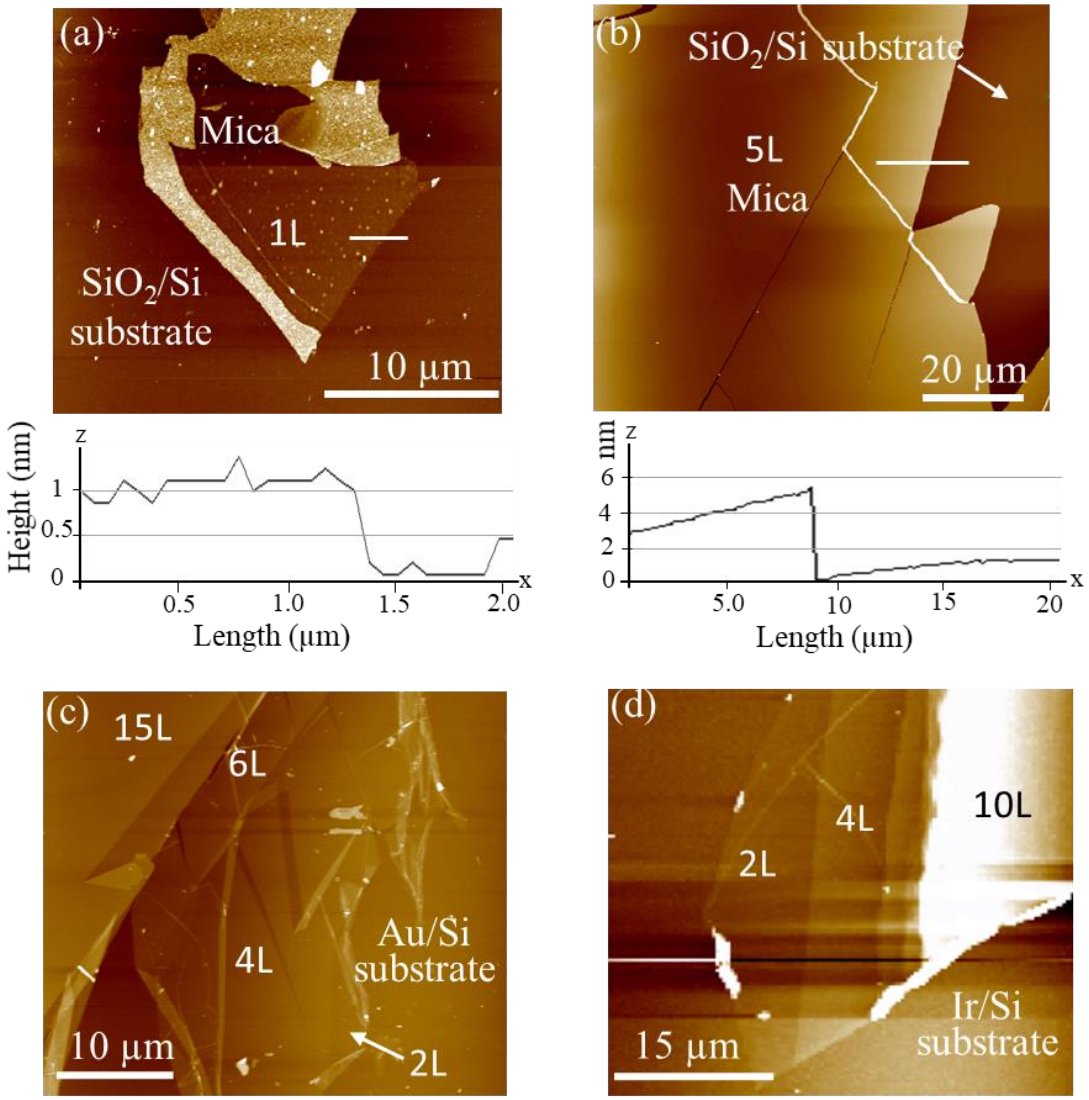

Figure 3.5: AFM images of mica nanosheets mechanically exfoliated to (a) 1 nm and (b) 5 nm thickness, affixed on the SiO2/Si substrates. AFM images of several layer mica nanosheets on (c)

Au/Si and (d) Ir/Si substrates. The typical cross-sectional line profiles along the lines in the images are shown below the images in (a) and (b). The numerals with the character "L" indicate the thickness of the mica nanosheets in the unit of one mica layer (1 nm) measured from the cross-sectional line profiles. [39]

It should be noted that the mica nanosheets often showed ripples and wrinkles, probably because of formation of water bubbles between the nanosheet and substrate. In our experiment, we found that monolayer or bilayers mica showed ripple because of existing water molecules between the thin mica and the substrate. Thus, we heated the substrates before transferring the mica nanosheets, resulting in smooth mica nanosheets without ripples and wrinkles, as shown in **Fig. 3.6**.

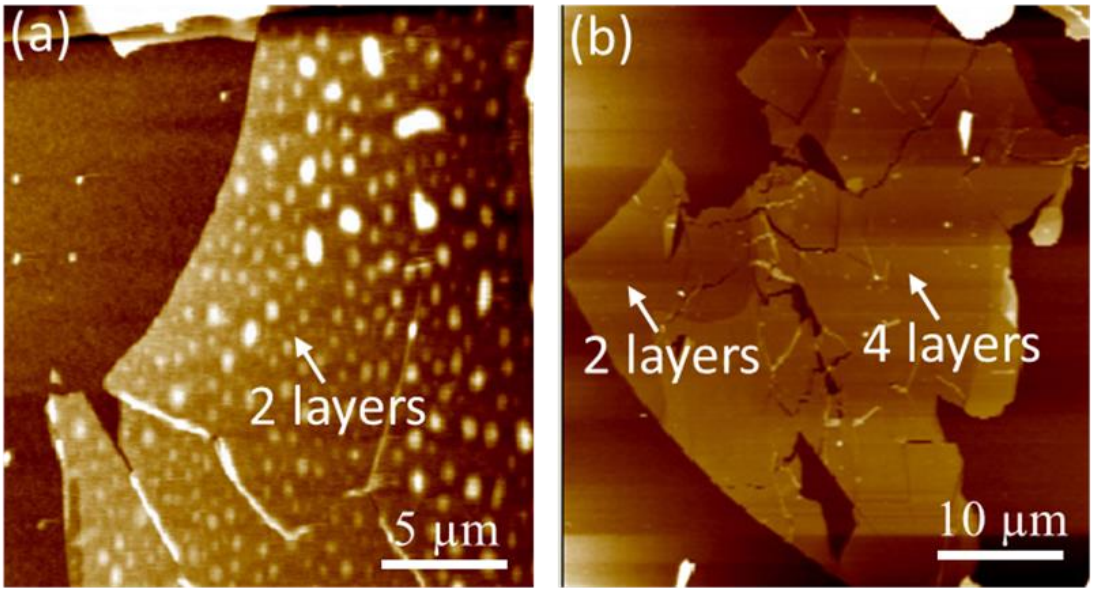

Figure 3.6: Bilayer mica nanosheets transfer on SiO_2/Si substrate (a) with and (b) without performing heating treatment at 250^0C for few minutes of the substrate before transferring mica on it. [39]

To examine the cleanliness of mica nanosheets exfoliated with our modified process, we performed the AES analysis of mica nanosheet surfaces (the details of the AES analysis are explained in the next chapter). From the AES spectra, we observed all the mica elements with detecting C_{KLL} Auger peaks at 272 eV close to the K_{LMM} peaks at 252 eV, as shown in **Fig. 3.7** (a). The degree of carbon contamination depends on the preparation method [40-44]. The AES spectra around the C_{KLL} peaks

of 10-layer-thick mica nanosheets on the Au/Si substrate prepared using the polyurethane hand roller and a stamp of a thin PDMS sheet are shown in **Fig. 3.7** (b). The carbon peak intensities were higher for the mica nanosheets exfoliated with the PDMS stamp. This tendency of the difference in the C peaks using the two different tools was confirmed for other mica nanosheet samples. This suggests that the higher carbon amount originated from the surface of the PDMS stamp. PDMS contains uncross-linked dimethylsiloxane oligomers, which are known to be present on its surface [40,42]. Although the polyurethane hand roller did not contain these undesirable species, the carbon peak did not disappear, which was possibly attributed to contamination from the laboratory environment during the process as we performed the exfoliation process in air.

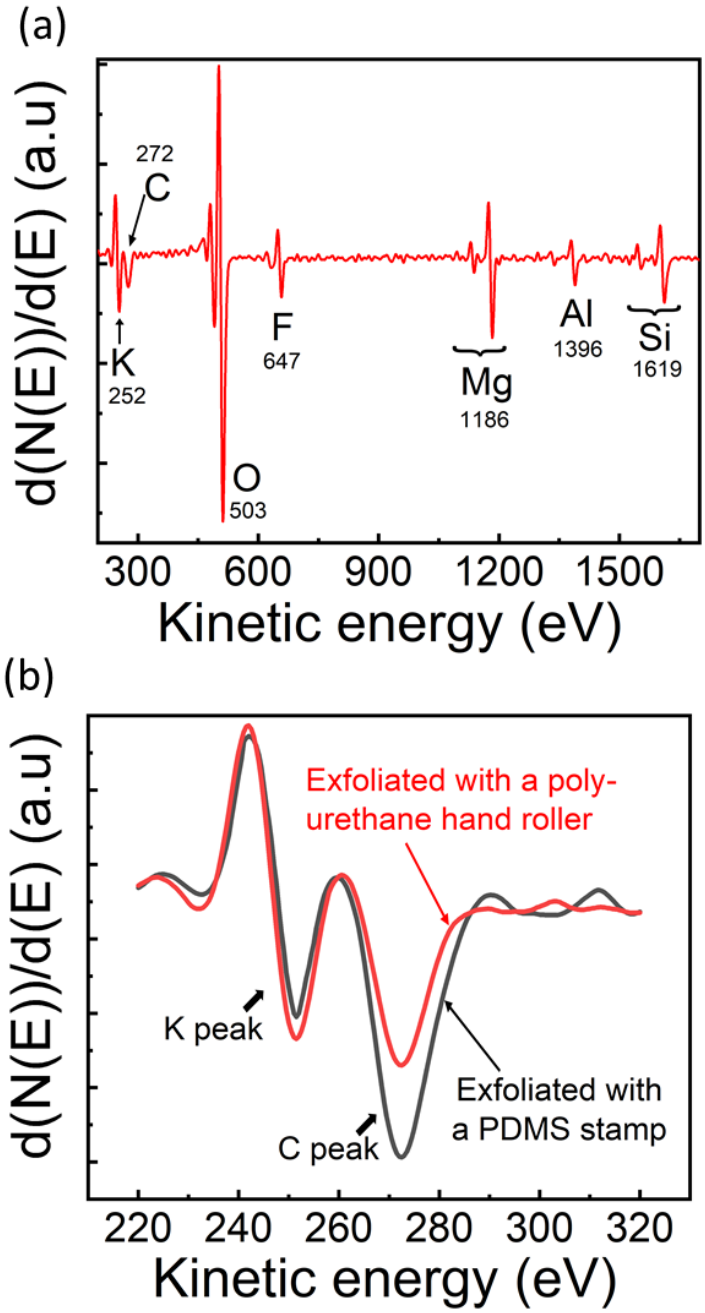

Figure 3.7: (a) AES spectra of 10-layer-thick mica nanosheets on the SiO2/Si substrate. The peaks denoted by the element symbols are the mica elements except C peaks at 272 eV. The C peaks were subjected to hydrocarbonous contaminations on the sample surface. (b) AES spectra to compare the difference in the contamination on the nanosheets prepared with the polyurethane hand roller (red) and the PDMS stamp (black). [39]

It is widely known that mica has a layered structure with the potassium (K) ion layers sandwiched between aluminosilicate layers. The aluminosilicate layer, which is a negatively charged oxide layer because of the substitution of a quarter of the Si^{4+} ions by Al^{3+} ions, is bounded together electrostatically with a layer of K^+ atoms, as shown in the model of **Fig. 3.2**. Since the attractive force between the K^+ layers and the aluminosilicate layers are weak, cleavage occurs easily along their interface. On the other hand, the interactions between the mica surface and the Si substrate during exfoliation are van der Waals forces. Exfoliation of mica sheets on the Si substrate represents a competition between the weak electrostatic force at the K^+ layer and the van der Waals forces between the bottom surface of mica sheet and the surface of the Si substrate, which are facing each other. When the adhesive force between the bottom of the mica sheet and the substrate exceeds the force between the mica layers, the mica sheet can be separated from the layered mica, leaving the thin mica nanosheet on the substrate surface. **Figure 3.8** gives a schematic diagram of the key steps of modified mica exfoliation process, and illustrates how the solid curve surface of the poly-urethane hand roller can increase the interaction at the mica/substrate interface and thus enhance the exfoliation process. When the roller together with few layers mica on its surface is pressed over the substrate, more uniform contact is established between the outermost mica layer and the support substrate which increased van der Waals force driven by an increase in pressure at the interface. The roller increases the force between mica and substrate surface by establishing pressure difference, increased contact area, and decreased overall contact distance. As a result, when the roller is rolled, separations occurred between the mica layers and monolayers or few layers of mica is transferred from the roller surface onto substrate surface. Similar mechanism happened when the roller is rolled over the bulk mica to transfer mica sheets onto the roller surface. Sometimes monolayer or few layers mica flakes that attached on the roller surfaces from the bulk mica are transferred onto the substrate surface directly. Upon cleavage of mica surface exhibits a hexagonal arrangement of Si (1/4 Al substitution) and O atoms partly covered by potassium ions over the exposing surface [45].

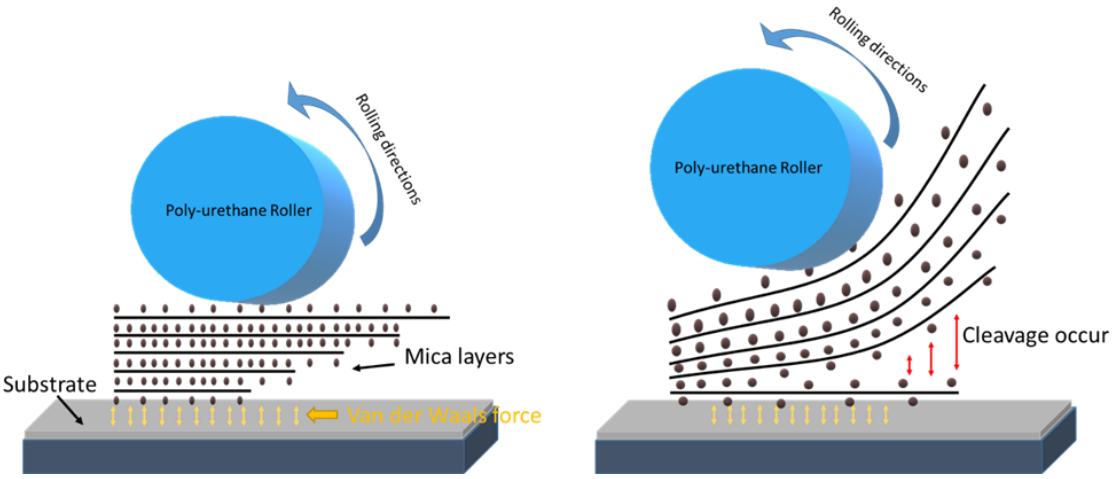

Figure 3.8: Key steps of the modified exfoliation process for 2D materials. (a) Increased pressure by the roller causes a small and uniform spacing between mica and substrate which in turn enhances the van der Waals interaction at the interface. (b) Separation between the mica layers occurred as the roller is started to rolling over the substrate.

3.4 Conclusion

We have successfully deposited atomically thin nanosheets of phlogopite mica with thickness down to a single layer (1 nm) and few layers with an area of several hundredth square micrometers on SiO_2/Si, Au/Si, and Ir/Si substrates. Mechanical exfoliation of mica nanosheets with a clean polyurethane roller can easily provide large area mica nanosheets. The AES analysis demonstrated that our modified exfoliations mica had a low level of hydrocarbon contamination compared with the commonly used PDMS exfoliations process. We suggest that the exfoliation approach demonstrated here is applicable to a wide range of 2D materials. Hence, our conventional method possibly accelerates the exploration of new 2D materials by providing an efficient pathway to large nanosheets derived from layered crystals via exfoliation.

References

1. Bhaviripudi, Sreekar, et al. "Role of kinetic factors in chemical vapor deposition synthesis of uniform large area graphene using copper catalyst." Nano letters 10.10 (2010): 4128-4133.
2. Sutter, E., P. Albrecht, and P. J. A. P. L. Sutter. "Graphene growth on polycrystalline Ru thin films." Applied Physics Letters 95.13 (2009): 133109.
3. Sutter, P. W., P. M. Albrecht, and E. A. Sutter. "Graphene growth on epitaxial Ru thin films on sapphire." Applied Physics Letters 97.21 (2010): 213101-213103.
4. Virojanadara, Chariya, et al. "Homogeneous large-area graphene layer growth on 6 H-SiC (0001)." Physical Review B 78.24 (2008): 245403-245408.
5. Ge, Wanyin, et al. "Large-scale synthesis of NbS_2 nanosheets with controlled orientation on graphene by ambient pressure CVD." Nanoscale 5.13 (2013): 5773-5778.
6. Wang, Shanshan, et al. "Shape evolution of monolayer MoS_2 crystals grown by chemical vapor deposition." Chemistry of Materials 26.22 (2014): 6371-6379.
7. Wang, Xinsheng, et al. "Controlled synthesis of highly crystalline MoS_2 flakes by chemical vapor deposition." Journal of the American Chemical Society 135.14 (2013): 5304-5307.
8. Zhang, Yu, et al. "Controlled growth of high-quality monolayer WS_2 layers on sapphire and imaging its grain boundary." ACS nano 7.10 (2013): 8963-8971.
9. Huang, Jing-Kai, et al. "Large-area synthesis of highly crystalline WSe_2 monolayers and device applications." ACS nano 8.1 (2014): 923-930.
10. Lu, Xin, et al. "Large-area synthesis of monolayer and few-layer $MoSe_2$ films on SiO2 substrates." Nano letters 14.5 (2014): 2419-2425.
11. Brent, Jack R., Nicky Savjani, and Paul O'Brien. "Synthetic approaches to two-dimensional transition metal dichalcogenide nanosheets." Progress in Materials Science 89 (2017): 411-478.
12. Colombo, Luigi, et al. "Growth kinetics and defects of CVD graphene on Cu." EC Transactions 28.5 (2010): 109-114.

13. Huang, Pinshane Y., et al. "Grains and grain boundaries in single-layer graphene atomic patchwork quilts." Nature 469.7330 (2011): 389-392.
14. Novoselov, Kostya S., et al. "Electric field effect in atomically thin carbon films." science 306.5696 (2004): 666-669.
15. Levendorf, Mark P., et al. "Graphene and boron nitride lateral heterostructures for atomically thin circuitry." Nature 488.7413 (2012): 627-632.
16. Radisavljevic, Branimir, et al. "Single-layer MoS_2 transistors." Nature nanotechnology 6.3 (2011): 147-150.
17. Novoselov, Kostya S., et al. "Two-dimensional gas of massless Dirac fermions in graphene." nature 438.7065 (2005): 197-200.
18. Wei, Xiaoding, et al. "Recoverable slippage mechanism in multilayer graphene leads to repeatable energy dissipation." ACS nano 10.2 (2016): 1820-1828.
19. Nair, Rahul Raveendran, et al. "Fine structure constant defines visual transparency of graphene." Science 320.5881 (2008): 1308-1308.
20. Schedin, Fredrik, et al. "Detection of individual gas molecules adsorbed on graphene." Nature materials 6.9 (2007): 652-655.
21. Withers, Freddie, et al. "Electron transport of WS_2 transistors in a hexagonal boron nitride dielectric environment." Scientific reports 4 (2014): 4967-4971.
22. Zhang, Yuanbo, et al. "Experimental observation of the quantum Hall effect and Berry's phase in graphene." nature 438.7065 (2005): 201-204.
23. Masubuchi, S., et al. "Observation of quantum Hall effect in mono-and bi-layer graphene using pulse magnet." Journal of Physics: Conference Series. Vol. 334. No. 1. IOP Publishing, 2011.
24. Ferrari, Andrea C., et al. "Raman spectrum of graphene and graphene layers." Physical review letters 97.18 (2006): 187401-187403.
25. Lee, Gwan-Hyoung, et al. "Flexible and transparent MoS_2 field-effect transistors on hexagonal boron nitride-graphene heterostructures." ACS nano 7.9 (2013): 7931-7936.

26. Mak, Kin Fai, et al. "Atomically thin MoS_2: a new direct-gap semiconductor." Physical review letters 105.13 (2010): 136805-136809.
27. Strait, Jared H., Parinita Nene, and Farhan Rana. "High intrinsic mobility and ultrafast carrier dynamics in multilayer metal-dichalcogenide MoS_2." Physical Review B 90.24 (2014): 245402-245411.
28. Lui, Chun Hung, et al. "Ultraflat graphene." Nature 462.7271 (2009): 339-341.
29. Geringer, V., et al. "Intrinsic and extrinsic corrugation of monolayer graphene deposited on SiO_2." Physical review letters 102.7 (2009): 076102-076106.
30. Meyer, Jannik C., et al. "The structure of suspended graphene sheets." Nature 446.7131 (2007): 60-63.
31. Teague, M. L., et al. "Evidence for strain-induced local conductance modulations in single-layer graphene on SiO_2." Nano letters 9.7 (2009): 2542-2546.
32. Castellanos-Gomez, Andres, Nicolas Agraït, and Gabino Rubio-Bollinger. "Dynamics of quartz tuning fork force sensors used in scanning probe microscopy." Nanotechnology 20.21 (2009): 215502-215566.
33. Ponomarenko, L. A., et al. "Effect of a high-κ environment on charge carrier mobility in graphene." Physical review letters 102.20 (2009): 206603-206607.
34. Castellanos-Gomez, Andres, et al. "Atomically thin mica flakes and their application as ultrathin insulating substrates for graphene." Small 7.17 (2011): 2491-2497.
35. Low, Chong Guan, et al. "Graphene field effect transistors with mica as gate dielectric layers." Small 10.20 (2014): 4213-4218.
36. Bitla, Yugandhar, and Ying-Hao Chu. "MICAtronics: A new platform for flexible X-tronics." FlatChem 3 (2017): 26-42.
37. Rudenko, A. N., et al. "Graphene adhesion on mica: Role of surface morphology." Physical Review B 83.4 (2011): 045409-045415.

38. Low, Chong Guan, and Qing Zhang. "Ultra-thin and Flat Mica as Gate Dielectric Layers." Small 8.14 (2012): 2178-2183.
39. Razzakul, Islam Mohammad, and Masahiko Tomitori. "Evaluation of the discrete thickness of exfoliated artificially synthesized mica nanosheets on silicon substrates: Toward characterization of the tunneling current through the nanosheets." Applied Surface Science 532 (2020): 147388-147401.
40. Jain, Achint, et al. "Minimizing residues and strain in 2D materials transferred from PDMS." Nanotechnology 29.26 (2018): 265203-265213.
41. Tongay, Sefaattin, et al. "Tuning interlayer coupling in large-area heterostructures with CVD-grown MoS_2 and WS_2 monolayers." Nano letters 14.6 (2014): 3185-3190.
42. Meitl, Matthew A., et al. "Transfer printing by kinetic control of adhesion to an elastomeric stamp." Nature materials 5.1 (2006): 33-38.
43. Allen, Matthew J., et al. "Soft transfer printing of chemically converted graphene." Advanced Materials 21.20 (2009): 2098-2102.
44. Glasmästar, Karin, et al. "Silicone transfer during microcontact printing." Langmuir 19.13 (2003): 5475-5483.
45. Müller, K., and C. C. Chang. "Electric dipoles on clean mica surfaces." Surface Science 14.1 (1969): 39-51.

Chapter 4

Discrete Thickness Measurement of Mica Nanosheets by Auger Electron Spectroscopy on Substrates: Toward Characterization of the Tunneling Current through the Nanosheets

Insulating two-dimensional (2D) single-crystal oxide of pure artificially-synthesized phlogopite (KMg3AlSi3O10F2) mica nanosheets were characterized by atomic force microscopy (AFM), and elemental analysis was performed by scanning Auger electron spectroscopy/microscopy (SAM). The elemental peak intensities of Auger electron spectroscopy (AES) spectra obtained by the SAM depended on the number of layers of the nanosheets up to five layers. Based on the thickness dependence intensity, we propose a conventional method to evaluate their thickness using the SAM. We also measured the current–voltage characteristics of metal–nanosheet–metal contacts using conductive AFM, and evaluated the tunneling barrier height. This study demonstrates the potential of the mica nanosheets with discrete thickness.

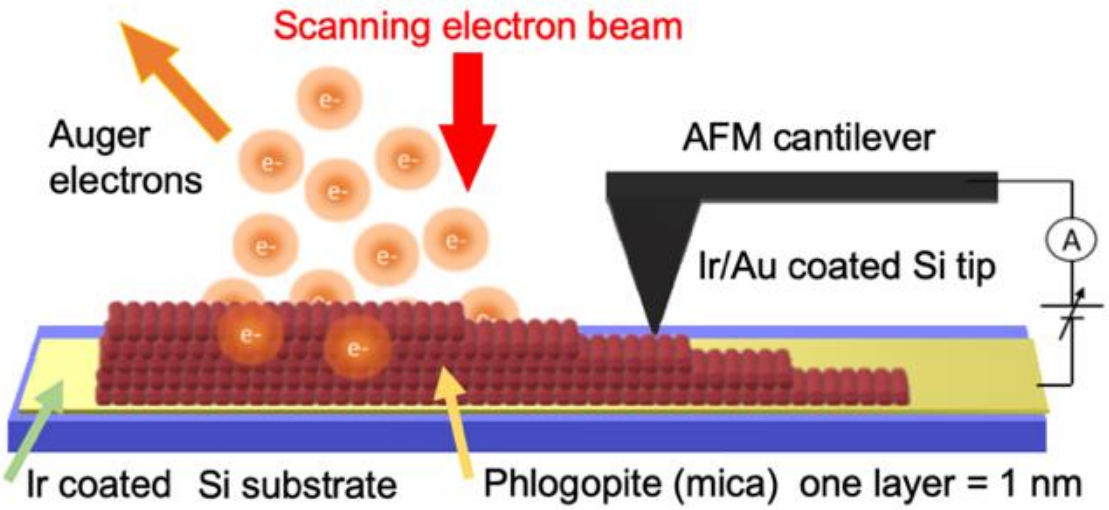

Figure 4: Characterizing mica nanosheets using surface sensitive analyzing methods, and established a method to calibrate the thickness of mica nanosheets by AES

4.1 Introduction

The field of two-dimensional (2D) materials with atomic or molecular thickness represent a broad spectrum of materials with exceptional physical and electronic properties that has witnessed several significant advancements in a short period of time [1-4]. Since the successful exfoliation of graphene a single atomic carbon layer with unique optoelectronic properties has paved the way to study the interesting family of 2D materials [5,6]. Apart from graphene, significant research effort has been directed toward 2D semiconducting materials such as boron nitride (h-BN) [7,8], transitions metal dichalcogenides [9,10], and layered transition metal oxides with wide band gap energies [11,12]. Those materials have significant effect on the advancement toward semiconductor industries as they are extremely thin and transparent, and their chemical structure makes them very strong to the application for flexible electronics. Another fascinating 2D materials 'mica' one of the groups of sheet silicate (phyllosilicate) minerals, is an oxide with a band gap of ~7eV, and has a nearly perfect basal cleavage plane of (001) [13,15]. Mica as 2D materials has prominent characteristic application in the electronic and electrical industries because of its optical transparency, uniform high dielectric constant and mechanical strength incorporated with high resistance to heat, water, and chemical agents. Owing to these characteristics, mica shows great potential from the viewpoint of application as a 2D material, especially as a single crystalline oxide [16,18].

The unique properties of mica nanosheets in the applications to electronic industries are strongly dependent on the thickness and interaction with the underlying substrate. With regard to the development of devices using 2D mica nanosheets, a conventional and reliable method to evaluate their precise thickness is of great importance when it comes to several atomic layers. While optical microscopy can provide quantitative information about the thickness of 2D mica nanosheets exfoliated from bulk mica, a specified substrate such as a SiO_2/Si wafer with a well-defined oxide thickness is needed to enhance the contrast of optical images [19,20]. Atomic force microscopy

(AFM) can be a powerful alternative to measure the thickness on flat substrates [21,22], though only the steep height difference can be measured at the periphery of the nanosheet with respect to the level of substrate and it is poor in time efficiency when a wide area is scanned. Furthermore, it is crucial to analyze the atomic species of the 2D layered materials, including contaminations covering their surfaces and residues between the interfaces of layers, which are often introduced in their fabrication processes and markedly change the properties of 2D layered materials.

In this work, we establish the basis to determine the thickness of few layer mica on substrates such as SiO_2/Si wafers and gold-coated Si wafers using scanning Auger electron microscopy/spectroscopy (SAM) as well as AFM, in regard to their 2D shapes and atomic species. Auger electron spectroscopy (AES) possesses is highly chemical sensitivity as a surface analytical technique, based on the kinetic energy spectrum of electrons backscattered from the sample irradiated with an accelerated electron beam [23,24]. In SAM, the electron beam is focused on a sub-micrometer scale and scanned over the sample surface for elemental mapping analysis, simultaneously scanning electron microscopy (SEM) images being observed. It is noted that the AES is very sensitive to the surface regions in the nanometer depth, benefit to analysis of the nanosheets [25-29]. The SAM routinely used to determine the ultra-thin film thickness for grapheme. Although, the SAM/SEM are not usually applied to insulating materials because of terrible charging effects induced by irradiation of the electron beam, the analysis can be conducted due to the thin layers, where the electron beam penetrates mostly. We also discuss an analytical method to evaluate the thickness in regard to the inelastic mean free path (IMFP) of Auger electrons passing through the mica layers. The current–voltage (I–V) curves were measured over mica nanosheets with different thicknesses by conductive AFM to investigate the correlation with the thickness.

4.2 Methods and Material

To explore the potential of SAM/SEM for the thickness characterization, a single crystal of artificially synthesized pure phlogopite mica ($KMg_3AlSi_3O_{10}F_2$) is used with a size of 10 mm × 10 mm × 0.5 mm was purchased from Itoh Kikoh Co., Ltd. To exfoliate the mica nanosheets from bulk and affix them on the substrtates, we used a polyurethane hand roller. The outline of the mechanical exfoliation and affixing processes is described in **chapter 3**. For the substrates, we used native oxidized Si wafers and the Si wafers coated with gold and iridium at a thickness of about 10 nm by DC magnetron sputtering. The thickness and extent of the samples on the substrates were characterized with an AFM setup (SPM 5500, Agilent Technologies, Inc., C) operated in contact mode in air. The I–V curves were recorded using the same setup as conductive AFM in a chamber filled with pure dry Ar gas (99.999%) to decrease the electric current through the water layers covering the surfaces of the mica nanosheets. These current measurements were performed with an Au-coated conductive Si cantilever over-coated with Ir by DC magnetron sputtering at a thickness of 5 nm to increase the durability of the conductive coating over the Si tip apex. The chemical components of the samples were analyzed using a SAM setup (SAM670, ULVAC-PHI, Inc., Chigasaki, Japan) with a cylindrical mirror analyzer set at 42° of the angle of electron emission from the sample normal, while the SEM images were observed using the SAM setup. The energy and current of the primary electron beam were 10 keV and ~10 nA, respectively, a beam diameter of about 30 nm on the sample surface with ready achievable $l0^{-10}$ Torr SAM vacuum chamber. The AES spectra were obtained in detection of electron counting with an energy sweep with 0.5 eV/step at 20 ms/step and averaged over four energy sweep cycles. The graphs of the spectra were displayed in differential form through numerical calculation with the parameter of 21-point differentiation and smoothing from the spectra data collected by electron counting using the software of the SAM.

4.3 Results and Discussion

Typical topographic AFM images of single to few-layers mica nanosheets on the SiO_2/Si, Au-coated Si (Au/Si) and Ir-coated Si (Ir/Si) substrates are shown in **Fig. 3.5**. For elemental analysis of the nanosheets, SAM analysis was performed. A typical SEM image of the mica nanosheets on the SiO_2/Si substrate is shown in **Fig. 4.1** (a), which was recorded using the SEM function of SAM. The sample area in the SEM image was also observed by AFM (**Fig. 4.1** (b)). By comparison, it was deduced that the brightest flat region in the SEM image in **Fig. 4.1** (a) corresponded to a 10-layer mica nanosheet. The thickness was evaluated from the cross-sectional line profile in the AFM image, and the second brightest region corresponded to five mica layers. Notably, the single mica layer also showed faint brightness in the SEM image with respect to the brightness of the SiO_2/Si substrate (the SEM images are not shown). The brightness differences in SEM images of mica nanosheets can be useful to estimate the thickness differences, and the scan time of the SEM image was much faster than that of the AFM image (almost 1/10 for our AFM setup with respect to that of SEM in **Fig. 4.1**). Because brighter in the SEM image means higher emission rate of secondary electrons, the electric potential at the surface of the thicker mica nanosheet might be slightly negative owing to the higher resistivity of the thicker nanosheet under electron beam irradiation. It is likely that the electrons at the surface can pass through the thin mica nanosheets by electron tunneling and/or because of the surface leakage current on the mica. Since mica is an insulating material, it is generally difficult to produce SEM images of bulk mica owing to image disturbance mainly because of electrical charging. However, for the mica nanosheets, we routinely produced SEM images of mica nanosheets thicker than several tens of nanometers without any disturbance. In addition, it is worth mentioning that the contrast of the SEM images of the mica nanosheets on the Au/Si and Ir/Si substrates was not very clear compared with that on the SiO_2/Si substrate (**Fig. 4.2**), probably because the strong emission of the secondary electrons from the Au and Ir covering the Si substrate partly concealed the contrast of the mica nanosheets.

A well-known difficulty with imaging bare insulators in SEM is due to the so-called charging effects. These effects lead to the deflection of the incident beam and the emitted secondary electrons (SE) by the external electric field, which is responsible for the distortion of images and sometimes for the impossibility of acquiring them. For example, the negative charge would flip the secondary electron from the surface. The negative charge also reduces the landing energy of the incident electrons, and it increase the field between the surface and secondary electron detector. On the other hand, positive charge re-collects the secondary electron. A voltage contrast mechanism develops in which the potential distribution across the surface is imaged. Some areas appear extremely bright because they are negative relative to the detector and enhance SE collection. Other areas appear black because they are charge positively and suppress the collection of SE. The mechanisms of charging are time-dependent phenomena related to the progressive electric charge storage into the specimen. The trapped charges generate an electric field and this initial electric field rapidly modifies the trajectories of the newly arriving primary electrons, modifying in turn the initial charge distribution and the field it creates.

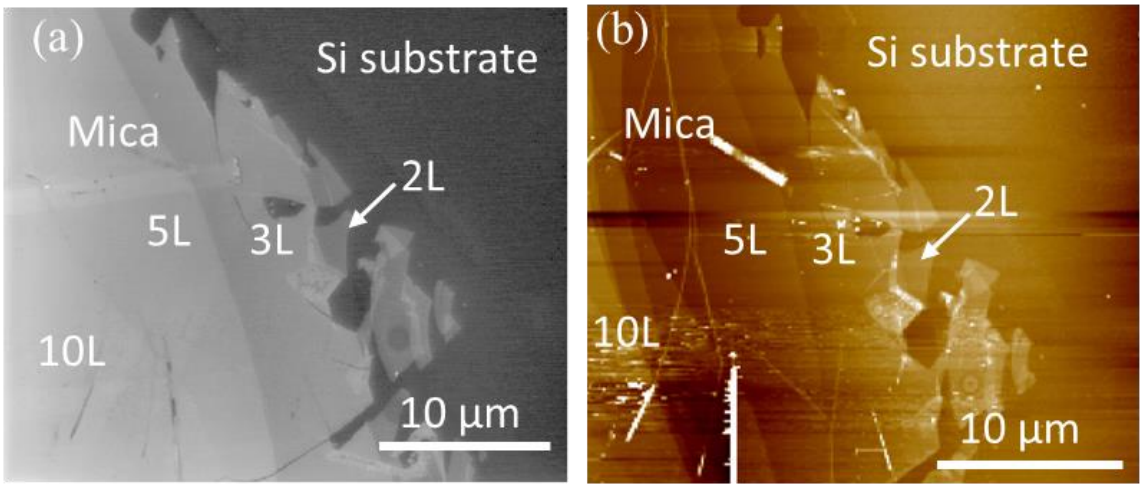

Figure 4. 1: a) SEM image of the area partly covered with 2-, 3-, 5-, and 10-layer mica nanosheets on the SiO_2/Si substrate. b) AFM image of almost the same area observed in (a). The brightness of the SEM image increased step-wise with increasing mica thickness. [30]

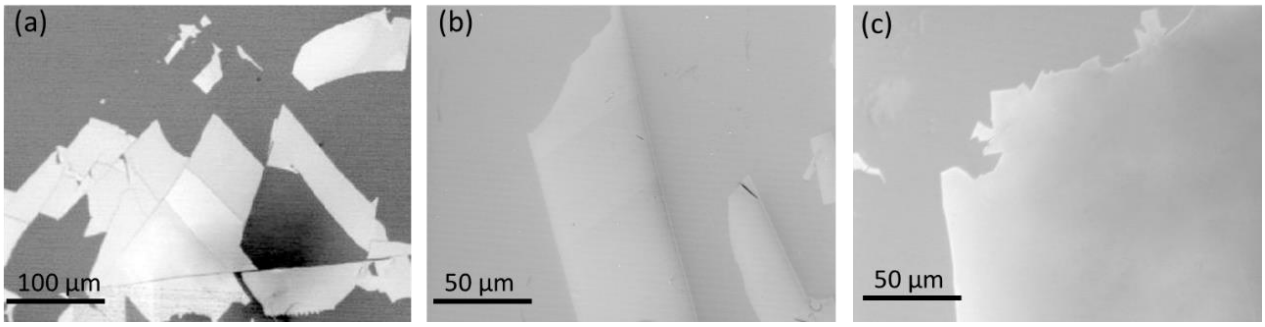

Figure 4. 2: SEM image of few layers mica nanosheets on (a) SiO_2/Si, (b) Au/Si and Ir/Si substrate. Mica have bright contrast on SiO_2/Si substrate compare with Au and Ir coated Si substrate.

The representative scanning electron microscopy (SEM) image of the exfoliated mica sheet on different substrate can be easily observed. As mica is an insulating material, it's difficult to get SEM image because of SEM measurement sample should be conductor. In that case, potassium ion inter-located between mica layers played great role in the SEM measurement for single layer mica sheets. After the exfoliation, inter-located K^+ ion become half amount on both surfaces. When wash with water the K^+ ion remove from the exposing surface. In **Fig. 4.3**, the SEM image shows clear contrast on the indicating point of single layer mica, after wash with water, K^+ ion remove from the top surface and SEM shows less contrast indicated by the white arrows.

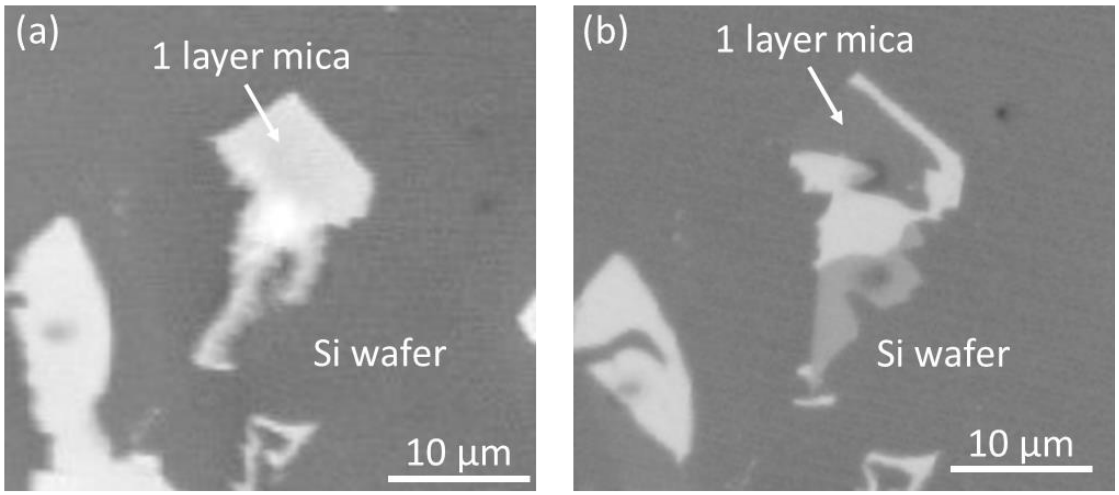

Figure 4. 3: SEM image of single layer mica on SiO_2/Si substrate. The white arrow indicates single layer of mica with K^+ ion (a) before and (b) after wash with water. Before washing with water K^+

ions exist on the top mica surface indicating bright contrast in the SEM image while less image contrast was found as K^+ ions is removed by water washing.

Typical AES spectra from 3 layers and 6 layers mica nanosheets on the SiO_2/Si substrate are shown in **Fig. 4.4**. All of the chemical elements K, O, F, Mg, Al, and Si constituting mica (Phlogopite: $KMg_3AlSi_3O_{10}F_2$) were detected as peaks in the Auger spectra [31]. The AES peaks became higher with increasing thickness of the mica nanosheets from 3 to 6 layers. We also detected C peaks at 272 eV close to the K_{LMM} peaks at 252 eV. This carbon peak in the mica system probably arose from the air during the sample exposing to carbonaceous environment as we performed the exfoliations process in air.

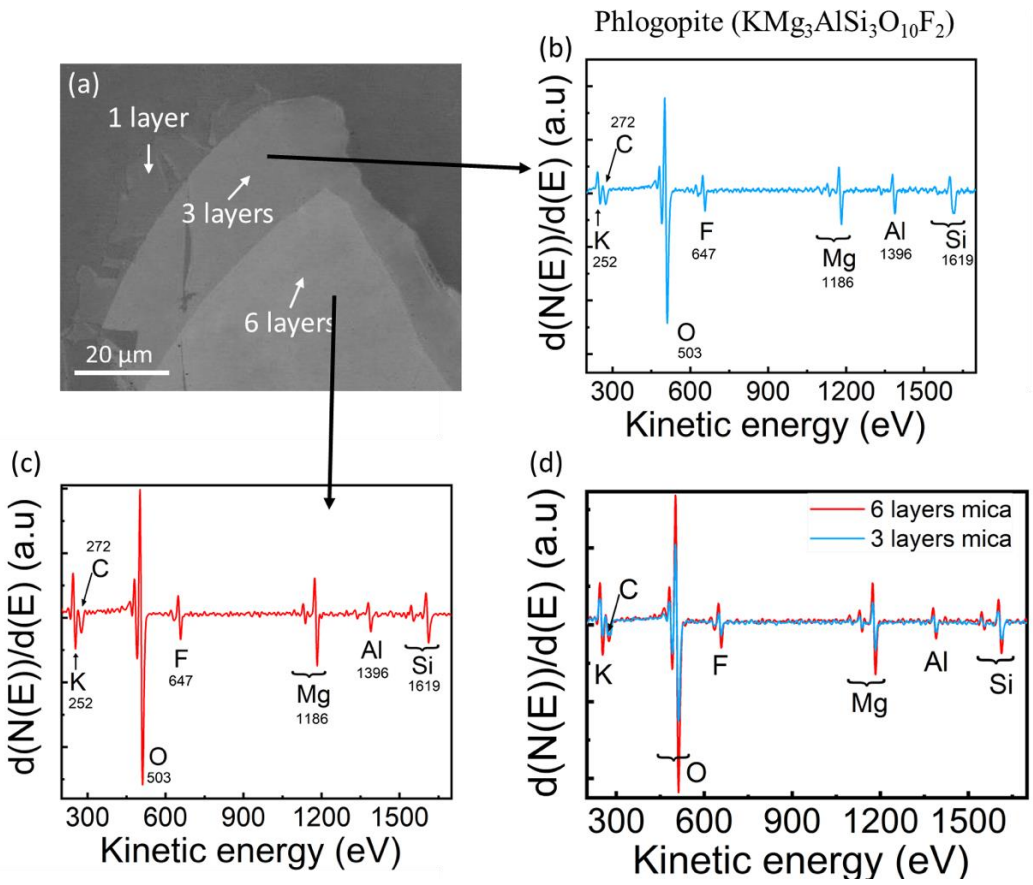

Figure 4. 4: AES spectra of 3 and 6-layer-thick mica nanosheets on the SiO_2/Si substrate. The peak energies of the spectra were the same, although their intensities are different with different thickness.

The peaks denoted by the element symbols are as follows: K_{LMM} at 252 eV, C_{KLL} at 272 eV, O_{KLL} at 503 eV, F_{KLL} at 647 eV, Mg_{KLL} at 1186 eV, Al_{KLL} at 1396 eV, and Si_{KLL} at 1619 eV.

From the **Fig. 4.4**, we observed that as the number of mica layers as increases, the corresponding layers mica elemental peak to peak intensities is changing accordingly. The changing behavior in the peak-to-peak intensities as a function of the number of mica layers up to 20 layers for the SiO_2/Si, Au/Si, and Ir/Si substrates are shown in **Fig. 4.5**. The peak-to-peak intensities of K_{LMM}, O_{KLL}, F_{KLL}, Mg_{KLL}, and Al_{KLL}, as well as the intensity of the Si_{KLL} peak on the Au/Si and Ir/Si substrates, increased with increasing number of mica layers up to five or six layers on the three substrates and became almost constant above five or six layers. In contrast, the intensity of the Si_{KLL} peak decreased on the SiO_2/Si substrate, because the emission of Si_{KLL} from the Si substrate was stronger than that from the mica nanosheets, and the emission from the substrate was gradually concealed with increasing mica nanosheet thickness. The intensities of the Au_{MNN} and Ir_{MNN} peaks decreased with increasing mica nanosheet thickness on the Au/Si and Ir/Si substrates because of attenuation of the Auger electrons passing through the mica nanosheets from the substrates.

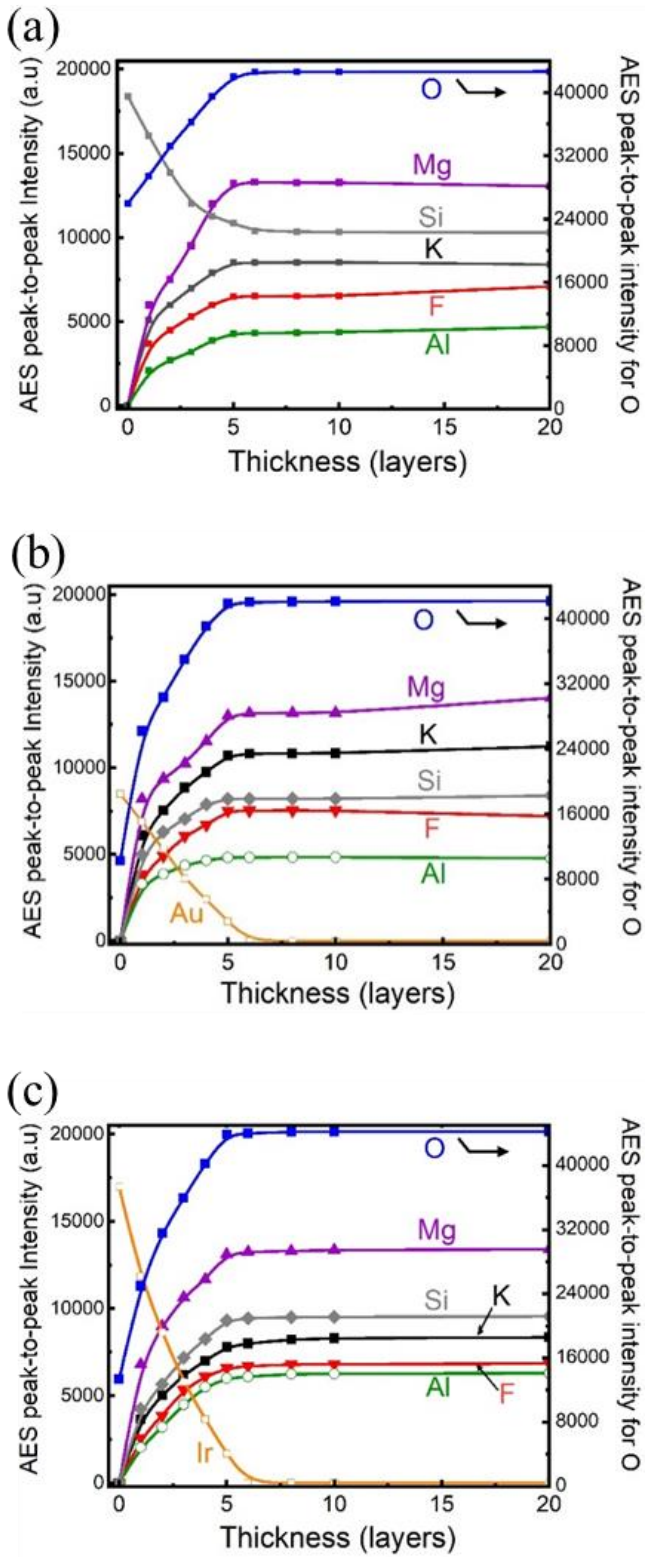

Figure 4. 5: Peak-to-peak intensities of the AES peaks versus the number of the mica layers on the a) SiO_2/Si substrate, b) Au/Si substrate, and c) Ir/Si substrate. [30]

Table 1: AES peak-to-peak intensity ratios with respect to intensity of the Mg peak for 20-layer-thick mica nanosheets and the inelastic mean free path λ at the kinetic energy of the Auger electrons for the element. [30]

Element	Kinetic energy (eV)	SiO_2/Si substrate λ (nm)	Au/Si substrate λ (nm)	Ir/Si substrate λ (nm)
K	252	1.9	2.2	2,1
O	503	4.0	2.5	2.2
F	647	2.3	2.3	2.2
Mg	1186	2.9	2.1	1.7
Al	1396	2.9	1.3	2.5
Si	1619	3.5	1.7	2.1
Ir	1905	—	—	2.8
Au	2024	—	3.3	—

Based on the curves in **Fig 4.7**, we evaluated the inelastic mean free path (IMFP) λ; roughly defined as a travel length for which the intensity decreases to the inverse of Napier's constant *e* [32,33]. Here we assume that each layer, as a unit virtually cleaved out of the mica nanosheet with multiple layer on the substrate, has the same emission rate of Auger electrons, which are summed from the individual elements in each layer, with respect to the primary electron beam I_0; I_0 does not decrease through the mica nanosheet. Then, we derive the following equation to express of the Auger electron intensity $I(N)$ of each element for the mica nanosheet with a thickness of N layers as below.

$$I(N) = \sum_{n=1}^{N} \alpha I_0 \exp\left[-(n-1)d/\lambda\cos\theta\right] + \beta I_0 \exp\left[-Nd/\lambda\cos\theta\right]$$

$$= \alpha I_0 \frac{1-\exp\left[-Nd/\lambda\cos\theta\right]}{1-\exp\left[-d/\lambda\cos\theta\right]} + \beta I_0 \exp\left[-Nd/\lambda\cos\theta\right] \qquad (1)$$

Here, N is the number of mica layers, α and β are the proportional constants meaning the emission rate of Auger electrons summed from individual elements in one layer per unit of the primary electron beam incident on the analyzing region (α = 0 for the Au peak and the Ir peak, and β = 0 except for the Si and O peaks on the SiO2/Si substrate, the Au peak on the Au/Si substrate, and the Ir peak on the Ir/Si substrate), d is the thickness of a mica nanosheet (= 1 nm), and θ is the angle of Auger electron emission with respect to the sample normal toward the electron energy analyzer (= 42 ° for our case). It is notable that α in the first term of equation (1) represents the emission from the layer of mica nanosheet and β in the second term represents the emission from the substrate. By numerical fitting of equation 1 to the curves in **Fig 4.7**, the values of λ at individual AES peaks, i.e., at their kinetic energies, were evaluated as in Table I. Although the values of λ for O peak for the SiO2/Si substrate and the peaks with kinetic energy higher than that of Mg for the Au/Si and Ir/Si substrates were deviated from the values experimentally obtained by Garmash et al. for IMFP of Si oxide using the SAM [34], the other values were reasonably close to those values, as shown in **Fig 4.8**. The deviation might originate from the electron backscattering at the interface between the mica nanosheets and the substrates, including the electron diffraction effect through the single-crystal mica nanosheets. [32]

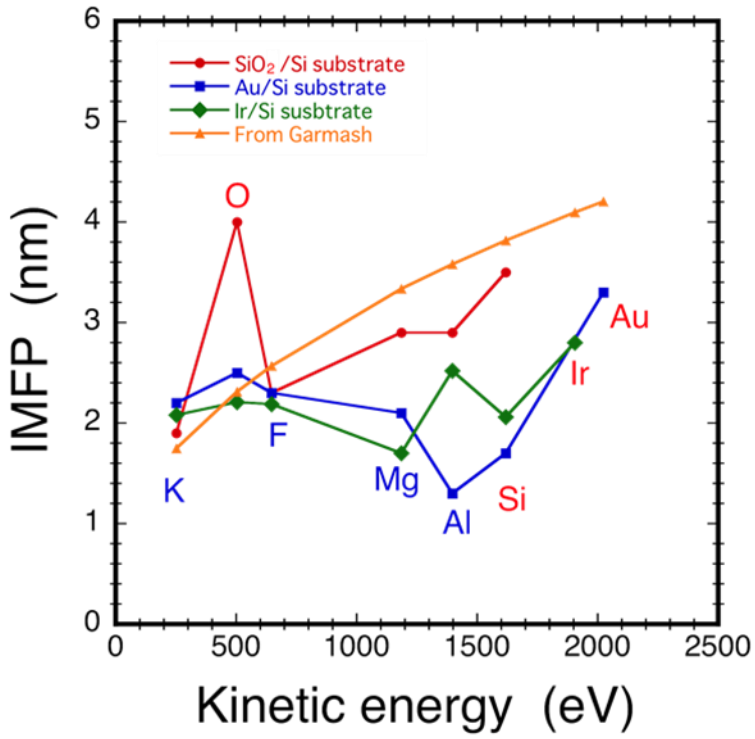

Figure 4. 6: Plots of the inelastic mean free path (IMFP, λ) evaluated from the change in the AES peak intensity for 1- to 20-layer-thick mica nanosheets on the SiO_2/Si, Au/Si, and Ir/Si substrates. The λ values at the kinetic energies of the individual AES peaks were in the range 1.3–4.0 nm. The orange points were calculated from the equation of IMFP, $\lambda = 0.1531 \times E^{0.4352} + 202.4 \times E^{-1.5}$ for SiO_2, where E is the kinetic energy, reported by (*V. I. Garmash, N. A. Djuzhev, E. P. Kirilenko, M. A. Makhiboroda, D. M. Migunov, J. Surf. Invest.: X-ray, Synchrotron and Neutron Tech. 2016, 10, 767)*. [30]

From the dependence of AES peak intensities on the thickness, we derive the calibration curves to evaluate the thickness. By taking the ratios of the AES peaks from the elements such as O, F and Mg that typically increase with thickness, with respect to the peaks such as Si and Au from the substrate that decrease with thickness (**Fig. 4.6**), the curves steeply increasing with thickness up to 5 – 6 layers can be produced as shown in **Fig. 4.8**. These curves can be used as the thickness calibration curve; unknown thickness of mica nanosheets at less than 6 layers can be evaluated from the ratio of AES peak of O, F and Mg with respect to that of elements of substrate in the AES spectrum by referring

the derived calibration curves which are universal for phlogopite nanosheets. We confirmed the validity of the calibration curves (**Fig. 4.8**) by randomly taking the AES spectra over seemingly thinner mica nanosheets, and afterward by measuring the thickness using the AFM.

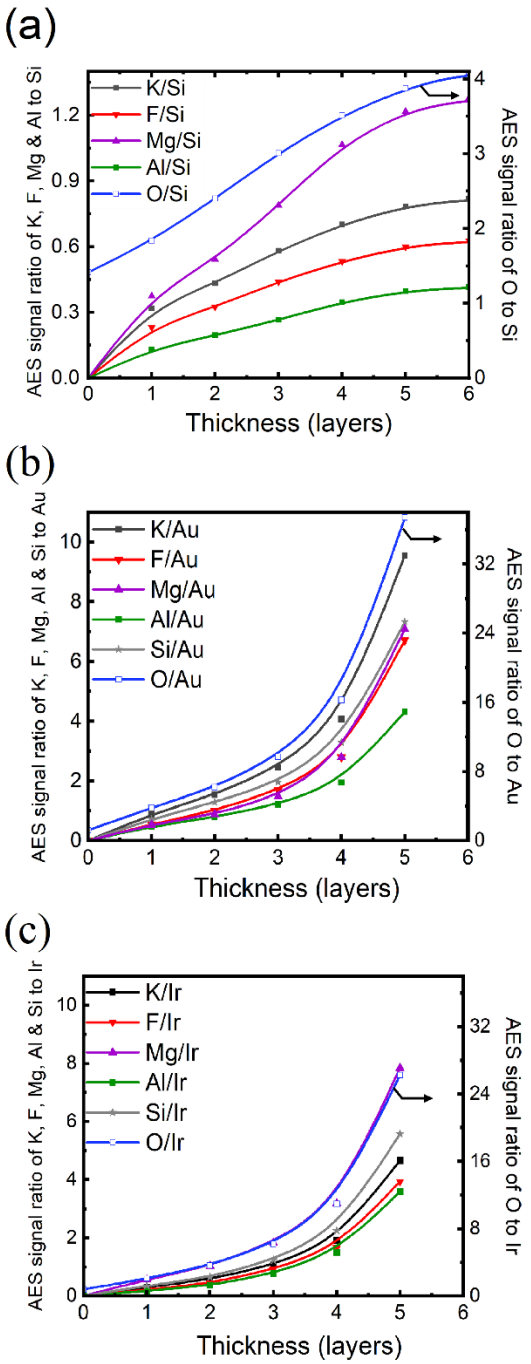

Figure 4. 7: Plots of the intensity ratios of the AES peaks with respect to (a) Si on the SiO_2/Si substrate, (b) Au on the Au/Si substrate, and (c) Ir on the Ir/Si substrate versus the thickness of the mica

nanosheet. The curves for Mg and O are useful as calibration curves to evaluate the thickness of the mica nanosheet. The curves connecting the points were drawn using cubic B-spline in the scientific graph software Origin. [30]

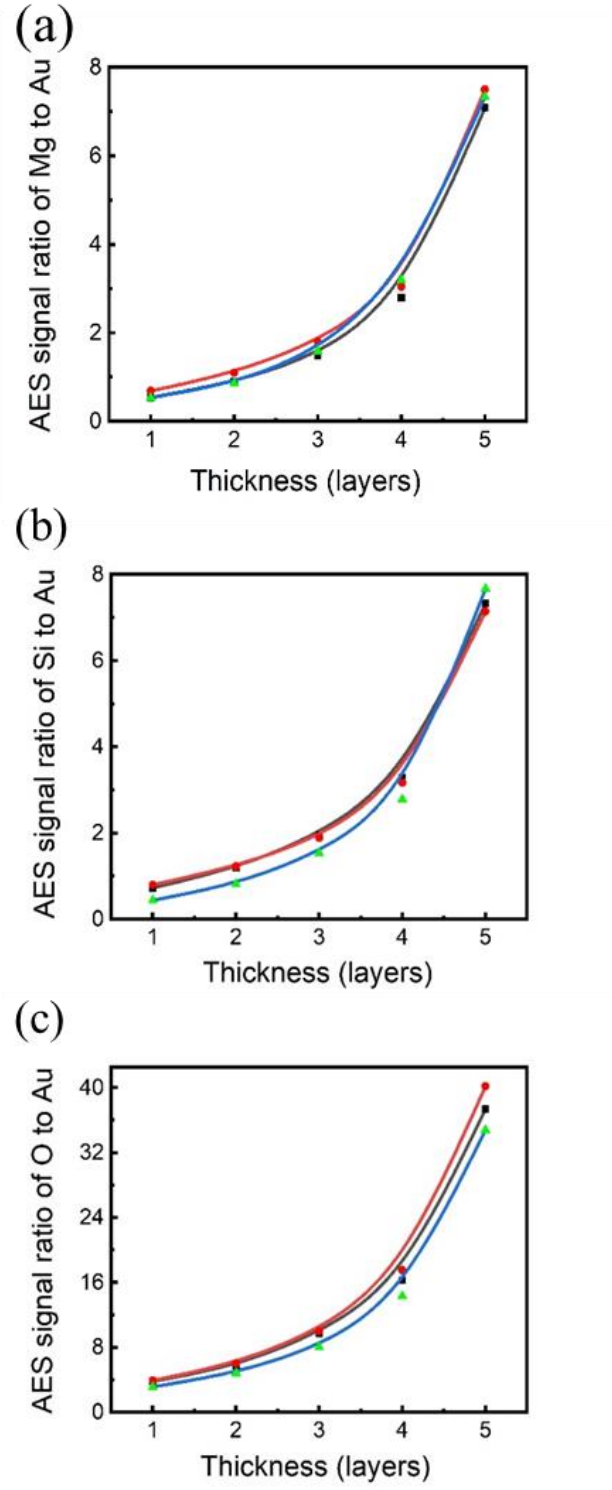

Figure 4. 8: AES peak-to-peak signal ratios of a) Mg to Au, b) Si to Au, and c) O to Au on the Au/Si substrate, which were randomly measured on the substrate covered with mica nanosheets with unknown thickness. The thicknesses of the mica nanosheets were subsequently measured by AFM. The ratios are plotted as a function of the measured number of layers of the mica nanosheets. The

ratios of Mg and O to Au show a reproducible relationship with the thickness because of the stronger AES signals of Mg and O. The plots in (a) and (c) seem to be suitable as calibration curves to evaluate the discrete thickness of the mica nanosheet, especially to distinguish between one and two layers. The curves connecting the points were drawn using cubic B-spline in the scientific graph software Origin. [30]

In order to measure the tunneling current through different layer of mica nanosheets, we carried out a separate set of experiment with the conductive atomic force microscopy (cAFM). A metal-insulator-metal tunnel diode has prepared with the cAFM tip coated with iridium as a top electrode and iridium coated silicon substrate as the lower electrode, in which electron from the first metal can tunnel into insulator (different layers of mica nanosheet) and be collected by the second metal. The *I–V* curves of mica nanosheets with thickness from one to five layers on the Ir-coated Si substrate are shown in **Fig. 4.9**, which were consecutively acquired by conductive AFM with Au/Si tip over-coated with Ir. Remarkably, the curves showed nonlinear behavior as the MIM contact [35], and the current values at a specified bias voltage decreased with increasing mica nanosheet thickness, probably because of the tunneling effect through the mica nanosheets. Although the metal electrodes of both sides of the nanosheet were Ir films, the curves exhibited asymmetric behavior with respect to the polarity of the applied bias voltage. This is possibly because of the difference in the geometries of the flat substrate and AFM tip shape and/or the state of the over-coated Ir on the tip.

When a voltage *V* is applied across a thin insulator with thickness *d* between two metallic electrodes, the tunnel current through the insulator layer *J* can be expressed as a function of *V* [34]:

$$J(V) = J_0\,[\left(\emptyset_0 - \frac{V}{2}\right)\exp\left(-C\sqrt{\emptyset_0 - \frac{V}{2}}\right) - \left(\emptyset_0 + \frac{V}{2}\right)\exp\left(-C\sqrt{\emptyset_0 + \frac{V}{2}}\right)]. \quad (2)$$

where $\boldsymbol{\emptyset_0}$ is the average barrier height of the insulator above the Fermi level, $\boldsymbol{J_0 = \frac{q^2}{2\pi hd}}$, and $\boldsymbol{C = \frac{4\pi d\sqrt{2m^* q}}{h}}$, where *q* is the electron charge, *h* is the Planck constant, and *m** is the effective mass of an electron in the insulator. We used Equation (2) to analyze the *I–V* curves, assuming that *m**= 0.32 *m*

(*m* is the electron mass) for SiO_2 in a thin film with the metal-oxide-semiconductor structure [36], because we could not find the value for mica. Because *C* includes the thickness *d*, the current in Equation (2) exponentially changes with the thickness.

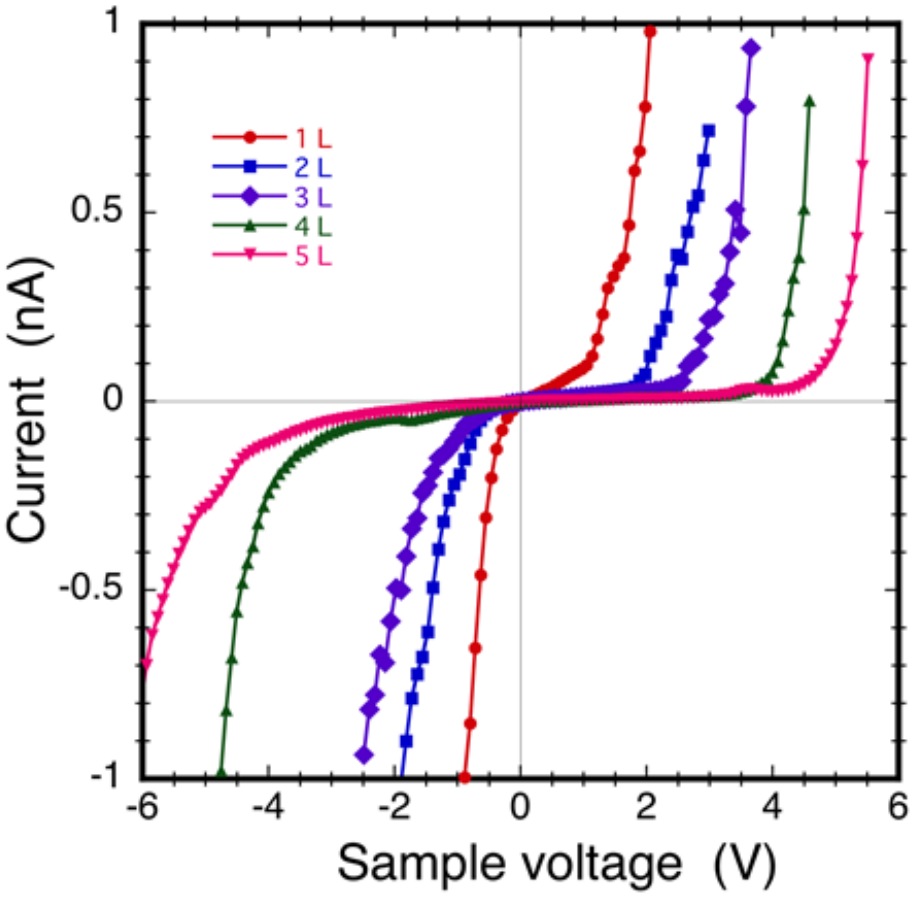

Figure 4. 9: (a) Current–voltage (*I–V*) curves of mica nanosheets with different thicknesses (one to five layers) on the Ir-coated Si substrate in the structure of an Ir–nanosheet–Ir contact measured by current AFM with an Au/Si tip over-coated with Ir. [30]

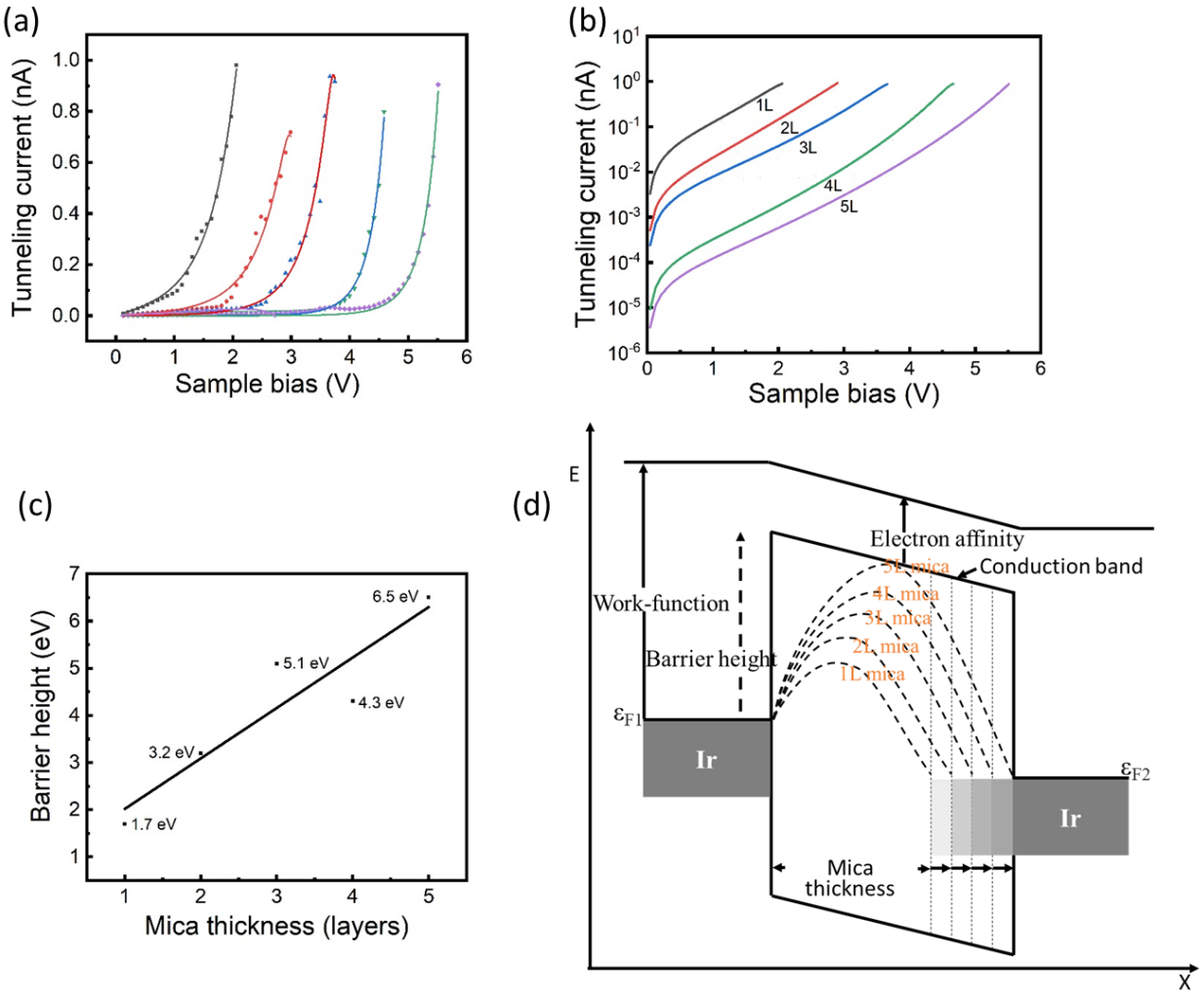

Figure 4. 10: (a) Forward current-voltage curve fitting to eq. 2, (b) Semilogarithmic plots corresponding to (a), (c) Barrier height as a function of mica thickness. (d) The energy band diagram of iridium-mica-iridium structure with 1 to 5 layers of mica nanosheets. The barrier height decreasing with the decreasing of mica nanosheets thickness.

By numerical fitting of Equation (2) to the *I–V* curves in **Fig. 4.9**, we determined the average tunneling barrier height $\emptyset_0$ to be about 1.7 eV for a one-layer mica nanosheet, and higher than about 6.5 eV for the thicker mica nanosheets **Fig. 4.10**. The $\emptyset_0$ value fluctuated, probably because of the contact pressure of the AFM tip or adventitious contamination on the mica nanosheets. The barrier height in the Ir-mica–Ir structure appeared to depend on the mica thickness. We have found that the barrier height decreased with decreasing thickness of the mica nanosheets. Although our experimental

data indicate a linear relationship between the barrier height and mica thickness, a direct correlation between them is very difficult. The dielectric constant of the insulator is important parameter to the barrier height at the interface. The dielectric constant of mica nanosheets is decreasing with the decreasing thickness down to one layer. In the MIM structure, we have used one- to five-layer mica nanosheets, as the dielectric constant of the mica nanosheets is changing with thickness that may affect the changing behavior of barrier height for different layer of mica nanosheets. In another case, the image-force lowering due to the two metals causes the metal-insulator barrier height to decrease as the insulator thickness decreases. Some important electrical properties of the dielectric (mica) films including the trap spacing, the trap density, the electronic drift mobility, and the dielectric relaxation time, the density of states in the conduction band is responsible in the changing behavior of barrier height. To reveal the exact mechanism, further investigation is necessary, in particular, by fabricating the MIM device structure on the mica nanosheet to avoid the variation of the contact pressure and the adventitious contamination on the surface.

4.4 Conclusion

We have demonstrated quantitative thickness determination of few-layers mica nanosheets by using Auger electron spectroscopy from peak to peak Auger electron intensity. The Auger spectra have shown distinct characteristic shape and intensity according to the change of the number of layers of mica sheets. It has been shown that AES system can be standardized and in the range of 1 to 5 layers of mica film thickness can be measured by simply determining the Auger electron peak to peak intensity and which is best coincide with the AFM thickness measurement. Here we also constructed calibration curves to evaluate the discrete thickness of mica nanosheets based on the change in the AES peaks and the validity was verified by the equation based on the IMFP values. The *I–V* measurements of metal–nanosheet–metal contacts showed the potential of mica nanosheets of pure artificially synthesized phlogopite with discrete thickness for electron tunneling devices. The primary

utility of the AES thickness measurement lies in the fact that the measurement is quite generally applicable, non-destructive and independent with substrate.

References

1. Khan, Ali Hossain, et al. "Two-dimensional (2D) nanomaterials towards electrochemical nanoarchitectonics in energy-related applications." Bulletin of the Chemical Society of Japan 90.6 (2017): 627-648.
2. Bhimanapati, Ganesh R., et al. "Recent advances in two-dimensional materials beyond graphene." ACS nano 9.12 (2015): 11509-11539.
3. Lin, Zhong, et al. "Research Update: Recent progress on 2D materials beyond graphene: From ripples, defects, intercalation, and valley dynamics to straintronics and power dissipation." APL Materials 6.8 (2018): 080701-080709.
4. Xu, Mingsheng, et al. "Graphene-like two-dimensional materials." Chemical reviews 113.5 (2013): 3766-3798.
5. Novoselov, Kostya S., et al. "Two-dimensional gas of massless Dirac fermions in graphene." nature 438.7065 (2005): 197-200.
6. Wilmart, Quentin. Engineering doping profile in graphene: from Dirac fermion optics to high frequency electronics. Diss. (2015).
7. Pacile, D., et al. "The two-dimensional phase of boron nitride: Few-atomic-layer sheets and suspended membranes." Applied Physics Letters 92.13 (2008): 133107-133112.
8. Dean, Cory R., et al. "Boron nitride substrates for high-quality graphene electronics." Nature nanotechnology 5.10 (2010): 722-726.
9. Wang, Qing Hua, et al. "Electronics and optoelectronics of two-dimensional transition metal dichalcogenides." Nature nanotechnology 7.11 (2012): 699-705.

10. Jariwala, Deep, et al. "Emerging device applications for semiconducting two-dimensional transition metal dichalcogenides." ACS nano 8.2 (2014): 1102-1120.
11. Zhao, Yang, et al. "Recent developments and understanding of novel mixed transition-metal oxides as anodes in lithium ion batteries." Advanced Energy Materials 6.8 (2016): 1502175-150182.
12. Kalantar-zadeh, Kourosh, et al. "Two dimensional and layered transition metal oxides." Applied Materials Today 5 (2016): 73-89.
13. Maslova, M. V., L. G. Gerasimova, and Willis Forsling. "Surface properties of cleaved mica." Colloid Journal 66.3 (2004): 322-328.
14. Castellanos-Gomez, Andres, et al. "Atomically thin mica flakes and their application as ultrathin insulating substrates for graphene." Small 7.17 (2011): 2491-2497.
15. Low, Chong Guan, et al. "Graphene field effect transistors with mica as gate dielectric layers." Small 10.20 (2014): 4213-4218.
16. Bitla, Yugandhar, and Ying-Hao Chu. "MICAtronics: A new platform for flexible X-tronics." FlatChem 3 (2017): 26-42.
17. Rudenko, A. N., et al. "Graphene adhesion on mica: Role of surface morphology." Physical Review B 83.4 (2011): 045409-045414.
18. Low, Chong Guan, and Qing Zhang. "Ultra-thin and Flat Mica as Gate Dielectric Layers." Small 8.14 (2012): 2178-2183.
19. Li, Hai, et al. "Rapid and reliable thickness identification of two-dimensional nanosheets using optical microscopy." ACS nano 7.11 (2013): 10344-10353.
20. Gaskell, P. E., et al. "Counting graphene layers on glass via optical reflection microscopy." Applied physics letters 94.14 (2009): 143101-143107.
21. Shearer, Cameron J., et al. "Accurate thickness measurement of graphene." Nanotechnology 27.12 (2016): 125704-125709.

22. Nemes-Incze, P., et al. "Anomalies in thickness measurements of graphene and few layer graphite crystals by tapping mode atomic force microscopy." Carbon 46.11 (2008): 1435-1442.
23. Shimizu, Ryuichi. "Quantitative analysis by Auger electron spectroscopy." Japanese journal of applied physics 22.11R (1983): 1631-1638.
24. Seah, M. P. "Quantitative Auger electron spectroscopy and electron ranges." Surface Science 32.3 (1972): 703-728.
25. Holloway, P. H. "Thickness determination of ultrathin films by Auger electron spectroscopy." Journal of Vacuum Science and Technology 12.6 (1975): 1418-1422.
26. Xu, Mingsheng, et al. "Auger electron spectroscopy: a rational method for determining thickness of graphene films." ACS Nano 4.5 (2010): 2937-2945.
27. Sutter, P., and E. Sutter. "Thickness determination of few-layer hexagonal boron nitride films by scanning electron microscopy and Auger electron spectroscopy." APL Materials 2.9 (2014): 092502-092508.
28. Mathieu, H. J., M. Datta, and D. Landolt. "Thickness of natural oxide films determined by AES and XPS with/without sputtering." Journal of Vacuum Science & Technology A: Vacuum, Surfaces, and Films 3.2 (1985): 331-335.
29. Cole, D. A., et al. "SiO_2 thickness determination by x-ray photoelectron spectroscopy, Auger electron spectroscopy, secondary ion mass spectrometry, Rutherford backscattering, transmission electron microscopy, and ellipsometry." Journal of Vacuum Science & Technology B: Microelectronics and Nanometer Structures Processing, Measurement, and Phenomena 18.1 (2000): 440-444.
30. Razzakul, Islam Mohammad, and Masahiko Tomitori. "Evaluation of the discrete thickness of exfoliated artificially synthesized mica nanosheets on silicon substrates: Toward characterization of the tunneling current through the nanosheets." Applied Surface Science 532 (2020): 147388-147401.

31. Bhattacharyya, Krishna G. "XPS study of mica surfaces." Journal of Electron Spectroscopy and Related Phenomena 63.3 (1993): 289-306.
32. Tarng, M. L., and G. K. Wehner. "Escape length of Auger electrons." Journal of Applied Physics 44.4 (1973): 1534-1540.
33. Seah, M. Pl, and W. A. Dench. "Quantitative electron spectroscopy of surfaces: A standard data base for electron inelastic mean free paths in solids." Surface and interface analysis 1.1 (1979): 2-11.
34. Garmash, V. I., et al. "Experimental determination of the energy dependence of electron inelastic mean free path in silicon oxide and silicon nitride." Journal of Surface Investigation. X-ray, Synchrotron and Neutron Techniques 10.4 (2016): 767-770.
35. Sze, S. "Physics of semiconductor devices Wiley Eastern." New York (1981).
36. Toumi, S., et al. "Determination of Fowler–Nordheim tunneling parameters in Metal–Oxide–Semiconductor structure including oxide field correction using a vertical optimization method." Solid-State Electronics 122 (2016): 56-63.

Chapter 5

Mica Nanosheet Patterned Etching Using Focused Electron Beams

Among the layered materials, mica is a well-known phyllosilicate mineral have a wide bandgap with unique optoelectronic properties that have remarkable impact on flexible electronics. However, the applicability and wide deployment of mica nanosheets in scalable devices is presently limited by a lack of suitable nanoscale processing techniques, particularly growth and etching. Here we present a Focused electron-beam (FEB)-induced etching of mica nanosheets in Auger electron spectroscopy (AES) studies as a selective nanoscale etching technique. We have shown that the electron-beam techniques can selectively remove mica layers and induce chemical reactions, as well as possible structural transformations. The primary electron beam bombarding on mica surface has a profound influence on its composition, the beam dissociates the surface compound into elementals component and the exposed surface element is then removed from the surface. The effects of beam current, beam energy, and scan time are investigated as controlling parameter to the dissociations on the mica nanosheets. The technique enables damage-free, nano scale, iterative patterning of mica nanosheets, which can widen the fabrication of mica-based 2D heterostructures and devices. This works provides an idea on how to optimize the experimental conditions for mica characterizations with energetic electrons and device fabrication.

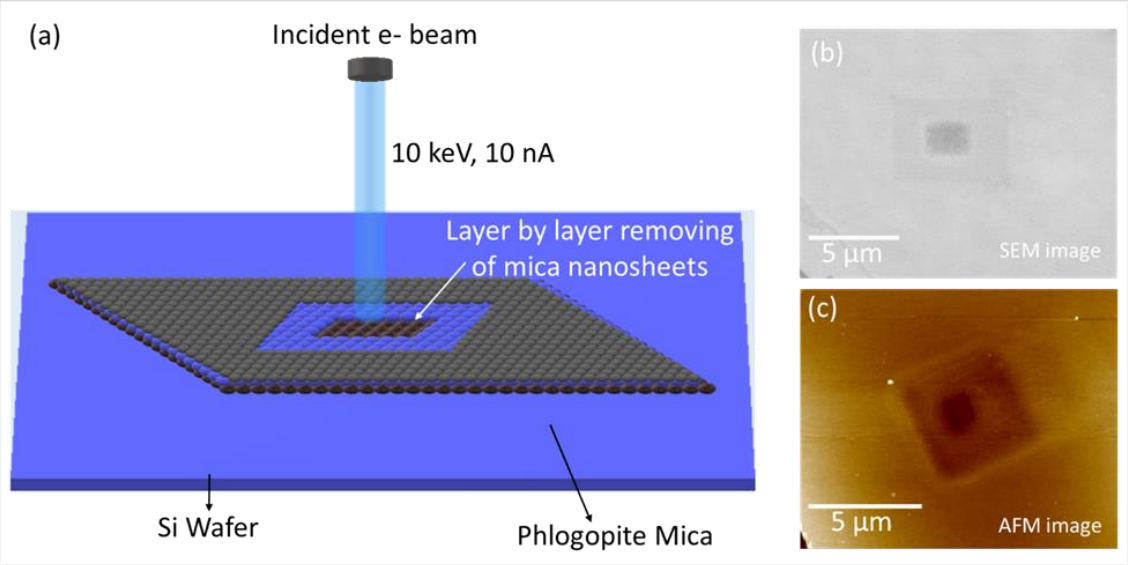

Figure 5: Schematic illustration of electron beam induced etching of Layer by layers removing of mica sheets under the focused election beam.

5.1 Introduction

Mica is a group of single-crystalline phyllosilicate minerals, cleavable to nanometer thicknesses, with a wide range of applications [1-3]. The properties of mica are remarkable in regard to electric insulating, chemical inertness, and mechanical and thermal strength. Furthermore, the thinned mica sheets are optically transparent and flexible, which are beneficial to substrates for electronic devices [4–6]. The applicability of 2D mica nanosheets in the devices, however, has not been sufficiently widened by a lack of suitable techniques for fine-pattern fabrication processes. While high-temperature annealing [7,8], oxidative etching [9], and reactive ion etching [10] are the common processing techniques for 2D materials, those techniques do not allow fine-pattern fabrications of the mica nanosheets. Direct-write patterning using a focused electron beam (FEB) and ion beam (FIB) also offers high-resolution methods to finely fabricate 2D materials [11–14]. However, the damage induced by high-energy ion beam bombardment is problematic [15]. Instead, the FEB seems suitable for low-damage or damage-free direct-write processes to selectively remove mica layers. For example, a variety of materials are fabricated on the scale of a sub-micrometer or few-tens nanometer by FEB

such as focused electron-beam-induced deposition (EBID) of silicon dioxide [12,13], carbon nanowires [14], platinum interconnects [15], as well as FEB etching of silicon [16] and AlGaAs [17]. Some compounds as oxides are decomposed by the electron beam irradiation to be volatile compositions, which would be evaporated from their surfaces. It is reported that the thin silicon dioxides were removed by electron beam irradiation [28].

In the present study, we locally etched the mica nanosheets by using FEB of a scanning Auger electron microscopy/spectroscopy (SAM) setup, and in-situ evaluated the etched areas by Auger electron spectroscopy (AES) in the SAM setup, as well as ex-situ atomic force microscopy (AFM). The AES is a powerful surface analytical technique to examine the chemical components on the surfaces [18-21] [22-25]. The target material is the artificially synthesized pure phlogopite of the mica group [2,3]. The prolonged FEB irradiation on the freshly cleaved mica surface could decompose the mica surfaces, resulted in etching patterns on them. We investigated the effects of beam current, beam energy, and irradiation time as of controlling parameters for the mica nanosheet patterned etching.

5.2 Methods and Material

A single crystal of artificially synthesized pure phlogopite with dimensions of 10 mm × 10 mm × 0.5 mm was purchased from Itoh Kikoh Co., Ltd (Tokai, Japan). The mica nanosheets were prepared by mechanically exfoliation of the phlogopite and affixed onto a Si substrate covered with a native oxide using a clean polyurethane hand roller: details of the exfoliation process are discussed in chapter 3. The Si substrate cut from a Si(111) wafer was cleaned in an ultrasonic bath with acetone and Mill-Q water followed by drying with pure nitrogen gas flow. Subsequently, ozone cleaning was carried out to remove hydrocarbon contaminants. After affixing the mica nanosheets on the Si substrate, the Si substrate was set on a custom-made sample holder, being resistively heated at 550 °C for 30 min in a

vacuum chamber of the low of $l0^{-8}$ Torr by passing a DC current to remove water adsorbed and contaminations from the sample; the chamber was connected to the main chamber of SAM through a gate valve. The sample temperature was measured with an infrared thermometer (IR-CAS, CHINO Corp., Tokyo, Japan) through a glass viewport. The outline of the exfoliation and affixing processes is illustrated in **Fig. 3.1**.

The Focused electron beam etching of mica nanosheets was performed with an electron beam in a SAM setup (SAM670, ULVAC-PHI, Inc., Chigasaki, Japan) with a cylindrical mirror analyzer for electron spectroscopy, while scanning electron microscopy (SEM) images were observed using the function of the SAM setup. The vacuum of the SAM chamber was of the order of $l0^{-10}$ Torr. In the SAM setup, the AES analysis and SEM observation were carried out with the same FEB, while the FEB irradiation time was prolonged for the etching experiments. The electron beam energies ranged from 3 keV to 20 keV with a current from 1 nA to 20 nA. The AES spectra were obtained in the detection of electron counting with an energy sweep with a 0.5 eV/step for 20 ms/step and averaged over multiple sweep cycles. Using the software of the SAM, the AES spectra were displayed in the differential form through numerical calculation with the parameters of 21-point differentiation and smoothing from the spectra data, which were collected by the electron counting method. After the etching in the SAM chamber, the etched areas were characterized with an atomic force microscopy (AFM) setup (SPM 5500, Agilent Technologies, Inc., Santa Clara, CA, USA) operated in contact mode in air.

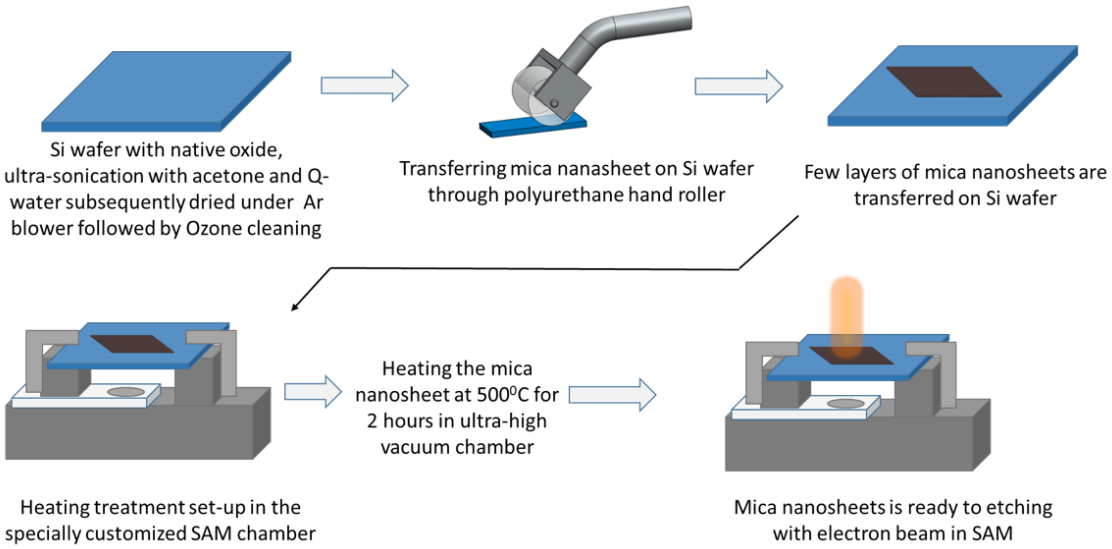

Figure 5. 1: Schematics of preparing mica nanosheets on the Si substrate for focused electron beam etching experiments.

5.3 Results and discussion

Figure 5.2 shows a typical SEM image of the mica nanosheets of a thickness of 15 nm with an area of 5x6 μm^2, (a) before and (b) after etched by using a 10-keV FEB with an electron beam current of 10 nA for 200 and 100 minutes. The SEM image clearly showed an electron beam radiation effect on the mica surface by completely (area I) and partially (area II) removed mica layers.

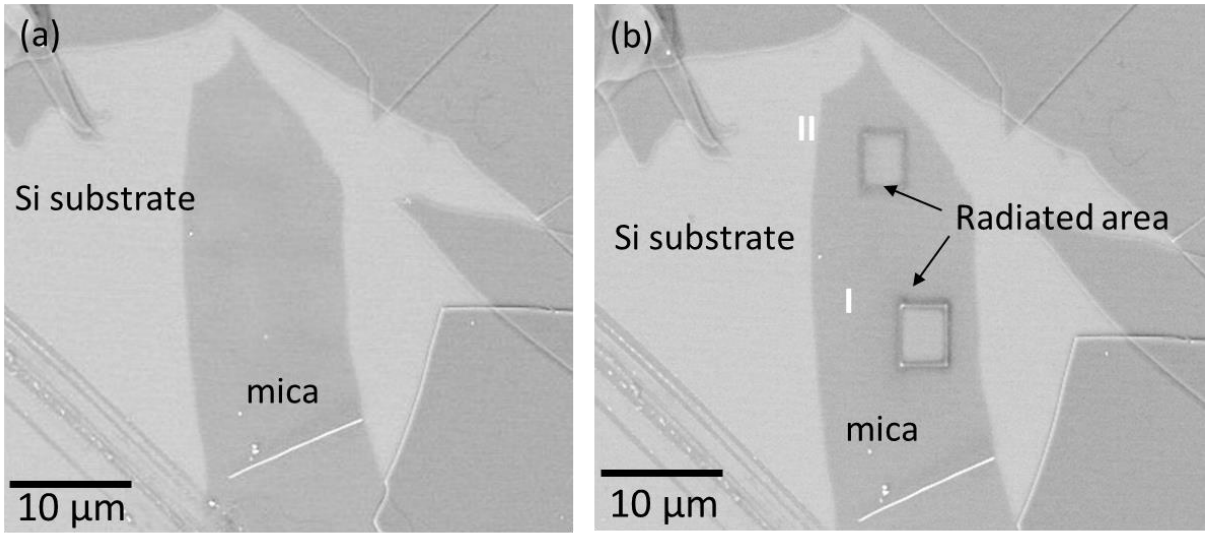

Figure 5. 2: SEM image (a) before and (b) after selectively removing 15 nm thick mica layer by FEB of 10 keV and 10 nA. Areas I and II are irradiated in the same scan size but for different irradiation time of 200 min and 100 min, respectively

Figure 5.3 (a) shows the SEM image of the mica nanosheet with a thickness of 8 nm before and after the FEB irradiation at 10 keV and 10 nA for 90, 120, 150, and 180 min in the area of II to V correspond to the irradiation times respectively. First the area II (10×8 μm^2) is radiated for 90 minutes then the area III (8×6 μm^2) is radiated for 30 minutes, then selecting area IV (6×4 μm^2) inside of II and III and radiated for 30 minutes subsequently choosing area V (4×2 μm^2) and radiated for another 30 minutes. **Figure 5.3** (c) shows the AES spectra taken from the five areas in **Fig. 5.3** (a). The AES peaks of K, F, Al, Mg, and Si were plainly observed in the area of I to VI but not in area V, area V is unfilled by phlogopite. We observed that the individual mica elementals peak intensities decreased from the area I to V as the irradiations time is continuously increasing in these areas. On the other hand, the strongest AES peak of Ir was found in area V and continuously decreases from V to II and no Ir peak was found in area I. This result suggesting that different irradiations time removing different layers of mica nanosheets.

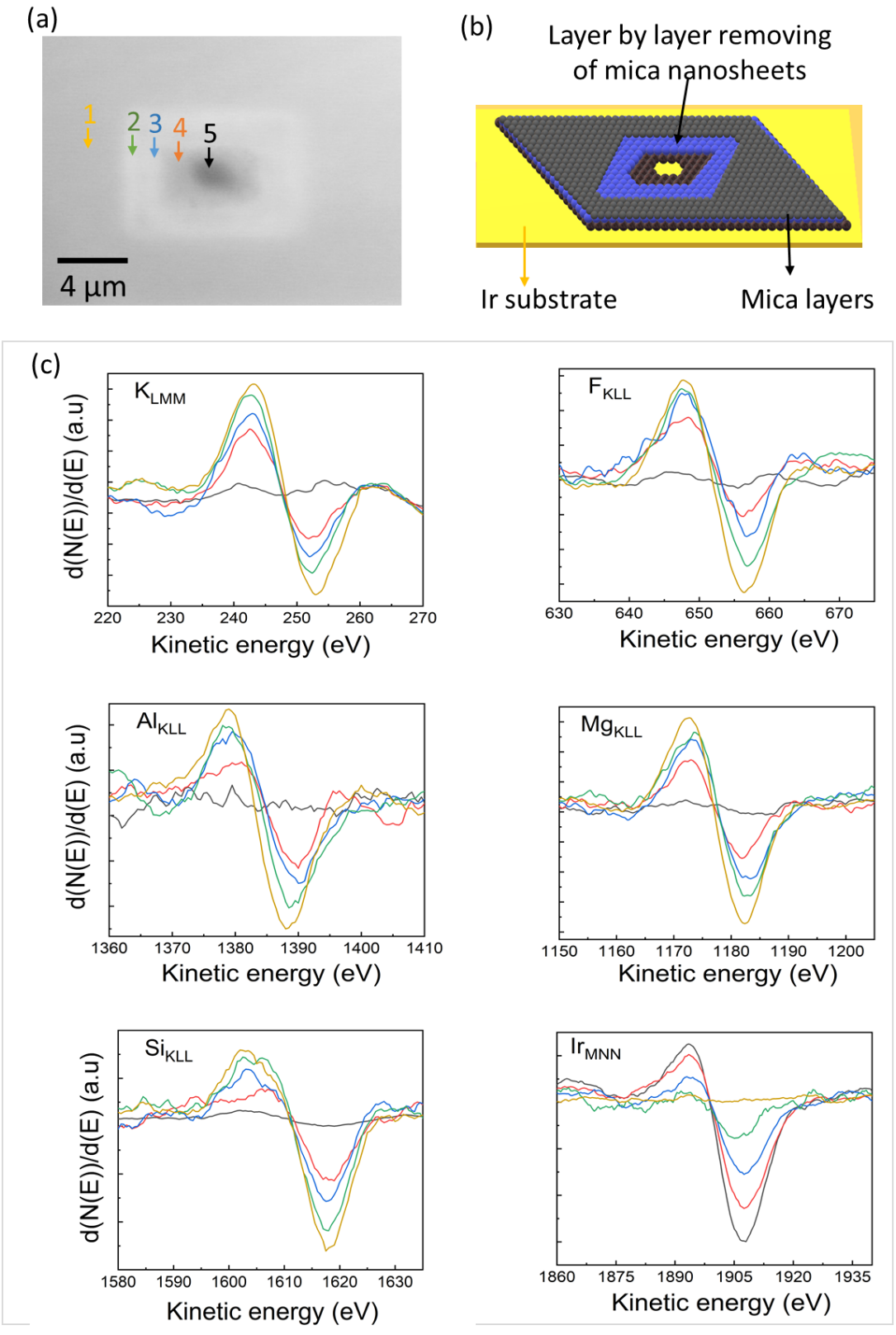

Figure 5. 3: (a) SEM image of a few layers mica after irradiated with the FEB for 90, 120, 150, and 180 min at the areas denoted by II to V, respectively. (c) AES spectra acquired at areas I to V. The

AES peaks intensity of K_{KMM}, F_{KLL}, Mg_{KLL}, Al_{KLL}, and Si_{KLL} decreases from I to V, and Ir_{MNN} increases vice versa. The electron beam energy and current were 10 keV and 10 nA, respectively.

Figure 5.4 (a) shows a typical AFM image of the mica nanosheet with a thickness of 6 nm; four regions labeled by I, II, III, and IV of an area of a ~4 µm × 5 µm were irradiated with the FEB at 10 keV and 10 nA for 50, 90, 160, and 220 min, respectively. The averaged beam fluences were calculated to be 1.5×10^{-12}, 2.7×10^{-12}, 4.8×10^{-12}, and 6.6×10^{-12} C/nm^2, respectively. The cross-sectional line profile (below **Fig. 4.4**(a)) shows the etched depths of one-, two-, four-, and six-layer mica (one-layer thickness is 1 nm), respectively. The etched depths were examined as a function of the irradiation time; as shown in **Fig. 5.4**(b), the plots exhibited an exponential behavior.

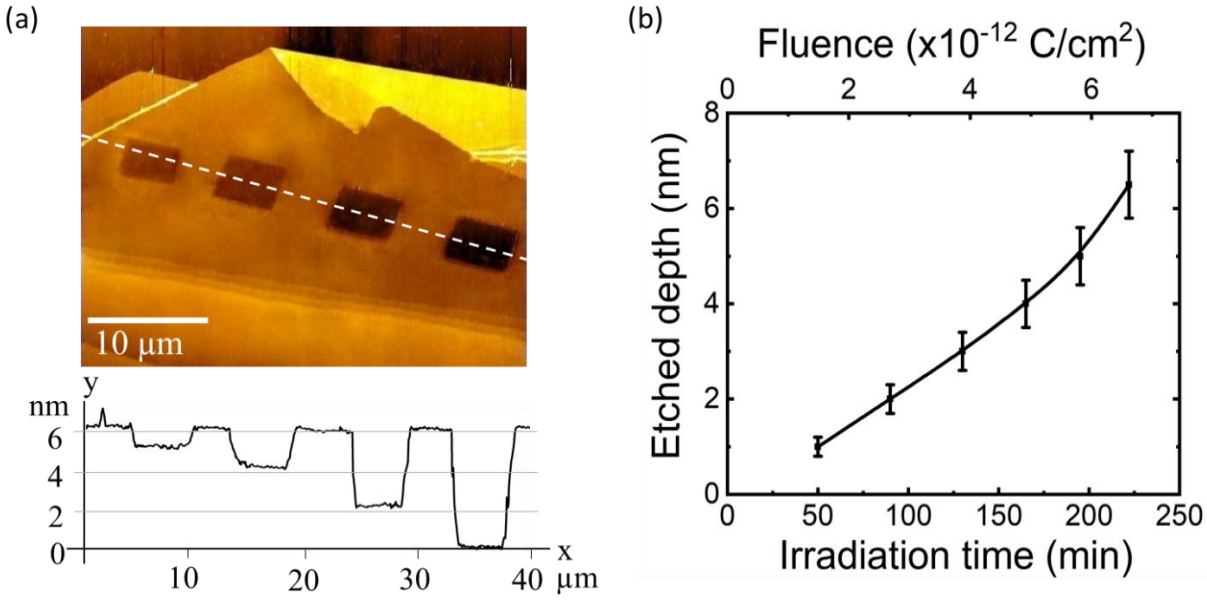

Figure 5. 4: (a) AFM image of the 6 nm-thick mica nanosheet irradiated with the FEB at 10 keV and 10 nA, scanned over the areas of ~4×5 µm^2. The irradiation times for region I, II, III, and IV were 50, 90, 160, and 220 min, respectively, resulted in removal of one, two, four, and six mica layers, measured from the cross-sectional line profile of the AFM image. (b) Plots of etched depths as a function of the FEB irradiation time as well as the beam fluence using the same beam and scan conditions in (a). [26]

Having demonstrated the ability to etch monolayers of mica nanosheets with an area scanning mode, we now characterize the etch process by point analysis mode. **Figure 5.5**(a,b) shows SEM image and plots of etch pit depth versus time respectively, revealing that the hole generated by the incident electron beam is increasing as the time of radiations is advancing. The fact that the etch rate is increasing with time indicates that the electron beam does create chemically active defects below the top monolayer of mica nanosheets. Etching depth dependencies on time have key insights into the underlying mechanisms. The most likely explanation in etch mechanisms is that the etching process is governed by the electron-induced decomposition of mica compound into elemental components. This phenomenon, known as the electron-stimulated desorption (ESD), in this process the chemical species from the radiated sample are ejected employing an electron-induced excitation process. Madey and Yates represented the basic mechanisms associated with ESD in which the incident electron current is directly proportional to the ion current generated via ESD [27]. Another interesting observation regarding **Fig. 5.5** (c) is the existence of a mildly etched ring surrounding the major etch feature in the points analysis mode. This peripheral etching can be considered as the effect of an etching by backscattered electrons (BSE) or secondary electrons (SE) emerging from the surface. We have observed that, regardless of the shape of the feature etched, the peripheral damaged region is always circular outside the primary electron beam radius. For example, if the beam is scanned in a smaller size square pattern, there is still a circular ring of etching around the irradiated region. The delocalized damage in areas beyond the e-beam irradiated regions is attributed to incomplete etching caused by backscattered electrons (or secondary electrons [28]) that are emitted from the sample after several scattering events. That kind of peripheral was damaged also observed in other materials such as SiO_2 [29] and h-BN [30] when treating with a focus electron beam. The effect of the BSE can be overcome simply by using a low energy electron beam, e.g., 1 keV [31].

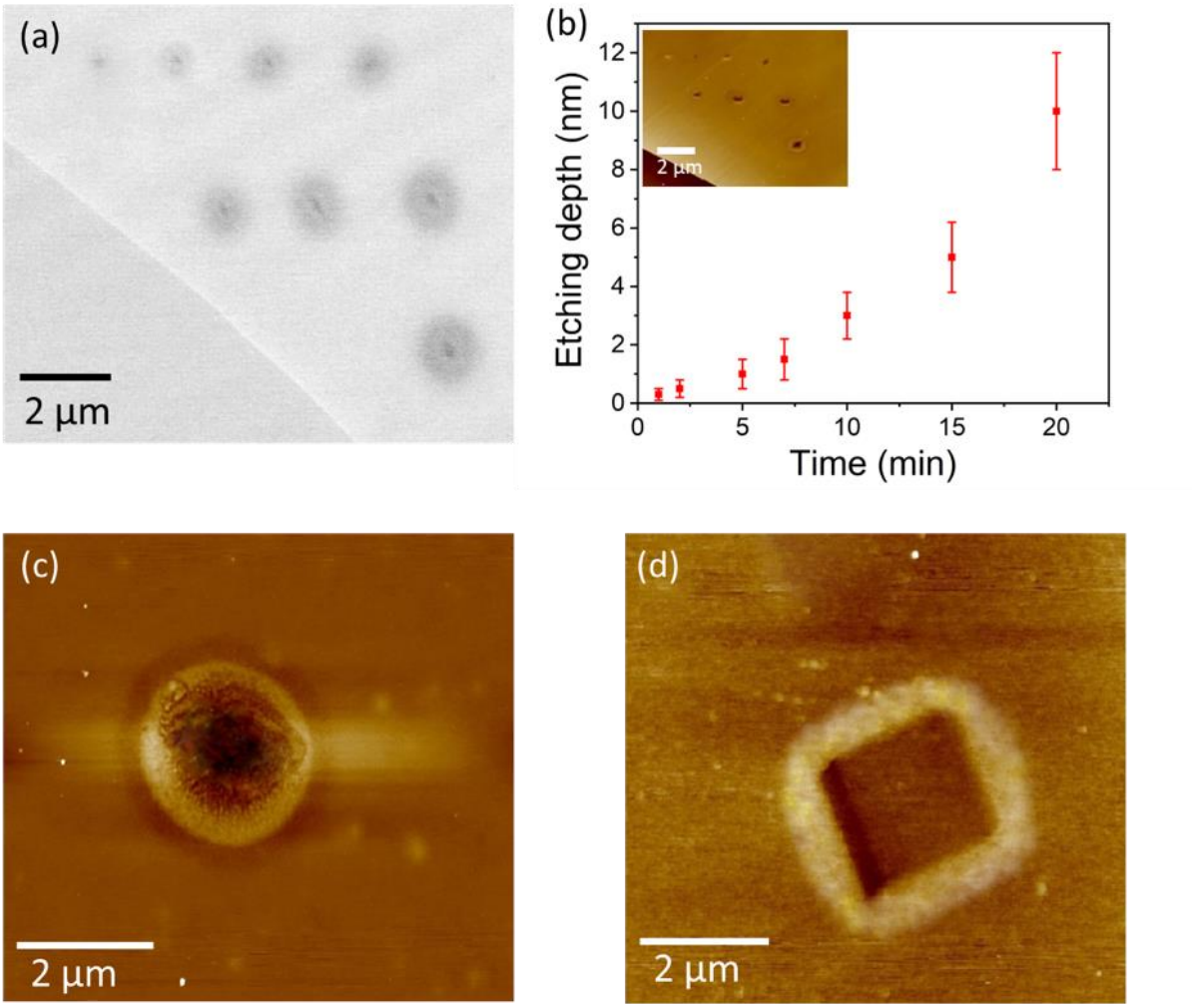

Figure 5. 5: (a) SEM image of point mode analysis with a beam energy of 10 keV and 10 nA current. (b) Plots depicting the effect of radiations on mica as a function of etching time, the inset is an AFM image of the same area of SEM image used to make the plot. The etching depth increases in a nonlinear manner as the time of radiation is increased. (c) AFM image of 20 minutes radiations effect on mica with Points mode analysis, the image depicted the peripheral etching that may occur with electron beam etching. The micrograph (d) shows that even when the scanned region is a square (3x3 μm^2) radiated for 150 minutes, the resulting peripheral damage remains circular.

We have performed the experimental studies examining the effects of incident beam energy and current on the mica surface. The effect of different incident beam energy varied from 3 keV to 20

keV on mica nanosheets was performed using point scan mode analysis at 8000 times magnification at the incident current of 10 nA, the etch time was 10 min. The results are displayed in **Fig. 5.6**, indicating that the observed etching depth (the etching depth profile collected with AFM analysis at contact mode in the air) is decreased approximately linearly with increasing beam energy (**Fig. 5.6** (b)). This experiment was carried out at constant current but as the beam energy is changing the current density changes proportionally utilizing a change in spot size. Whereas we don't know the specific probe size in our experimental setup, it can be observed from the SEM image that the spot diameter typically decreases with increased beam energy, therefore, it is expected that the current density is higher for high beam energies.

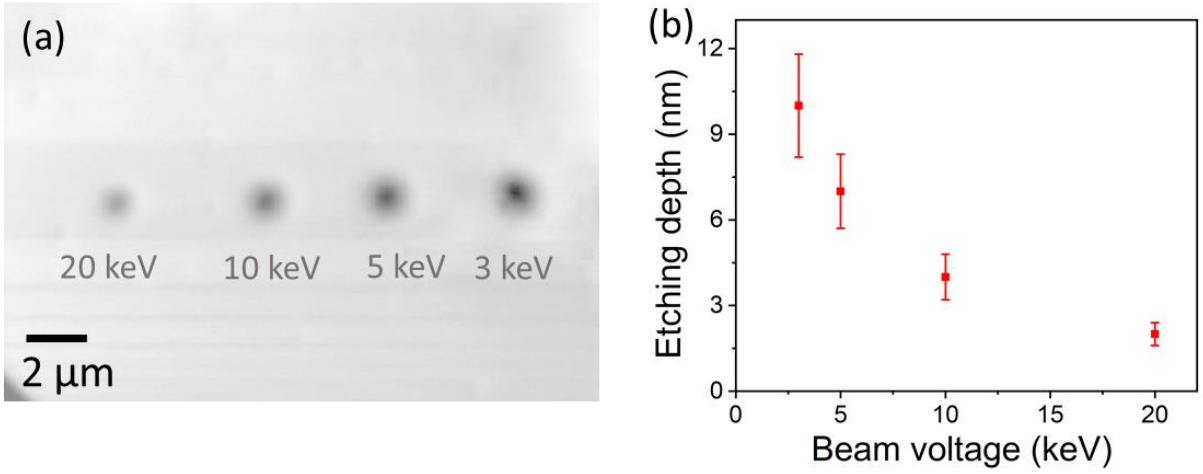

Figure 5. 6: (a) SEM image and (b) Plot depicting the effects of different beam energy on the mica etching process. This experiment was carried out with a point scanning mode at a constant beam current of 10 nA and radiation exposer time is 10 min. Both figures clearly showing that increased energy results in a decrease in the etching depth. Etching depth was measured with AFM measurement at contact mode in air. [26]

The incident beam current has a strong correlation to the reduction of mica layers, therefore, the effects of beam current on the etching process were also investigated and results are displayed in **Fig. 5.7**(a,b). The conditions of the experiments were as follows: 12 keV beam energy, variable current,

a magnification of 8000 times, and etching time of 10 min with a point mode analysis. From **Fig. 5.7**, it is evident that the etching depth is increasing with increasing current, typically the spot diameter increases as the beam current is increased, resulting in a change in current density.

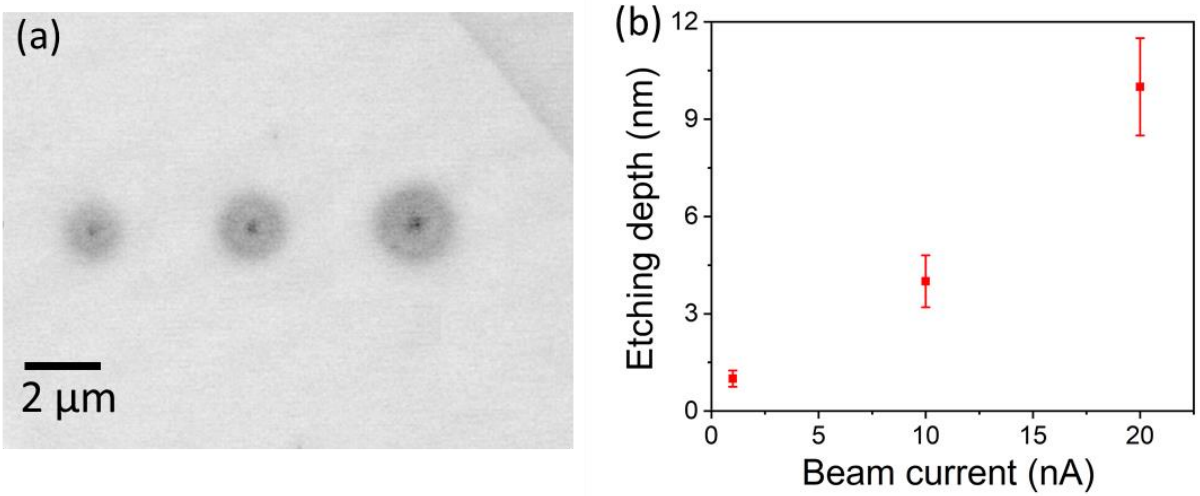

Figure 5. 7: (a) SEM image and (b) Plots of etching depth as a function incident beam current. Experiments were performed in point mode analysis with a beam energy of 10 keV. The etching depth increases linearly as the beam current is increased. Etching depth was measured with AFM measurement at contact mode in air. [26]

The primary electron beam bombarding on the mica surface has a significant effect on the surface composition. The layered mica structural unit (1 nm) comprises two tetrahedral sheets on either side of an octahedral sheet and these (2:1) layer stacks are bound together by interlayer cations (**Fig. 1.2**). The basic building blocks of the mica layers are silicate tetrahedron (SiO_4) and magnesium octahedron (MgO_6). Si ions in the tetrahedral sheets are partially substituted by Al ions (1/3) to give a net negative charge and interlayer cations (K^+) maintaining the charge neutrality of the unit. We are considering that the incident electron beam can break up the mica compound into elemental components and removed from the surface at the time of radiations occurring. To discuss the effect of electron irradiation on the mica surface, the Auger spectrum of $Si(-O-)_4$ from the mica surface will

be presented here. During the radiation, silicate tetrahedron $Si(-O-)_4$ is broke up into Si and O component and we can easily distinguish the two species present on the surface by analyzing similarities/differences in the features of the Auger spectra from Si and $Si(-O-)_4$. Silicon with native oxide is perhaps the most extensively studied element in the periodic table using AES, and lots of original work presenting the fundamental mechanisms of the reduction of SiO_x by electron radiation during Auger analysis [32–35]. There are two Auger spectra of Si, one is the low-energy Auger peaks originating from the LVV -type transitions and another one is a group of high-energy Auger peaks having its origin in the KLL-type transitions. These high-energy peaks are of great importance for the practical use in surface elemental analysis in the unambiguous identification of Si comparing the overlap problem in the low-energy Auger spectrum. For the study of mica dissociations by electron beam bombardment, we have investigating the low-energy side of $Si(-O-)_4$/Si Auger peak. In the low energy spectrum, the Auger peak appear at 78 eV is usually monitored for the purposes of identification of $Si(-O-)_4$ tetrahedron, whereas the 92-eV peak is characterized for the elemental Si [36]. In the early stage of mica dissociations, the tetrahedron $Si(-O-)_4$ 78 eV peaks are prominent, with continuous electron bombardment on the mica surface, a new peak appears on the high-energy side of the $Si(-O-)_4$ at 78 eV peak [**Fig. 5.8**], this new peak at 92-eV is characteristic of elemental Si. In order to measure the peak height variation with the time of electron beam incident, the 78 eV and 92 eV Auger peaks are continuously monitored. **Figure 5.8** shows typical change in AES spectra due to the exposer to an electron beam, the peak to peak intensities are shifted toward the higher-energy side which is correspond to the Si-92 eV. As the time passes and Si Auger peak intensities gradually increasing therefore we are expecting that the mica compound broke up into its elemental form. The appearance of new and strong Auger peak at 91 eV and reduction of highly oxidized Si upon extended-time irradiation with 10 keV primary electron beam with 10 nA beam current has permitted us to declare the radiation damage effects on mica surface.

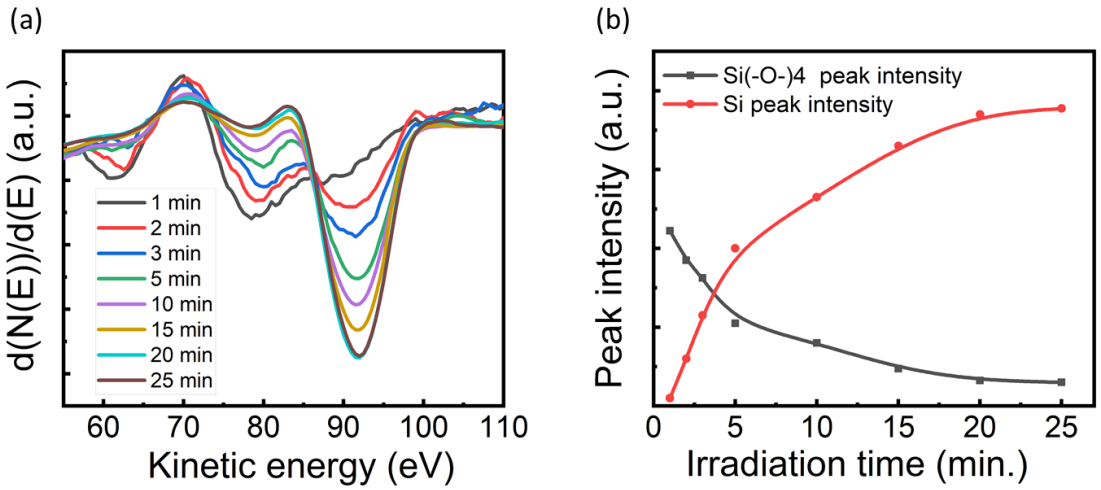

Figure 5. 8: (a) AES spectra around the peaks of $Si(-O-)_4$ at 78 eV and Si at 92 eV, intermittently taken with increasing irradiation time to be 1, 2, 3, 5, 10, 15, and 20 min in the point mode of the FEB at 10 keV and 10 nA. (b) AES peaks as a function of the irradiation time. [26]

The beam energy and current density with the beam exposer time on mica surface are the important parameter to selectively remove or dissociation of mica layer with focus electron in AES system. The contamination present on the surface can also significantly affect the dissociation of mica with incident electron radiations. We have observed a small amount of carbon (or a carbon compound) was present on the mica sample when performing the exfoliated process in air. To remove the carbonaceous compound from the surface of mica, we performed heating treatment in an ultra-high (10^{-8} torr) vacuum condition. It was found that, the carbon contamination on mica can be removed by heating the sample for approximately 2 hours in 10^{-8} torr vacuum conditions at 500 to 550°C. **Fig. 5.9** clearly illustrates the carbon AES peak before and after heating treatment, indicating that after performing the heating treatment the carbon AES peak is completely gone. It was also observed that extended period of heating at more than 600 °C can make the depletion of K elements from the mica surface. During the high heating process K element from the mica surface simply evaporated. In our experiment, we have used high grade of artificially synthesized mica, and assuming that the source of the contaminant carbon arises from the carbonaceous atmospheric gas component during air

exposing of the sample after completing the exfoliations process. To perform the exfoliations process we have used poly-urethane hand roller, which is free from any contaminations (finding is explained in details in chapter 3).

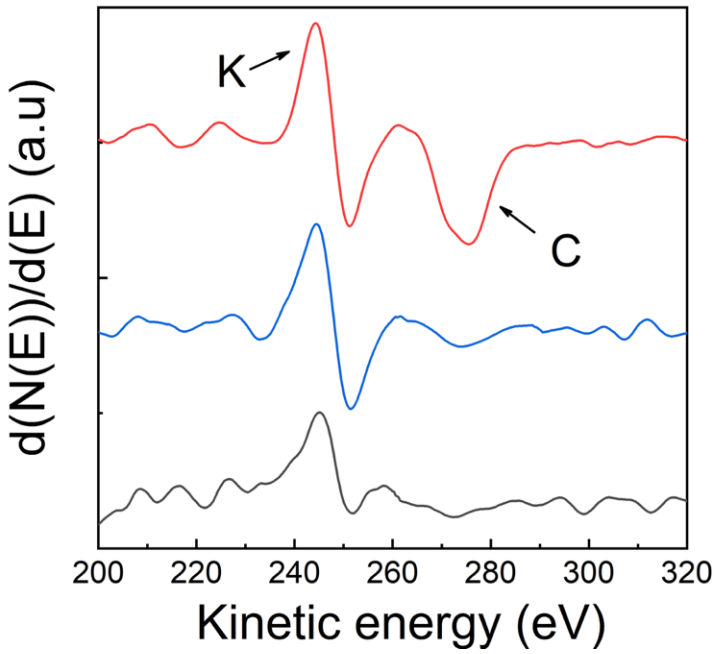

Figure 5.9: Heat treatment of C-contaminated mica surface in UHV, blue line before heating and red line after heating the mica nanosheets at 500 °C for 2 hours. Black line is heating the sample at 650 °C for 4 hours and its showing that the amount of K element is depleting from the sample.

Some experimental observations of mica etching process by AES technique can be qualitatively explain by **Fig. 5.10**, but it is important to remember that the etching process prospectively involves a complex interaction of several factors such as electron-stimulated desorption (ESD), electron-beam heating, beam current, beam energy, scan time and vacuum conditions. The electron-stimulated desorption has been extensively studied by many authors as a fundamental mechanism in the AES techniques involving electron bombardment to the etching phenomenon [37,38]. There are many and diverse explanations of the physical mechanism leading to the electron-induced dissociation. One probable mechanism related to mica dissociations by electron bombardment is, the high-energy electrons traverse a thickness equivalent to their range and come to rest, producing a net negative

charge in the sample. This net electric charge sets up an electric field in the mica layers. Under the influence of this electric field, the positive elements (such as K^+, Mg^{2+} and Al^{3+}) presents in the mica systems are diffused away from the surface into the vacuum. This mechanism is related for the release of oxygen from soda glass bombarded by high-energy (10–27 keV) electrons was postulated by Lineweaver [39]. The above mechanism may not be responsible for the dissociation of mica instead the mechanism responsible for mica dissociation are more complicated than the Lineweaver mechanism. Another likely mechanism proposed by Redhead [40] and by Menzel and Gomer [41] for the neutral and ionic desorption in ESD from a substrate-adsorbate system and based on the Franck-Condon principle[42], may be applicable to the case of desorption of elemental components from the mica surface. According to this theory, in a metal-adsorbate system (M + A), the bombardment by electrons causes transitions from the ground state to an ionic state of the type ($M + A^+ + e^-$) with the final states distributed over the Franck-Condon region. The A^+ ions formed on the repulsive part of the potential energy curve corresponding to the ionic state may be desorbed as ions or more likely as neutrals following Auger neutralization or deexcitation. We may extend this explanation to the case of mica dissociations as well, where the tetrahedron and octahedron bond is broken by the excitation to the ionic state of the molecules and followed by the desorption from the surface as of free elements. Because of the interaction of electron bombardment and dissociations of mica nanosheets in the AES etching process are more complicated therefore substantial additional work will be required to fully validate a model to explain the process.

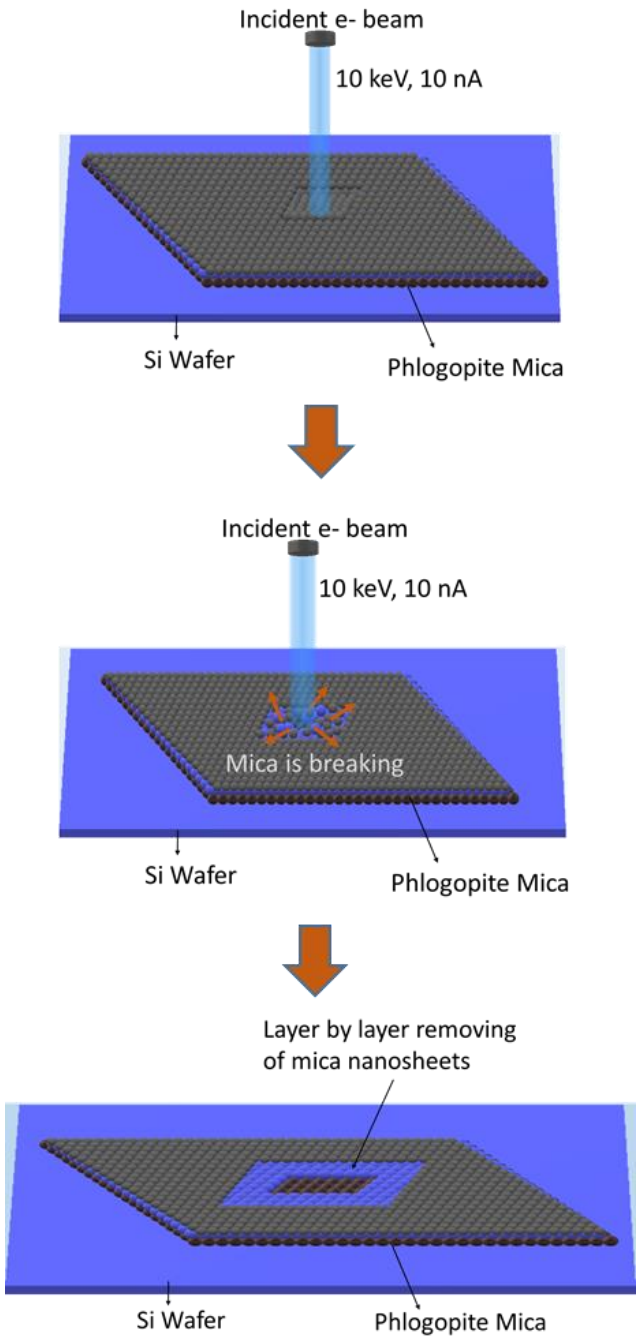

Figure 5. 10: Illustration depicting the AES etch process in which mica layers is removed by electron bombardment. The mica compound break into elemental component during radiations and spontaneously desorbed from the surface and making selective patters on mica nanosheets by removing layers.

5.4 Conclusion

We have demonstrated selective removal of mica layers by electron beam irradiation to form high-resolution patterning. We found that several factors influencing electron beam etching of mica nanosheets. It was determined from the experimental results that the etching depth decreases with increasing beam energy, increases with decreasing beam current, and increasing with etching durations. The electron beam bombarding on mica surface has a spontaneous dissociations of mica composition. With extended irradiation, $Si(-O-)_4$ tetrahedron broke up into elemental Si and remove from the mica surface and dissociation take place. Carbon contamination of mica substrates can be eliminated by long time heating at temperatures of 500 °C in vacuum. The dissociations process is primarily involved electric field creations or ionization of deep levels of the adsorbate in Auger excitations in terms of electron-stimulated desorption process. While this work provides practical and fundamental insight into the AES etching of mica layers, there is still a need for considerable study of this and other material systems. To fully realize the potential of AES etching, it is essential to gain a stronger understanding of the fundamental physical processes involved. Our results will advance the understanding of mica chemical stability and accelerate its use in practical optoelectronic and photonic devices.

References

1. Bitla, Yugandhar, and Ying-Hao Chu. "MICAtronics: A new platform for flexible X-tronics." FlatChem 3 (2017): 26-42.
2. Rudenko, A. N., et al. "Graphene adhesion on mica: Role of surface morphology." Physical Review B 83.4 (2011): 045409-045415.
3. Low, Chong Guan, and Qing Zhang. "Ultra-thin and Flat Mica as Gate Dielectric Layers." Small 8.14 (2012): 2178-2183.
4. Maslova, M. V., L. G. Gerasimova, and Willis Forsling. "Surface properties of cleaved mica." Colloid Journal 66.3 (2004): 322-328.
5. Castellanos-Gomez, Andres, et al. "Atomically thin mica flakes and their application as ultrathin insulating substrates for graphene." Small 7.17 (2011): 2491-2497.
6. Low, Chong Guan, et al. "Graphene field effect transistors with mica as gate dielectric layers." Small 10.20 (2014): 4213-4218.
7. Xu, Hai-Qun, et al. "Visible-light photoreduction of CO_2 in a metal–organic framework: boosting electron–hole separation via electron trap states." Journal of the American Chemical Society 137.42 (2015): 13440-13443.
8. Sharma, Subash, et al. "Opening of triangular hole in triangular-shaped chemical vapor deposited hexagonal boron nitride crystal." Scientific reports 5 (2015): 10426-10432.
9. Liao, Yunlong, et al. "Oxidative etching of hexagonal boron nitride toward nanosheets with defined edges and holes." Scientific reports 5 (2015): 14510-14518.
10. Liu, Zheng, et al. "In-plane heterostructures of graphene and hexagonal boron nitride with controlled domain sizes." Nature nanotechnology 8.2 (2013): 119-125.
11. J. I. Goldstein, D. E. Newbury, P. Echlin, D. C. Joy, A. D. Romig, C. E. Lyman, C. Fiori, and E. Lifshin, Scanning Electron Microscopy and X-Ray Microanalysis, 2nd ed., New York (1992).

12. Sanchez, Erik J., J. T. Krug, and X. S. Xie. "Ion and electron beam assisted growth of nanometric Si m O n structures for near-field microscopy." Review of scientific instruments 73.11 (2002): 3901-3907.
13. Randolph, S. J., J. D. Fowlkes, and P. D. Rack. "Effects of heat generation during electron-beam-induced deposition of nanostructures." Journal of applied physics 97.12 (2005): 124312-124318.
14. Choi, Young R., et al. "Effect of Electron Beam-Induced Deposition and Etching Under Bias." Scanning: The Journal of Scanning Microscopies 29.4 (2007): 171-176.
15. Gopal, Vidyut, et al. "Rapid prototyping of site-specific nanocontacts by electron and ion beam assisted direct-write nanolithography." Nano Letters 4.11 (2004): 2059-2063.
16. Matsui, Shinji, and Katsumi Mori. "Direct writing onto Si by electron beam stimulated etching." Applied physics letters 51.19 (1987): 1498-1499.
17. Taneya, M., et al. "Electron-beam-induced pattern etching of AlGaAs using an ultrathin GaAs oxide as a resist." Journal of applied physics 68.7 (1990): 3630-3634.
18. Chang, Chuan C. "Analytical Auger electron spectroscopy." Characterization of Solid Surfaces. Springer, Boston, MA, 1974. 509-575.
19. Chang, Chuan C. "Auger electron spectroscopy." Surface Science 25.1 (1971): 53-79.
20. Shimizu, Ryuichi. "Quantitative analysis by Auger electron spectroscopy." Japanese journal of applied physics 22.11R (1983): 1631-1637.
21. Seah, M. P. "Quantitative Auger electron spectroscopy and electron ranges." Surface Science 32.3 (1972): 703-728.
22. Holloway, P. H. "Thickness determination of ultrathin films by Auger electron spectroscopy." Journal of Vacuum Science and Technology 12.6 (1975): 1418-1422.
23. Xu, Mingsheng, et al. "Auger electron spectroscopy: a rational method for determining thickness of graphene films." ACS Nano 4.5 (2010): 2937-2945.

24. Sutter, P., and E. Sutter. "Thickness determination of few-layer hexagonal boron nitride films by scanning electron microscopy and Auger electron spectroscopy." APL Materials 2.9 (2014): 092502-092507.
25. Mathieu, H. J., M. Datta, and D. Landolt. "Thickness of natural oxide films determined by AES and XPS with/without sputtering." Journal of Vacuum Science & Technology A: Vacuum, Surfaces, and Films 3.2 (1985): 331-335.
26. Islam, Mohammad Razzakul, and Masahiko Tomitori. "Layer-etching of mica nanosheets using focused electron beam." Applied Physics Express 13 (2020): 106502-106506.
27. Madey, Theodore E., and John T. Yates Jr. "Electron-stimulated desorption as a tool for studies of chemisorption: A Review." Journal of Vacuum Science and Technology 8.4 (1971): 525-555.
28. Joseph Goldstein et al. Scanning electron microscopy and X-ray microanalysis: a text for biologists, materials scientists, and geologists. Springer Science & Business Media (2012).
29. Randolph, S. J., J. D. Fowlkes, and P. D. Rack. "Focused electron-beam-induced etching of silicon dioxide." Journal of applied physics 98.3 (2005): 034902-034911.
30. ToanáTran, Trong, and Lu HuaáLi. "Electron beam directed etching of hexagonal boron nitride." Nanoscale 8.36 (2016): 16182-16186.
31. Dai, S., et al. "Tunable phonon polaritons in atomically thin van der Waals crystals of boron nitride." Science 343.6175 (2014): 1125-1129.
32. Taylor, Norman J. "Thin reaction layers and the surface structure of silicon (111)." Surface Science 15 (1969): 169-174.
33. Coad, J. P., H. E. Bishop, and J. C. Riviere. "Electron-beam assisted adsorption on the Si (111) surface." Surface Science 21.2 (1970): 253-264.
34. Grant, J. T., and T. W. Haas. "Auger electron spectroscopy of Si." Surface Science 23.2 (1970): 347-362.
35. Maguire, H. G., and P. D. Augustus. "The influence of the band structure on the Auger electron spectrum of silicon." Journal of Physics C: Solid State Physics 4.9 (1971): L174.

36. Maki, Kunisuke, and Yukichi Shigeta. "Surfaces of vacuum-deposited silicon oxide films studied by auger electron spectroscopy." Japanese Journal of Applied Physics 20.6 (1981): 1047-1052.
37. Madey, Theodore E., and John T. Yates Jr. "Electron-stimulated desorption as a tool for studies of chemisorption: A Review." Journal of Vacuum Science and Technology 8.4 (1971): 525-555.
38. Poppa, Helmut, and A. Grant Elliot. "The surface composition of mica substrates." Surface Science 24.1 (1971): 149-163.
39. Lineweaver, Jack L. "Oxygen outgassing caused by electron bombardment of glass." Journal of Applied Physics 34.6 (1963): 1786-1791.
40. Redhead, P. A. "Interaction of slow electrons with chemisorbed oxygen." Canadian Journal of Physics 42.5 (1964): 886-905.
41. Menzel, Dietrich, and Robert Gomer. "Desorption from metal surfaces by low-energy electrons." The Journal of Chemical Physics 41.11 (1964): 3311-3328.
42. Lax, Melvin. "The Franck-Condon principle and its application to crystals." The Journal of Chemical Physics 20.11 (1952): 1752-1760.

Chapter 6

6.1 Conclusions

We have successfully fabricated atomically thin down to single and few layer mica nanosheets on SiO_2/Si and, Au and Ir-coated Si substrates using the procedure based on mechanical exfoliation with the polyurethane hand roller. We found that our fabrication method yielded single and few-layer wider mica nanosheets, which were evaluated by AFM and SAM. In comparison with other conventional exfoliations process, our modified method of using poly-urethane hand roller provide much larger and high quality mica nanosheets.

We determined the quantitative thickness of the few-layer mica nanosheets by using AES in regard to the change of peak-to-peak intensities of AES spectra. The Auger spectra showed distinct characteristic shapes and intensities according to the change of the number of layers of mica nanosheets. It has been shown that AES analysis can be used as a standard to determine their thickness in the range of 1 to 6 layers of mica film thickness, which has well coincided with the thickness measured by AFM. We also derived the inelastic mean free path (IMPF) values for mica nanosheets as a function of Auger electron energy which showed good agreement with the universal curve of IMPF, based on plasmon energy loss in solids, for energy dependent electron escape depth. We successfully investigated the SEM image of several layer mica nanosheets with SAM observations and found that the SEM image contrast changes with increasing number of mica layer. This study demonstrates that the elemental and structural analysis of even insulating thin two-dimensional layered materials can be plainly conducted by the SAM, the information of which is fundamental and critical to realize nanoscale electronic devices, composed of conducting and insulating 2D layered materials.

The current-voltage characterization of few-layers mica nanosheets with the metal-insulator-metal structure highlight the electron tunneling probability through mica nanosheets. We found that the barrier height of mica nanosheets continually increased with the increasing thickness.

As we characterized mica nanosheet with electron beam in the AES observations, the effect of beam irradiations on the sample surface were investigated and found that long time electron beam incident on mica surface make permanent damage on it. We observed that with the Focused electron-beam induced etching process, mica layer can selectively be removed. It was determined that etching rate increases with decreasing incident beam energy, increasing beam current and by increasing incident durations.

In regard to the fabrication and characterization of mica nanosheets as a 2D nanomaterial presented here, we believe that our findings and proposed methods will expanding the scope of materials selections for nanofabrication of 2D materials.

6.2 Future Work

Semiconductor technologies have evolved with development of integrated circuits that demanded the high-performance and miniaturization of individual transistors of the electronic devices. Among a diversity of the improvement of transistors, the role of the gate dielectric materials is remarkably important to the proper functioning of field effect transistors (FETs). The gate dielectric materials must have high resistivity to prevent the leakage current, as well as high dielectric constant and ultra-flat surface, and free from surface charge traps and defects to have enough capacitance for channel current flow. To date, lots of high-*k* materials such as hafnium oxide, zirconium oxide, aluminum oxide, and silicon nitride have been widely employed as a gate insulator. However, there are many difficulties with high-*k* gate dielectric such as crystallization upon heating, dopant penetration and fixed charge, low channel mobility and uncontrolled oxide formation at the Si/high-*k* interface. Hence,

single crystalline materials such as ‘artificially synthesized mica’ is an excellent choice for the gate dielectric material because of its uniform high dielectric constant, high dielectric strength, low power loss and atomically flat surface free from surface charge traps and surface defects. Thus, one of the most challenging and attractive targets using mica is for a dielectric gate layer of FETs through the processes to handle the mica as a thin layered crystal.

To use mica as gate dielectric, the following researches will be realized:

1. Mica has excellent properties so that mica could be a good dielectric material in addition to h-BN, especially when it is down to a few atomic layers thick. First of all, mica has ultra-flat surface free from surface charge traps and surface defects, those will enhance the carrier mobility of the channel. In addition, mica has uniform high dielectric constant twice that of silicon oxide and BN are more advantageous to enable highly effective gate control over the channel potential of graphene FET.
2. As we can prepare highly clean thin mica sheets, it is expected that the cleanness of mica greatly influences the transport property of the graphene affix on it.
3. Interface plays a crucial role in transistor performances, therefore a proper interface will be formed during the device fabrication and experimental studies on interfaces will be carried out.

List of publications

1. **Razzakul, Islam Mohammad**, and Masahiko Tomitori. "Evaluation of the discrete thickness of exfoliated artificially synthesized mica nanosheets on silicon substrates: Toward characterization of the tunneling current through the nanosheets." Applied Surface Science 532 (2020): 147388-147401.
2. **Islam, Mohammad Razzakul**, and Masahiko Tomitori. "Layer-etching of mica nanosheets using focused electron beam." Applied Physics Express 13 (2020): 106502-106506.